ISSN 2587-1366

TUJE

TURKISH JOURNAL OF ENGINEERING

VOLUME 6 ISSUE 3 JULY 2022

JOURNAL SECRETARY

TURKISH JOURNAL OF ENGINEERING (TUJE)

Turkish Journal of Engineering (TUJE) is a multi-disciplinary journal. The Turkish Journal of Engineering (TUJE) publishes the articles in English and is being published 4 times (January, April, July and October) a year. The Journal is a multidisciplinary journal and covers all fields of basic science and engineering. It is the main purpose of the Journal that to convey the latest development on the science and technology towards the related scientists and to the readers. The Journal is also involved in both experimental and theoretical studies on the subject area of basic science and engineering. Submission of an article implies that the work described has not been published previously and it is not under consideration for publication elsewhere. The copyright release form must be signed by the corresponding author on behalf of all authors. All the responsibilities for the article belongs to the authors. The publications of papers are selected through double peer reviewed to ensure originality, relevance and readability.

AIM AND SCOPE

The Journal publishes both experimental and theoretical studies which are reviewed by at least two scientists and researchers for the subject area of basic science and engineering in the fields listed below:

Aerospace Engineering
Environmental Engineering
Civil Engineering
Geomatic Engineering
Mechanical Engineering
Geology Science and Engineering
Mining Engineering
Chemical Engineering
Metallurgical and Materials Engineering
Electrical and Electronics Engineering
Mathematical Applications in Engineering
Computer Engineering
Food Engineering

PEER REVIEW PROCESS

All submissions will be scanned by iThenticate® to prevent plagiarism. Author(s) of the present study and the article about the ethical responsibilities that fit PUBLICATION ETHICS agree. Each author is responsible for the content of the article. Articles submitted for publication are priorly controlled via iThenticate ® (Professional Plagiarism Prevention) program. If articles that are controlled by iThenticate® program identified as plagiarism or self-plagiarism with more than 25% manuscript will return to the author for appropriate citation and correction. All submitted manuscripts are read by the editorial staff. To save time for authors and peer-reviewers, only those papers that seem most likely to meet our editorial criteria are sent for formal review. Reviewer selection is critical to the publication process, and we base our choice on many factors, including expertise, reputation, specific recommendations and our own previous experience of a reviewer's characteristics. For instance, we avoid using people who are slow, careless or do not provide reasoning for their views, whether harsh or lenient. All submissions will be double blind peer reviewed. All papers are expected to have original content. They should not have been previously published and it should not be under review. Prior to the sending out to referees, editors check that the paper aim and scope of the journal. The journal seeks minimum three independent referees. All submissions are subject to a double blind peer review; if two of referees gives a negative feedback on a paper, the paper is being rejected. If two of referees gives a positive feedback on a paper and one referee negative, the editor can decide whether accept or reject. All submitted papers and referee reports are archived by journal Submissions whether they are published or not are not returned. Authors who want to give up publishing their paper in TUJE after the submission have to apply to the editorial board in written. Authors are responsible from the writing quality of their papers. TUJE journal will not pay any copyright fee to authors. A signed Copyright Assignment Form has to be submitted together with the paper.

PUBLICATION ETHICS

Our publication ethics and publication malpractice statement is mainly based on the Code of Conduct and Best-Practice Guidelines for Journal Editors. Committee on Publication Ethics (COPE). (2011, March 7). Code of Conduct and Best-Practice Guidelines for Journal Editors. Retrieved from http://publicationethics.org/files/Code%20of%20Conduct_2.pdf

PUBLICATION FREQUENCY

The TUJE accepts the articles in English and is being published 4 times (January, April, July and October) a year.

CORRESPONDENCE ADDRESS

Journal Contact: tuje@mersin.edu.tr

CONTENTS

Volume 6 – Issue 3

ARTICLES

Turkish Journal of Engineering

https://dergipark.org.tr/en/pub/tuje

e-ISSN 2587-1366

Molecular dynamic simulation of uniaxial tension deformation applied to α-Fe nanowire

Sefa Kazanç [1], Canan Aksu Canbay*[2]

[1] *Fırat University, Faculty of Education, Mathematics and Science Education, Elazığ, Turkey*
[2] *Fırat University, Faculty of Science, Department of Physics, Elazığ, Turkey*

Keywords
Nano wire
Mechanical properties
Molecular dynamics
Strain rate

ABSTRACT

In this study, using the Molecular Dynamics (MD) simulation method, the effects of the tensie stress applied to the Fe nano wire along the direction of [100] for different temperatures and strain rates were tried to be determined. The stress-strain curve, Young' s modulus, yield stress and plastic deformation of the model system under tensile stress were investigated. The Embedded Atom Method (EAM), which includes many body interactions, was used to determine the interactions between atoms. It was determined that temperature and strain rate had an effect on the mechanical behaviour of α-Fe nanowire. It was found that the Young' s modulus is independent of the strain rate at low temperatures, but decreases with increasing temperature. It was also determined that the flow strain decreased with increasing temperature and decreasing strain rate. The motion of dislocations and twinning corresponding to plastic deformation and the resulting reorientation of regional crystal structures were attempted to be determined by the method of Common Neighbour Analysis (CNA).

1. INTRODUCTION

Both metallic and semiconductor nano wires are among the remarkable materials recently due to their superior mechanical, electrical, thermal, magnetic and optical properties due to their nanoscale dimensions (Suresh and Li 2008; Gao et al. 2016; Da Silva et al. 2001; Park and Zimmerman 2005; Diao et al.2004). These unusual characteristics have increased the interest in nanowires and offered the opportunity to be used in many different research and application areas. Nano wires, one of the important one-dimensional nano structures, will play an important role in the design and production of electronic, optical and nano-electromechanical devices in the future (Wu 2006; Jing et al. 2009; Wen et al. 2008; Gan and Chen 2009). In recent years, various nano devices such as nano laser (Huang and Mao 2001; Duan and Huang 2003), field effect transistor (Arnold et al. 2003; Wu et al. 2004), light emitting diode (Kim et al. 2008) have been developed from nano wires. Many studies have been conducted on the nanoscale mechanical behaviors to increase the technological applications of nanowires (Diao et al. 2006; Alavi et al. 2010; Zhu and Shi 2011; Wang et al. 2011; Sainath and Choudhary 2016; Wang et al. 2011; Godet et al. 2019). Although many studies have been conducted for metallic materials in volumetric structure to determine these behaviors, studies for nanoscale materials are inadequate. Many studies have been conducted to experimentally determine the thermal, mechanical and electrical properties of different metallic nanowires (Pasquier et al. 2005; Lee et al. 2004; Li et al. 2006). Dynamic high-resolution transmission electron microscopy (Legoas et al.2002; Rodrigues et al. 2000), atomic force microscopy is used (Agrait et al. 1995; Marszalek et al. 2000) and transmission electron microscopy to experimentally examine nano-scale metallic materials at atomic scale. (Agrait et al. 1993; Landman et al. 1996). Deformation and breakage of nanowires can be easily affected by many factors such as temperature, orientation, load application rate, surface and boundary conditions. Therefore, metallic nanowires always behave particularly and unpredictably under experimental conditions.

Computer simulations play an important role in understanding the structural and thermodynamic properties of substances at the atomic level. MD simulation, one of the atomic simulation techniques, is

---

* **Corresponding Author**

(skazanc@firat.edu.tr) ORCID ID 0000-0002-8896-8571
*(caksu@firat.edu.tr) ORCID ID 0000-0002-5151-4576

Cite this article

Kazanc S & Canbay C A (2022). Molecular dynamic simulation of uniaxial tension deformation applied to α-Fe nanowire. Turkish Journal of Engineering, 6(3), 190-198

Research Article / DOI: 10.31127/tuje.888891

Received: 01/03/2021; Accepted: 07/05/2021

one of the effective methods to evaluate the deformation and fracture characteristics of nanowires subjected to stress. Especially in recent years, there are many theoretical studies in the literature to determine the mechanical behaviors and deformation mechanisms of volumetric and nano structures using the classical MD simulation method (Tschoppa and McDowella 2008; Salehinia and Bahr 2014; Zhanga et al. 2017; Rawat and Mitra 2020) and there are also first principal methods based on density function theory (Da Silva et al. 2004; Krüger et al. 2002). However, in studies to be carried out with this method, computers with a low particle count and a large number of processors are needed to model atomic systems. With the MD simulation method, the orbits of atoms are produced over a finite time in phase space, and the desired physical and thermodynamic properties of the system can be determined by using these orbits (Davoodi and Ahmadi 2012). The determination of the potential energy function, which expresses the interactions between atoms mathematically, is extremely important in terms of the compatibility of the results obtained for the system to be modeled with the experimental values (Kazanc et al. 2003; Voter and Chen 1987). There are many potential functions developed by different researchers for different element and alloy systems (Cai and Ye 1996; Kazanc and Ozgen 2004; Wadley et al. 2001; Malins et al. 2013). EAM, which is based on multi-body interactions, is one of the most used potential functions in studies conducted with MD simulation method. Horstemeyer et al. (2001) studied the effect of length and time on plastic flows of fcc metals under simple shear, and Liang and Zhou (Liang and Zhou 2003) studied the effect of size and strain rate on the stress behavior of Cu nanowires. However, recently the shape recall effect and artificial elasticity behavior in Cu and Ag nanowires have also been investigated by MD simulation method (Liang et al. 2005; Park and Zimmerman 2005; Park and Ji 2006).

In this study, the mechanical behavior of the Fe nano wire system was tried to be investigated by MD simulation by applying a tensile stress under different temperatures and strain rates along the direction of [100]. LAMMPS open-source MD simulation program was used in the study (LAMMPS 2021). Force interactions between the EAM potential function and Fe atoms were determined. In the results obtained, it was determined that the temperature and strain rates had an effect on the mechanical properties of the nanowire. The CNA method was used to determine the atomic structure changes caused by the applied stress.

2. METHOD

Classical MD method aims to calculate the trajectories of atoms in phase space by numerical integration of equations of motion obtained from Lagrange function of a system with N atoms. Details of the MD simulation method can be found in the literature (Parrinello and Rahman 1980; Parrinello and Rahman 1981).

The axial stress applied to the computing cell is determined by the volume average of the kinetic and potential energies of all the atoms in the system. The sttress tensor can be calculated using the virial theorem as given below.

$$\mathbf{\Pi} = V^{-1}\left[\sum_{i=1}^{N} m_i v_i \cdot v_i - \sum_{i=1}^{N}\sum_{j>i}^{N} \frac{F_{ij}}{r_{ij}} \mathbf{r}_i \cdot \mathbf{r}_i\right] \qquad (1)$$

In this expression, V and N indicate the volume and total number of atoms of the system, m_i and ϑ_i indicate the mass and velocity of the ith atom, and F_{ij} and r_{ij}, respectively, the force and distance between i and j atoms. In Equation (1), the first sum term is due to the thermal vibration of the system, and the second sum term is due to the inter-atomic force (Wen et al. 2010).

It is said that an object under the influence of external forces is in a stressed state. The state of stress at any point in matter is determined by the nine-component stress tensor.

$$\sigma_{ij} = \begin{pmatrix} \sigma_{11} & \sigma_{12} & \sigma_{13} \\ \sigma_{21} & \sigma_{22} & \sigma_{23} \\ \sigma_{31} & \sigma_{32} & \sigma_{33} \end{pmatrix} \qquad (2)$$

The components of the hard tensor σ_{11}, σ_{22}, σ_{33} (which can also be expressed as σ_x, σ_y, σ_z respectively) are known as the normal components of the hard, while the other components are known as the stress shear components. Positive values of normal components correspond to tensile stress, negative values correspond to compressive stress. In uniaxial loading applied to the system along the x-axis, only the σ_x component changes. On the other hand, other components are zero (Saitoh and Liu 2009; Jacobus et al. 1996).

The strain along the x-axis is defined as $\varepsilon_x = (l_x - l_{x0}) / l_{x0}$. This expression is the length of the l_{x0} wire before the loading is applied in the x direction and the length under the load l_x (Saitoh and Liu 2009).

In this study, atoms were placed at fcc lattice points for the Fe nano wire system as the initial structure. Periodic boundary conditions were applied along the direction of [100] where stress would be applied as atoms were released along the directions [010] and [001] of the nanowire. The initial velocities of the atoms in the model system were determined randomly in accordance with the Maxwell-Boltzman velocity distribution. Numerical integration of the equations of motion of the system in 1 fs time steps was performed using the velocity form of the Verlet algorithm. Uniaxial tensile tests were applied to the NVT statistical community where the number of particles, volume and temperature were kept constant at certain values. Before the stress loading was applied, $5\text{x}10^4$ MD steps in all studies were provided to stabilize the system in a stable structure. The cut-off distance of the potential function used was determined as $r_c = 2a_{Fe}$.

2.1. Potential Energy Function

The EAM function, which includes the multi-body interaction terms for modeling monatomic and alloy systems, is one of the most used functions. Total energy expression of the system in a computing cell composed of

N atoms in EAM (Finnis and Sinclair 1984; Sutton and Chen 1990);

$$E_T = \frac{1}{2}\sum_{\substack{i,j \\ (i\neq j)}}^{N} \emptyset(r_{ij}) + \sum_{i}^{N} F(\overline{\rho_i}) \tag{3}$$

is given in the above form. The first term refers to the double interactions between atoms. The second term describes attractive interactions that involve many body interactions and known as embedding functions. Binary interaction potential and embedding function can be defined differently for different systems. Hence there are different types of EAM potential functions (Finnis and Sinclair 1984; Sutton and Chen 1990). Details of the EAM potential function used in this study and the values of the parameters for the element Fe can be found in the literature (Wadley et al. 2001).

In MD simulation studies, determining the tight package structures such as fcc, hcp, bcc in the model system is one of the important problems. Many methods have been developed for the analysis of these solid phase structures. The general purpose of these methods is to assign a structural type to each particle in the system. However, these methods try to determine how close they are by matching a local structure with an idealized structure. For the characterization of the structures existing in the MD cell, in simulation studies, centrosymmetry parameter analysis (CSP), common neighbohr analysis, bond-order analysis, bond-angle analysis), Honeycutt-Andersen, and Voronoi analysis are widely used (Stukowski 2012).

3. RESULTS

In this study, the effect of the uniaxial tensile stress applied along the direction of [100] on the tensile behaviour of the single crystal Fe nano wire model system, depending on different temperature and strain rates, was investigated using the MD method. The nanowire structure was formed by placing Fe atoms along the crystallographic directions [100], [010] and [001] in the x, y, and z directions as shown in Figure 1.

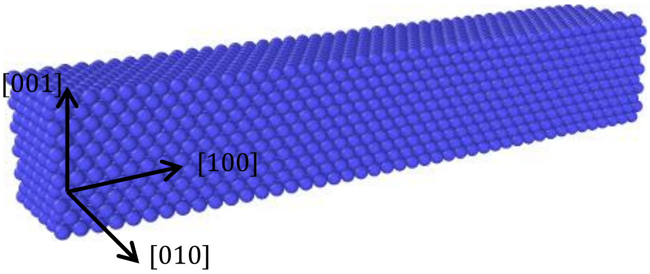

Figure 1. Initial structure of a single crystal α Fe nanowire before stress is applied.

At the beginning of the simulation study, the nanowire has a length of 12.8 nm (45 bcc unit cell) in the x direction and 1.43 nm (5 bcc unit cell) in the y and z direction. Periodic boundary conditions are applied along the x-axis, surfaces in other directions are released. Stretching processes were applied along the x direction throughout the entire study. The system is balanced with 5x10^4 MD steps before loading on the nano wire. Fe is one of the polyformic (multi-shaped) elements with different crystal structures at different temperatures. It has Fe bcc structure up to 911°C at zero pressure value. Fe in this structure is known as α-Fe (Engin and Urbassek 2008). Fe atoms are placed at fcc lattice points in the initial structure of the MD cell.

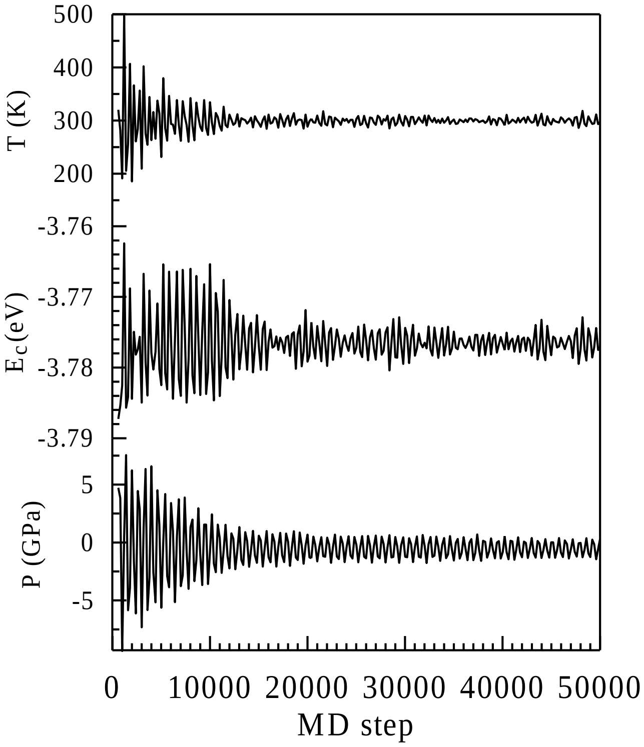

Figure 2. Change of temperature, Ec and pressure for the first 5x10^4 MD steps

Figure 2 shows the changes of temperature, bonding energy (E$_c$) per unit atom and pressure values obtained for the model system where 5x10^4 MD steps are brought into equilibrium at 300 K temperature value. The radial distribution functions obtained in different MD steps during this balancing process are given in Figure 3. It is clearly seen from Fig. 2, that the nano wire system where the atoms are placed on the fcc mesh points has an unstable structure until 18000. MD step, and after this step, it reaches a stable structure and reaches equilibrium state. This situation was also determined from the RDF curves given in Figure 3. In the RDF curves, it is clearly seen that the Fe nano wire has fcc structure at step 0, however, the instability of the structure at the 50. and 100. steps. From the RDF curves obtained at the steps of 350. and 500. MD, it was determined that the structure showed a transformation towards the stable bcc phase and the system reached equilibrium at the 25000. MD step and α-Fe structure with bcc unit cell was obtained. In this case, it can be said that a structural phase transformation has occurred in the MD cell from the high energy phase with fcc unit cell to the low energy phase with bcc unit cell. At the beginning of the simulation study, the transformation of the MD cell with fcc unit cell structure to bcc unit cell phase after a short time shows that the potential energy function used can realistically model the Fe system.

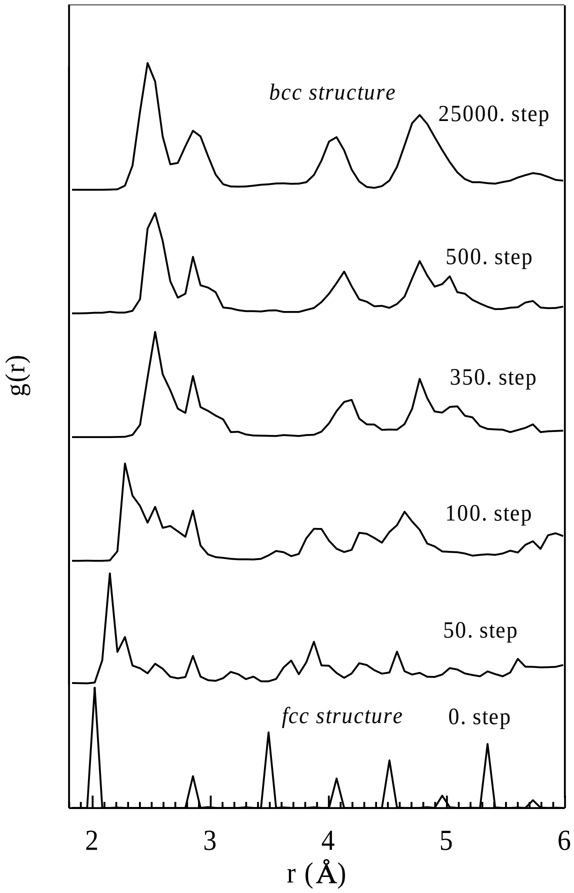

Figure 3. RDF curves obtained at different MD steps for the Fe nano wire model system.

In order to determine the melting temperature of the Fe nano wire, the temperature of the model system was increased from 300 K to 2100 K at intervals of 100 K. 5x10^4 MD steps were kept waiting for the system to reach equilibrium at every temperature value. In order to determine the melting temperature precisely, the temperature value was increased from 1400 K to 1900 K at 50 K intervals. At the end of the study, for each temperature value, E_c was averaged over the last 5000 MD steps. The results obtained are shown in Figure 4.

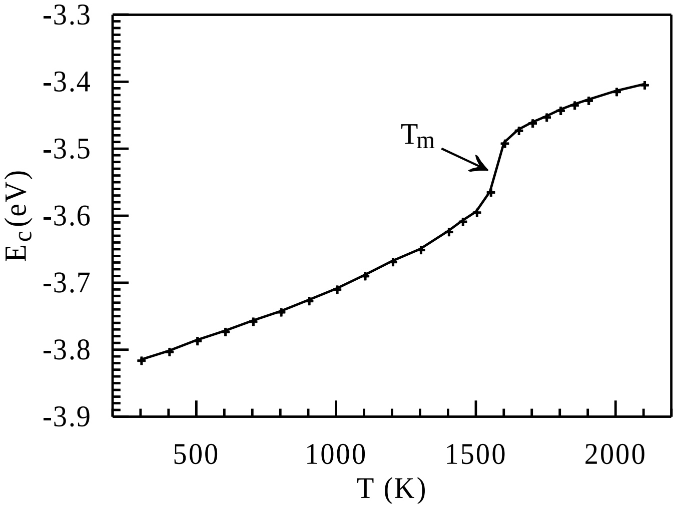

Figure 4. Variation of bonding energy (Ec) per unit atom with temperature

When the temperature reaches 1550 K, a discontinuity occurs in energy. This discontinuity in coherent energy is an indicator of the transition of the structure from solid phase to liquid phase (Karimi et al. 1997). The melting temperature for the Model Fe nano wire system was determined as 1575 ± 25 K.

In the uniaxial tensile studies, the tensile behaviour of the α-Fe nano wire at 300 K temperature was investigated until rupture. In Figure 5 (a-b), the stress-strain curve of the nano wire at 1x10^9 s^{-1} strain rate and the atomic positions obtained by CNA analysis from the OVITO program at different MD steps during the tensile process, respectively. The change in the form of two peaks and a flat region in the middle is clearly seen in the stress-strain curve given in Figure 5 (a). In the AB region, stress exhibits an almost linear change with the increase in strain. This is known as the elastic zone. The highest value (point B) of the sudden drop in stress before it begins is expressed as the flow stress. When a critical strain value is reached, it hardly shows a sudden drop (point C). This sudden decrease in the stress-strain graph is an indication of the onset of plastic deformation occurring in the model system. When a stress above the force corresponding to the yield stress value is applied to the material, the plastic deformation begins, and the sliding mechanism is activated. In other words, dislocations start to move, and plastic deformation occurs. This is a wide strain range from point C to point D and there is no significant change in strain. When it comes to point D, the stress-strain curve begins to show a change like at the beginning of the strain process (DE interval). As the strain continues, it suddenly drops to zero after a certain maximum value. This situation corresponds to the breaking of the nanowire. The deformation phases seen in the stress-strain graph were also observed in studies performed for other metallic nanowires (Zhu and Shi 2011; Wang et al. 2011; Li et al. 2010). In this study, CNA topological analysis method proposed by Honeycutt and Anderson was used to determine the percentage of regional structures such as fcc, hcp, bcc formed around the atoms in the model system during tensile process. CNA analysis is a useful characterization technique used to determine the structural development of crystal structures such as agglomeration defects, grain boundaries, deformation, and different phases (Bonny et al. 2013; Mishin et al. 2001). The CNA algorithm performs a geometric analysis of the closest neighbours around a reference atom. The minimum value between the first two peaks of the radial distribution function and the arrangement of the selected atoms within a certain distance are analyzed one by one (Bañuelos et al. 2016). In this analysis, each atom in the model system is classified according to regional crystal structures determined by the bonds between an atom and its closest neighbours. Therefore, the atoms here are divided into 4 classes as fcc, hcp, bcc and "other". Atoms in a regional fcc arrangement are considered fcc atoms. Atoms in a regional hcp arrangement are considered as hcp atoms seen as agglomeration defect structures formed in the fcc crystal. Atoms in all other local arrangements are called "other" atoms (Fanga et al. 2020). The CNA method was used to analyze microstructural developments during mechanical deformation. Figure 5 (b) shows the atomic images and CNA analysis of the Fe nano wire obtained from the OVITO program at different MD steps in order to contribute to the explanation of the stress-strain response expressed above.

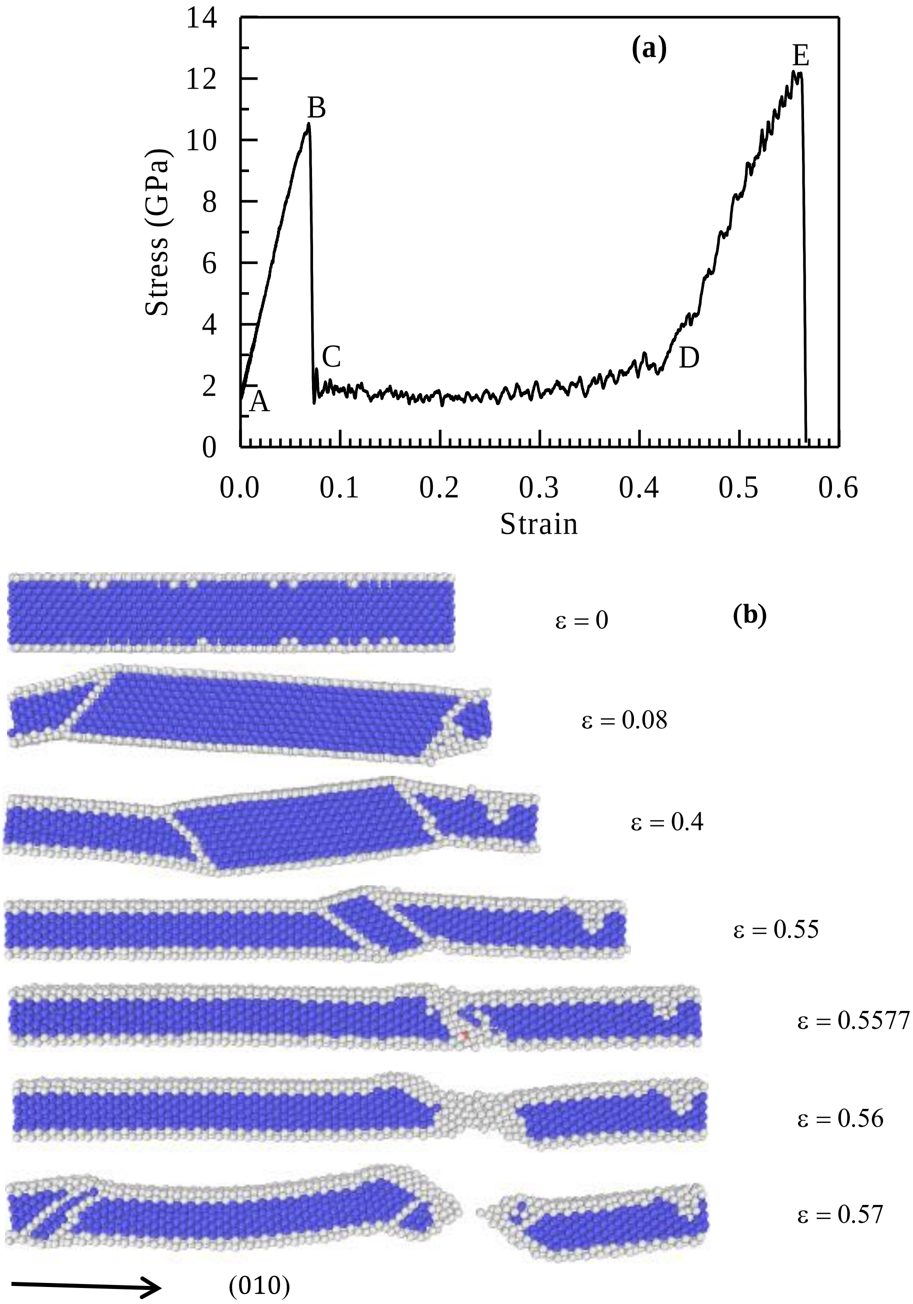

Figure 5. (a) Stress-strain curve for Fe nanowire at 300 K temperature for 1x10^9 s^{-1} strain rate, (b) atomic images obtained from CNA method at different strain values.

The blue bcc, the red hcp and the white colour represent the so-called "other" atoms that show regional localization outside of these structures. The atomic image of the nano wire (010) taken from the plane cross section belongs to point A in the stress-strain curve before the stress is applied for ε=0. The structure of bcc was determined as 64.1% and 35.9% as other structures. Since the periodic boundary conditions are not applied in the y and z directions of the nano wire, the atoms on the surface of the wire and close to the surface are not considered as bcc unit cell structure. When the critical strain value ε=0,08 (point B) is reached, it is seen that twin embryos are formed in the nanowire and this situation causes a sudden decrease in the stress value. It is observed that the twinning planes in the nanowire move and the nanowire reorients crystallographically at the stress values increasing from ε=0,08 to ε=0,4 (Ikeda et al. 1999). In this case, the nano wire is subject to plastic deformation. When it reaches the value of ε= 0,55, it is determined that the twinning planes disappear and the reorientation is complete. It is seen that when the tension continues to increase and the value of ε=0,557is reached, the nano wire gives neck and shrinkage occurs at ε=0,56. At ε=0,57 it is hard zero and rupture occurs. Nano wire was deformed mainly by the twinning mechanism with the applied tensile stress, and no shear behaviour was observed at this temperature.

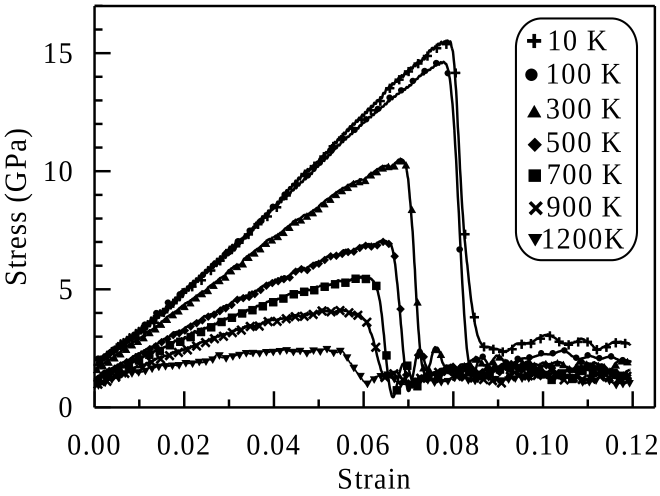

Figure 6. Stress-strain curve obtained at 5 different temperature values for 1x10^9 s^{-1} strain rate.

In Fig. 6, the obtained stress-strain curve as a result of the tensile stress applied to the single crystal Fe nano wire along the direction of [100] for 7 different temperature values is given and for each temperature the strain rate is taken as ε=1x10^9 s^{-1}. The region where the linear change occurs at low stresses (ε<0,05) for each temperature value is clearly seen from the graph. This zone is known as the elastic deformation zone. Stress also increases linearly with increasing of strain at low temperatures, while at high temperatures (> 500K) it exhibits a slightly non-linear behaviour before creep occurs. As it is known, thermally effective atomic vibrations dominate at high temperatures, and this causes Fe-Fe bonds to deform easily. This causes the stress response to strain during the stretching of the nanowire to exhibit a nonlinear behaviour. Such behaviour has also been observed in other metallic nanowires (Saha et al. 2017).

In Figure 6, Young's modulus is determined as a result of regression analysis of the linear region where elastic deformation occurs in the stress-strain graph. The change of Young' s modulus against temperature is given in Figure 7. Young's modulus decreases with increasing temperature (Wang et al. 2008). High values of the Young' s modulus, known as a measure of the elastic deformation under the force applied to the material, indicate that the elastic property of that material decreases. Generally, this decrease increases after half of the melting temperature value. Since there is no attraction force between atoms at the melting temperature, the Young' s modulus value approaches zero (Koh et al. 2005). The model system at the critical strain value where the stress decreases rapidly, undergoes plastic deformation. This maximum stress value at which dislocation nucleation begins to occur is known as the yield stress (Zhang et al. 2018). Yield stress, one of the important material properties, is a stress level associated with the onset of irreversible plastic deformation (Schiotz et al. 1998).

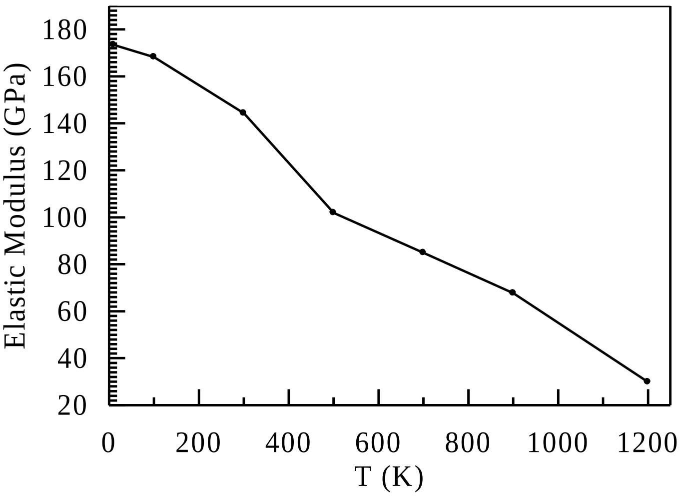

Figure 7. Modulus of elasticity with temperature for 1x10^9 s^{-1} strain rate.

For the Model Fe nano wire system, the variation of the yield stress with temperature is given in Figure 8.

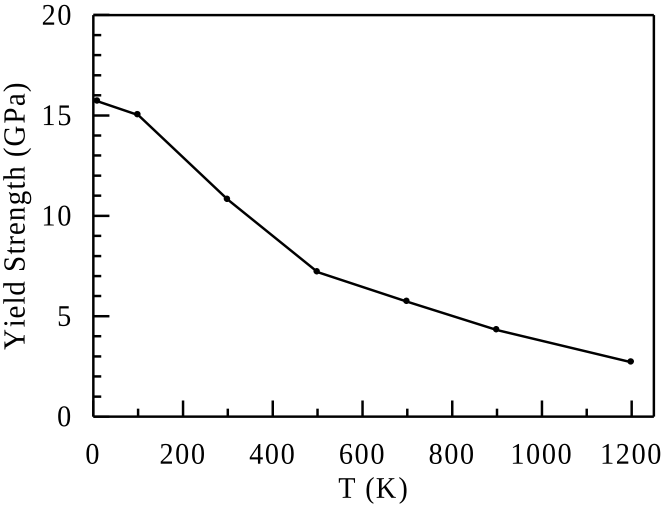

Figure 8. Change of yield stress with temperature for 1x109 s-1 strain rate.

It is clearly seen that the flow value decreases with the increase in temperature. At high temperature values, the atomic structure has high entropy. Atoms vibrate around their equilibrium positions at large amplitudes depending on temperature. Compared to low temperature values, many atoms gaining sufficient kinetic energy at high temperatures overcome the activation energy barrier and deformation occurs. This situation causes a decrease in the stress value as it causes twinning to spread and disappear. From the results obtained, it can be said that the thermal process plays an active role in the elongation of the Fe nano wire (Jing et al. 2009; Wen et al. 2008). In this study, the yield stress was determined as 10.79 GPa. Fe nano wire has a flow rate of 300 K, 11.1 GPa using two band EAM potential by Olsson et al. (2005) GPa has been found.

Figure 9 shows the stress-strain curves obtained for the Fe nano wire model system at 300 K temperature, for 1x10^8 s^{-1}, 1x10^9 s^{-1}, 1x10^{10} s^{-1}, 2x10^{10} s^{-1} and 5x10^{10} s^{-1}strain values. The strain values used in this study are quite high when compared to experimental values.

Because the time scale of the MD is determined by atomic mobility, the simulation can be made for a very short time. As a result of the short time scale, a high strain rate is required for proper deformation at the present time (Wen et al. 2008). It is clearly seen that the stress value for all strain rates increases linearly up to the strain value of 0.05. Below this value the stress-strain curve is completely overlapped for all applied strain rates. For the elastic zone where this plastic deformation does not occur, the model shows that the elastic properties of the system do not depend on the strain rate. In addition, the fact that the Young' s modulus is not dependent on the strain rate indicates that during the elastic deformation occurring in the same crystallographic directions in single crystals, the bonds require the same inter-atomic force for the same stress values.

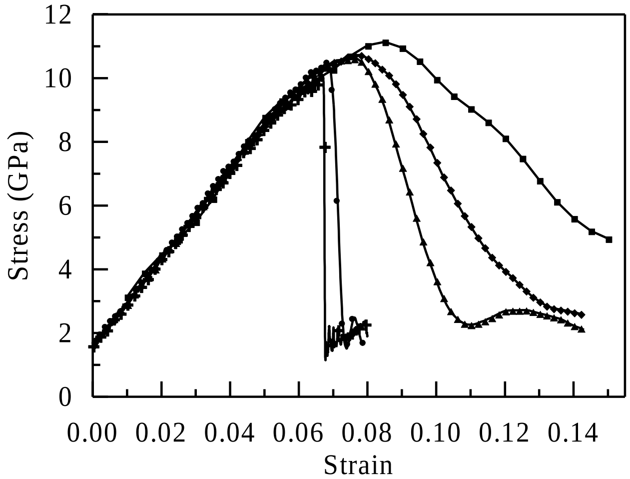

Figure 9. Stress-strain curve for 5 different strain rates at 300 K temperature. The + symbol $1x10^{8}s^{-1}$, • symbol $1x10^{9}s^{-1}$, ▲ symbol $1x10^{10}s^{-1}$, ♦ symbol $2x10^{10}s^{-1}$ and ■ symbol $5x10^{10}$ s^{-1} shows strain ratios.

Similarly, the same stress is required to nucleate twinning in the same crystal directions even at different strain rates. Therefore, it can be said that the modulus of elasticity is independent of the strain rate (Li and Han 2017). Young's modulus was determined as 144.23 GPa as a result of regression analysis of linear region where elastic deformation occurred in the stress-strain graph. However, the yield strain for the Fe nano wire is 10.11 GPa, 10.79 GPa, 11.09 GPa for $1x10^{8}$ s^{-1}, $1x10^{9}$ s^{-1}, $1x10^{10}$ s^{-1}, $2x10^{10}$ s^{-1} and $5x10^{10}$ s^{-1}, respectively. , 11.24 GPa and 11.82 GPa. It is clearly seen that the yield stress increases with the increase in the strain rate. It can be said that with the increase of the strain rate, higher stress is needed for the model system to undergo plastic deformation.

4. CONCLUSION

The stress behaviours under different temperatures and strain rates along the direction of the α-Fe nanowire system [100], where inter-atomic interactions are represented by the EAM potential function, were investigated using MD simulation method. It was determined that the temperature and strain rate affected the mechanical behaviour of the model system. The increase in temperature decreases the Young's modulus because the large amplitude thermal vibrations of the atoms at high temperatures significantly weaken the bond forces. However, it has been determined that the yield stress decreases with increasing temperature and decreasing strain rate. Different strain rates have no effect on the Young' s modulus of the nanowire within the elastic zone boundaries. It can be stated that the plastic deformation in the nanowire occurs due to the nucleation and propagation of twinning.

Author contributions

Sefa Kazanç: Methodology, Software, Writing-Original draft preparation, Software, Validation. **Canan Aksu Canbay:** Visualization, Investigation, Writing-Reviewing and Editing.

Conflicts of interest

The authors declare no conflicts of interest.

REFERENCES

Agrait N, Rodrigo J G, Sirvent C & Vieira S (1993). Atomic-scale connective neck formation and characterization. Phys. Rev. B, 48, 8499.

Agrait N, Rubio G & Vieira S (1995). Plastic Deformation of Nanometer-Scale Gold Connective Necks. Phys. Rev. Lett., 74, 3995.

Alavi A, Mirabbaszadeh K, Nayebi P et al. (2010). Molecular dynamics simulation of mechanical properties of Ni–Al nanowires. Computational Materials Science, 50, 10–14.

Arnold M S, Avouris P, Pan Z W & Wang Z L (2003). Field-effect transistors based on single semiconducting oxide nanobelts. Journal of Physical Chemistry B, 107(3), 659-663

Bañuelos E U, Aburto C C & Arce A M (2016). A common neighbor analysis of crystallization kinetics and excess entropy of charged spherical colloids. The Journal of Chemical Physics, 144, 094504.

Bonny G, Castin N & Terentyev D (2013). Interatomic potential for studying ageing under irradiation in stainless steels: the FeNiCr model alloy. Model. Simul. Mater. Sci. Eng., 21, 085004.

Cai J & Ye Y Y (1996). Simple analytical embedded-atom-potential model including a long-range force for fcc metals and their alloys. Phys. Rev. B, 54, 8398.

Da Silva, E Z da Silva AJR & Fazzio A (2001). How Do Gold Nanowires Break? Phys. Rev. Lett., 87, 256102.

Da Silva E Z, Novaes F D & da Silva A J R (2004). Theoretical study of the formation, evolution, and breaking of gold nanowires. Phys. Rev. B, 69, 115411.

Davoodi J & Ahmadi M (2012). Molecular Dynamics simulation of elastic properties of CuPd nanowire. Composites: Part B, 43, 10-14.

Diao J, Gall K, Dunn ML (2004). Yield Strength Asymmetry in Metal Nanowires Nano Lett, 4, 1863–1867.

Diao J, Gall K, Dunn M L & Zimmerman J A (2006). Atomistic simulations of the yielding of gold nanowires. Acta Materialia, 54, 643-653.

Duan X & Huang Y (2003). Single-nanowire electrically driven lasers. Nature, 421, 241-245.

Engin C & Urbassek H M (2008). Molecular-dynamics investigation of the fcc-bcc phase transformation in Fe. Computational Materials Science, 41, 297-304.

Fanga R, Wanga W, Guoa L, Zhanga K, Zhanga X & Lib H (2020). Atomic insight into the solidification of Cu melt confined in graphene Nanoslits. Journal of Crystal Growth, 532, 125382.

Finnis M W & Sinclair J E (1984). A simple empirical N-body potential for transition metals. Philosophical Magazine, 50, 45-55.

Gan Y & Chen J K (2009). Molecular dynamics study of size, temperature and rate dependent thermomechanical properties of copper nanofilms. Mechanics Research Communications, 36, 838-844.

Gao Y, Sun Y, Yang X, Sun Q & Zhao J (2016). Investigation on the mechanical behaviour of faceted Ag nanowires. Molecular Simulation, 42(3), 220-228.

Godet J, Pizzagalli L & Guillotte M (2019). Molecular dynamics study of mechanical behavior of gold-silicon core-shell nanowires under cyclic loading. Acta Materialia, 5, 100204.

Horstemeyer M F, Baskes M I & Plimpton S J (2001). Length scale and time scale effects on the plastic flow of fcc metals. Acta Mater, 49, 4363-4374.

Huang H M & Mao S (2001) Room-temperature ultraviolet nanowire nanolasers Science, 292, 5523.

Ikeda H, Qi Y, Cagin T, et al. (1999). Strain rate induced amorphization in metallic nanowires. Phys. Rev. Lett. 82, 2900-2903.

Jacobus K, Sehitoglu H & Balzer M (1996). Effect of stress state on the stress-induced martensitic transformation in polycrystalline Ni-Ti alloy. Metallurgical and Materials Transactions A, 27(A), 3066-3073.

Jing Y, Meng Q & Zhao W (2009). Molecular dynamics simulations of the tensile and melting behaviours of silicon nanowires. Physica E, 41, 685-689.

Karimi M, Stapay G, Kaplan T & Mostoller M (1997). Temperature dependence of the elastic constants of Ni: reliability of EAM in predicting thermal properties. Modelling Simul. Mater. Sci. Eng., 5, 337.

Kazanc S, Ozgen S & Adiguzel O (2003). Pressure effects on martensitic transformation under quenching process in a molecular dynamics model of NiAl alloy. Physica B, 334, 375-381.

Kazanc S & Ozgen S (2004). The Changes of barrier energy in fcc-bcc phase transformation by shear stresses. G.U. Journal of Science, 17(2), 35-42.

Kim C, Gu W, Briceno M, Robertson I M, Choi H & Kim K (2008). Copper Nanowires with a Five-Twinned Structure Grown by Chemical Vapor Deposition. Adv Mater., 20, 1859-1863.

Koh S J A, Lee H P, Lu C & Cheng Q H (2005). Molecular dynamics simulation of a solid platinum nanowire under uniaxial tensile strain: Temperature and strain-rate effects. Phys. Rev. B, 72, 085414.

Krüger D, Fuchs H, Rousseau R, Marx D & Parrinello M (2002). Pulling Monatomic Gold Wires with Single Molecules: An Ab Initio Simulation. Phys. Rev Lett., 89, 186402.

LAMMPS Molecular Dynamics Simulator, http://lammps.sandia.gov/, (Access date:02.01.2021).

Landman U, Luedtke W D, Salisbury B E & Whetten R L (1996). Reversible Manipulations of Room Temperature Mechanical and Quantum Transport Properties in Nanowire Junctions.Phys. Rev. Lett., 77, 1362.

Lee K, Wu Z, Chen Z, Ren F, Pearton S J & Rinzler A G (2004). Single wall carbon nanotubes for p-type ohmic contacts to GaN light-emitting diodes. Nano Lett., 4, 911-914.

Legoas S B, Galvao D S, Rodrigues V & Ugarte D (2002). Origin of Anomalously Long Interatomic Distances in Suspended Gold Chains. Phys. Rev. Lett., 88, 076105.

Li J, Hu L, Wang L, Zhou Y, Gruner G & Marks T J (2006). Organic light-emitting diodes having carbon nanotube anodes, Nano Lett., 6, 2472-2477.

Li S, Ding X, Deng J et al. (2010). Superelasticity in bcc nanowires by a reversible twinning mechanism. Phys. Rev. B, 82, 205435.

Li L & Han M (2017). Molecular dynamics simulations on tensile behaviors of single-crystal bcc Fe nanowire: effects of strain rates and thermal environment. Appl. Phys. A, 123, 450.

Liang W W & Zhou M (2003). Size and strain rate effects in tensile deformation of Cu nanowires. Nanotechnology, 2, 452-455.

Liang W, Zhou M & Ke F (2005). Shape Memory Effect in Cu Nanowires. Nano Lett., 5, 2039.

Malins A, Williams S R, Eggers J & Royall C P (2013). Identification of structure in condensed matter with the topological cluster classification. The Jouurnal of Chemical Physics, 139, 234506.

Marszalek P E, Greenleaf W J, Li H B, Oberhauser A F & Fernandez J M (2000). Atomic force microscopy captures quantized plastic deformation in gold nanowires. PNAS, 97, 6282-6286.

Mishin Y, Mehl M, Papaconstantopoulos D, Voter A & Kress J (2001). Structural stability and lattice defects in copper: Ab initio, tight-binding, and embedded-atom calculations. Phys. Rev. B, 63, 224106.

Olsson P, Wallenius J, Domain C, Nordlund K & Malerba L (2005). Two-band modeling of α-prime phase formation in Fe-Cr. Phys. Rev. B, 72, 214119.

Park HS, Zimmerman JA (2005). Modeling inelasticity and failure in gold nanowires Phys Rev B, 72, 054106.

Park H S & Ji C (2006). On the thermomechanical deformation of silver shape memory nanowires. Acta Mater., 54, 2645.

Parrinello M & Rahman A (1980). Crystal structure and pair potentials: a molecular-dynamics study. Physical Review Letters, 45(11), 1196.

Parrinello M & Rahman A (1981). Polymorphic transitions in single crystals: a new molecular dynamics method. J. Appl. Phys., 52(12), 7182-7190.

Pasquier A, Unalan H E, Kanwal A, Miller S & Chhowalla M (2005). Conducting and transparent single-wall carbon nanotube electrodes for polymer-fullerene solar cells. Appl. Phys. Lett., 87, 203511.

Rawat S & Mitra N (2020). Twinning, phase transformation and dislocation evolution in single crystal titanium under uniaxial strain conditions: A molecular dynamics study. Computational Materials Science, 172, 109325.

Rodrigues V, Fuhrer T & Ugarte D (2000). Signature of atomic structure in the quantum conductance of gold nanowires. Phys. Rev. Lett., 85, 4124.

Saha S, Motalab M & Mahboob M (2017). Investigation on mechanical properties of polycrystalline W nanowire. Comp. Mater. Sci., 136, 52-59.

Saitoh K I & Liu W K (2009). Molecular dynamics study of surface effect on martensitic cubic-to-tetragonal transformation in Ni-Al alloy. Computational Materials Science, 46, 531-544.

Sainath G & Choudhary B K (2016). Orientation dependent deformation behavior of bcc iron nanowires. Computational Materials Science, 111, 406–415.

Salehinia I & Bahr D F (2014). Crystal orientation effect on dislocation nucleation and multiplication in fcc single crystal under uniaxial loading. International Journal of Plasticity, 52, 133–146.

Schiotz J, Tolla F D D & Jacobsen K W (1998). Softening of nanocrystalline metals at very small grain sizes. Nature, 391, 561-563.

Stukowski A (2012). Structure identification methods for atomistic simulations of crystalline materials. Modelling and Simulation in Materials Science and Engineering, 20, 045021.

Suresh S & Li J (2008). Deformation of the ultra-strong. Nature, 456, 716–717.

Sutton A P & Chen J (1990). Long-range Finnis-Sinclair potentials. J. Philosophical Magazine Letter, 61, 139-146.

Tschoppa M A & McDowella D L (2008). Influence of single crystal orientation on homogeneous dislocation nucleation under uniaxial loading. Journal of the Mechanics and Physics of Solids, 56, 1806–1830.

Wadley H N G Zhou X, Johnson R A & Neurock M (2001). Mechanism, models and methods of vapor deposition. Progress in Materials Science, 46, 329-377.

Wang J, Huang Q A & Yu H (2008). Size and temperature dependence of Young's modulus of a silicon nano-plate. J. Phys. D: Appl. Phys., 41, 165406.

Wang P, Chou W, Nie A, Huang Y, Yao H & Wang H (2011). Molecular dynamics simulation on deformation mechanisms in body-centered-cubic molybdenum nanowires Journal of Applied Physics, 110, 093521.

Wen Y H, Zhu Z Z & Zhu R Z (2008). Molecular dynamics study of the mechanical behavior of nickel nanowire: Strain rate effects. Computational Materials Science, 41, 553-560.

Wen Y H, Zhang Y, Wang Q, Zheng J C & Zhu Z Z (2010). Orientation- dependent mechanical properties of Au nanowires under uniaxial loading. Computational Materials Science, 48, 513-519.

Wu Y H, Zhou Z M & Wang Y L (2004). Studies on effects of aluminum compounds on aluminum contents inserum and brain of mice with high performance capillary electrophoresis. Nature, 29(1), 61.

Wu H A (2006). Molecular Dynamics study of the mechanism of metal nanowires at finite temperature. European Journal of Mechanics A/Solids, 25, 370-377.

Voter A F & Chen S P (1987). Accurate Interatomic Potentials for Ni, Al, and Ni_3Al. Mat. Res. Soc. Symp. Proc., 82, 175.

Zhanga L, Lua C, Tieua K, Sua L, Zhaoa X & Peib L (2017). Stacking fault tetrahedron induced plasticity in copper single crystal. Materials Science and Engineering A, 680, 27–38.

Zhang L, Lu C & Tieu A K (2018). Nonlinear elastic response of single crystal Cu under uniaxial loading by molecular dynamics study. Materials Letters, 227, 236-239.

Zhu J & Shi D (2011). Reorientation mechanisms and pseudoelasticity in iron nanowires. J. Phys. D Appl. Phys., 44, 055404.

Turkish Journal of Engineering
https://dergipark.org.tr/en/pub/tuje
e-ISSN 2587-1366

Digital elevation modeling using artificial neural networks, deterministic and geostatistical interpolation methods

Esra Aslı Çubukçu *1, **Vahdettin Demir** 1, **Mehmet Faik Sevimli** 1

1*KTO Karatay University, Faculty of Engineering and Natural Sciences, Civil Engineering Department, Konya, Turkey*

Keywords
Digital Elevation Models
Artificial Neural Network
Samsun
Geostatistical methods
Mert River Basin

ABSTRACT

The digital elevation model (DEM) is the name given to a digital structure used to indicate the surface. Determination of features such as elevation, basin slope and basin area are very important in engineering applications. These properties are determined by the DEM and their power to represent accuracy or truth is vital in engineering applications. In addition to the latitude (X), longitude(Y) coordinate information, altitude information is required, and intermediate values are determined by different methods for DEM. In this study, Mert River Basin Samsun (Turkey) was chosen as the application area. Heights are estimated from X, Y coordinate information. Three different Artificial Neural Networks, IDW and Kriging methods were used. Artificial Neural Networks (ANN) were analyzed with three different inputs. These are: (i) x coordinate information; (ii) y coordinate information; (iii) It is in the form of x and y coordinate information and are used Radial Based Artificial Neural Network, Multilayer Artificial Neural Network and Generalized Artificial Neural Network. X and Y coordinate information was used in IDW and Kriging interpolation methods. Results were evaluated using Coefficient of Determination (R^2), Mean Absolute Error (MAE) and Root Mean Square Error (RMSE) as comparison criteria. According to the modeling results: It was observed that the results of all methods reached a sufficient level of accuracy. Kriging method was found to be the most successful model, followed by IDW and ANN.

1. INTRODUCTION

Resource management, urban and rural planning, transportation planning, agriculture, forestry, watershed management, disaster risk assessment etc. Digital Elevation Model (DEM) is needed in many studies. In addition, basic topographic and morphological parameters derived from the DEM are needed. At the present time, Geographical Information Systems (GIS) enables the creation of DEM and the automatic derivation of topographic and morphological parameters from DEM (Fang and Wu 2007; Gocic and Trajkovic 2013; Klingseisen et al. 2008; Papik et al. 1998; Parlak et al 2006; Yan 2008, Yakar 2008; Yakar et al. 2009).

DEM is the numerical representation of the topography. The DEM contains some errors and uncertainties depending on the data generated and the model used. These errors systematically affect the details of the land derived from the DEM. For this reason, the correctness of the DEM must be investigated for the adequacy of the work to be performed (Usul and Paşaoğulları 2004; Wang et al. 2006).

Two methods are generally used when creating DEM. The first is the 3-dimensional images obtained by the remote sensing method. These images are a wide range of high precision data. Also, the relative and absolute precision accuracy is very low. Radar and laser scanners and other sensor are also available to achieve high precision, high resolution DEM. These transactions are generally costly. The second method is to scan the existing topography, using digital contour lines; access to the height data generated by DEM, data such as high efficiency, low cost, topographic maps related to the experiment, measuring the use of this method and achieving the desired results (Yan 2008).

When the important studies on numerical height

---

* **Corresponding Author**

*(cubukcuasli@gmail.com) ORCID ID 0000-0003-4159-205X
(vahdettin.demir@karatay.edu.tr) ORCID ID 0000-0002-6590-5658
(mehmet.faik.sevimli@karatay.edu.tr) ORCID ID 0000-0002-4676-8782

Cite this article

Çubukçu E A, Demir V & Sevimli M F (2022). Digital elevation modeling using artificial neural networks, deterministic and geostatistical interpolation methods. Turkish Journal of Engineering, 6(3), 199-205

Research Article / DOI: 10.31127/tuje.889570

Received: 02/03/2021; Accepted: 02/07/2021

modeling are examined; Demirkesen (2003) created the digital elevation model using satellite images of the Cumberland Drainage Basin in Kentucky, USA (Demirkesen 2003). Arslanoğlu and Özçelik (2005) modeled numerical heights using the contour lines of 1 / 25.000 scaled maps (Arslanoğlu and Özçelik 2005). Akçın et al. (2005) modeled the seabed topography with Artificial Neural Networks (ANN) (Akçın et al. 2005). Şahin and Yakar (2007) have created a numerical elevation model for 2 different regions from aerial photographs, IKONOS satellite images, elevation curves and radar scans. (Şahin and Yakar 2007). Karan et al. (2004) made surface modeling with Object-Information-Based Combinational-Photogrammetry technology using three-dimensional topographic data, two-dimensional aerial images and satellite images. (Karan et al. 2004). Hani et al. (2011) created the numerical height model with Granulometric analysis model (Hani et al. 2011). Çakır and Yılmaz (2014) made surface modeling using polynomials, multiquadric interpolation, feed forward neural network and ANFIS methods (Çakır and Yılmaz 2014). Schulmann et al. (2015) made topographic surface modeling using Landsat satellite image data and shadow and vision technique (Schulmann et al. 2015). Niederheiser et al. (2018) created a numerical model by using terrestrial image matching method to obtain the topographic features of the Alps region (Niederheiser et al. 2018). Khosa et al. (2019) used elevation modeling from land surface, empirical and satellite-based models using on-site observations in a semi-arid region in South Africa (Khosa et al. 2019). Zhang et al. (2020) made surface modeling with stochastic and micro grinding processes (Zhang et al. 2020). Demir and Ülke Keskin (2020) made surface modeling with multi-layered artificial neural network method and regression methods from ANN methods (Demir and Ülke 2020). In addition, surface models based on coordinate transformation are also made (Güllü et al. 2011; Konakoğlu et al. 2016; Lei and Qi 2010; Tierra et al. 2008)

Öztürk et al. (2010) have studied digital elevation data sources and structures, sources of errors in Grid DEM, observation of slope, view, flow direction, flow sum, basin-sub basin, drainage network from GIS and DEM, and effect of grid-DEM's resolution on self-derived topographic and morphological data in their study (Öztürk et. al. 2010). Demirkesen (2003) made hydrological analysis by using the DEM data obtained from the satellite images belonging to that region in order to help the land arrangement and planning in urban and rural areas. As a result of the analysis, the flood zones were determined depending on the rainfall amount to the region (Demirkesen 2003). Çakır (2015) used a functional test surface as an application area. The surface created is a rugged terrain consisting of mountains and pits. After specifying 80 fulcrums and 30 test points for this test surface in random distribution, optimal DEM models to represent the surface have been developed with Polynomials, Multicuadic Interpolation, Feedforward Artificial Neural Networks (F-ANN) and Adaptive Network Based Fuzzy Inference Systems (ANFIS). As a result of their work, F-ANN and ANFIS methods are more successful than polynomials and multicharistic interpolation methods in determining DEM (Çakır 2015). Yaprak and Arslan (2008) investigated the usability of deterministic and Kriging interpolation methods in surface modeling to determine geoid with GPS and Leveling method. Gümüş and Şen (2017) obtained surface models of lands with different topographic features using IDW and Kriging methods and interpreted the results using analysis of variance (ANOVA). In the current study, the 14362 digital elevation model data are used. 14362 data were randomly sorted in excel. Then A (as training data 90% - as testing data 10%), B (80% -20%), C (70% -30%), D (60% -40%), E (50% -50%) were divided into training-test packages. Coordinate information was prepared as single x, single y and x, y, respectively, and z output data was produced. The objective of the study is to estimate the elevation point at any ungauged location in the Mert River. Artificial Neural Network models and two different well- known interpolation methods (IDW and Kriging) are used for this purpose.

2. MATERIALS AND METHOD

2.1. Material

The Mert River (latitude: 41.279 and longitude: 36.352) located in the central district of Samsun and poured into the Black Sea was selected as the study area. The study area is shown in Figure 1.

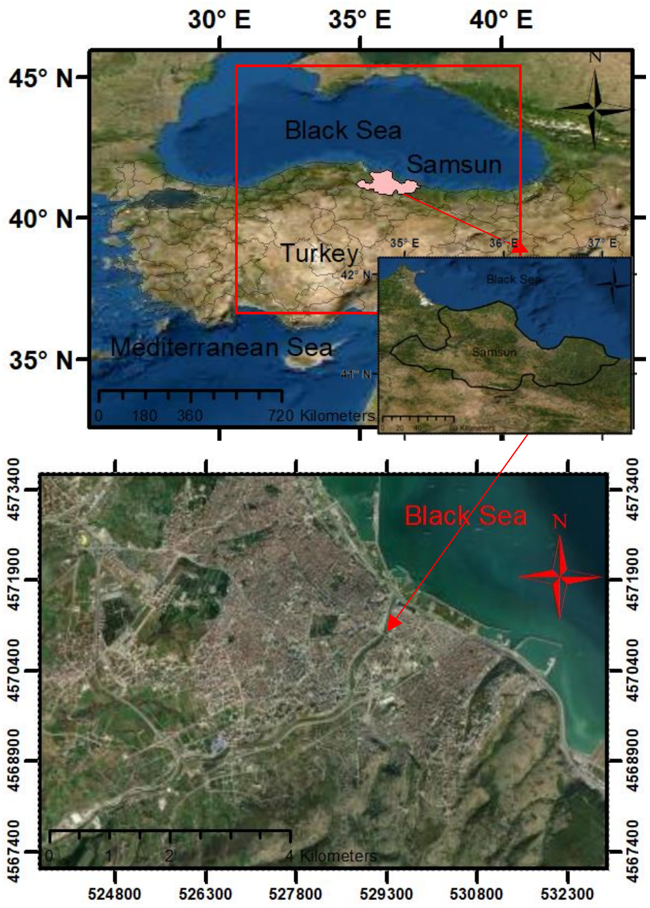

Figure 1. Study Area

The data modeled in the study is the current map height data obtained from the central municipalities of Samsun (Canik-Ilkadım). These data are defined in the

ED-50 coordinate datum with a scale of 1/1000 and were obtained from aerial photographs.

Table 1. Statistical information of data

	X	Y	Z
Number of Data (N)	14362	14362	14362
Minimum value (m)	4568584.581	528296.486	0.07
Maximum value (m)	4572051.156	530920.692	238.130
Skewness Coefficient	0.008	0.0579	1.429
Standard deviation	889.701	686.639	52.355
Average	4570318.492	529557.428	43.688

2.2. Methods

2.2.1. Multi-Layered Artificial Neural Network

Multi-layer Artificial Neural Networks (MANN) consists of an input layer, one or more hidden (intermediate) layers, and an output layer where information is input. MANN has transitions between layers called forward and backward propagation. In the forward propagation phase, the output and error value of the network are calculated.

In the back-propagation phase, the inter-layer link weight values are updated to minimize the calculated error value (Arı and Berberler 2017). The MANN model uses the backpropagation learning algorithm, which is the generalization of the least squares algorithm in linear perception. Back propagation consists of backward steps in which the output of the network is determined by the algorithm that defines advanced forward information and the error caused by the emergence of the weights is reduced. In the feed-forward step, the inputs of the training set are sent to the input layer of the network. The input layer contains neurons that receive these inputs. Therefore, the number of neurons in the input layer must be the same as the number of input values in the data set. Neurons in the input layer transmit the input values directly to the hidden layer. Each neuron in the hidden layer calculates the total value by adding the threshold value to the weighted input values and multiplies them with an activation function, then transmits them to the next layer or directly to the output layer. The weights between the layers are initially chosen randomly. The error value is calculated by comparing the output values of the network with the expected output values. The multi-layer sensor model consists of an input (X_1, X_2, X_3,….., X_n), a hidden, and an output layer (Y). Each layer may also have one or more processing elements. The processor elements in the input layer act as a buffer that distributes the input signals to the processor elements in the intermediate layer. The intermediate layer processor elements use the outputs of the previous layer as inputs. With all inputs, weights are multiplied and total. This value is then passed through a transfer function and the output value of that neuron is calculated. These operations are repeated for all the processor elements on this floor. These operations are repeated for all processor elements in this layer. The processor elements in the output layer also act as intermediate layer elements and the network output values are calculated. This model is also known as feed forward ANN's as the information flow is in the forward direction (Gemici et al. 2013). Different learning algorithms are used to train the network The activation function processes the net input to the cell and determines the output that the cell will generate for that input. One of the most used activation functions in applications is the Sigmoid-type activation function (Gemici et al. 2013). The formula of the function is shown in Equation (1). The most active site of the function is between 0.2 and 0.8.

$$y = F(v) = \frac{1}{1+e^{-v}} = \frac{1}{2}[\tanh(\frac{v}{2}) - 1] \tag{1}$$

2.2.2. Radial Based Artificial Neural Networks

Radial-based ANN (RBANN) concept was introduced into the literature in 1988 by Broomhead and Lave. ANN model and Radial-based functions have been developed by considering the effect-response states of neuron cells in human nervous system (Okkan and Dalkılıç 2012). It is possible to see the The digital elevation model (DEM) is a numerical structure used to indicate the surface. It is possible to view the training of RBANN models as a curve fitting approach in multidimensional space (Partal et al., 2008; Poggio and Girosi 1990). Thus, the educational performance of the RBANN sample turns into a problem of finding the closest result to the data in the output vector space and thus an interpolation problem (Okkan and Dalkılıç 2012). RBANN structure generally consists of input layer, hidden layer and output layer similar to ANN structure. However, unlike other ANNs, the data is subjected to radial based activation functions and a nonlinear cluster analysis when passing from the input layer to the hidden layer. The structure between the hidden layer and the output layer functions as in other ANN types and the actual training takes place in this layer. In the RBANN model we used, the problem was solved with purelin function.

2.2.3. Generelization Regresion Artificial Neural Network

The Generalized Regression Artificial Neural Network (GRANN) proposed by Specht (1991) does not require an iterative training procedure as in the back-propagation method (Sürel, 2006). GRANN estimates any function between input and output vectors using training data. As the training set expands, the prediction error decreases to zero (Alp and Cığızoğlu, 2004). As known by definition, regression estimates the most probable value of a dependent variable based on the independent variable x, given the training set x. The regression method estimates y to minimize common square error. GRANN is a method that estimates the common probability density function of x and y when a training set is given. The system is generally ideal since the Common Density Function is obtained without any pre-acceptance from the data (Alp & Cığızoğlu, 2004; Kesikoğlu et. al. 2020; Öztürk et. al. 2022). If the common probability density function of f (x,

y) is known, the regression of the dependent y variable according to the independent x variable is given in Equation (2).

$$E\left[y|X\right]=\frac{\int_{-\infty}^{\infty} yf(X,y)dy}{\int_{-\infty}^{\infty} f(X,y)dy} \qquad (2)$$

2.2.4. Inverse Distances Weighted

Inverse Distance Weighted (IDW) is one of the most preferred non-geostatistics methods. This method is an interpolation technique used to determine the cell values of unknown points using the values of known sample points. Since it produces estimates only from neighboring points, it makes a local intermediate value estimation. The method is based on the fact that the nearby points have a greater weight on the surface to be interpolated than the distant points. The cell value is calculated by observing the various points moving away from the cell of interest and depending on the increase in distance. The predicted values are a function of the distance and the size of the points in the neighboring neighborhood, and as the distance increases, the importance and effect on the cell to be estimated decreases (Taylan and Damçayırı, 2016).

$$F(x,y)=\sum_{i=1}^{n} w_i f_i \qquad (3)$$

$$w_i=\frac{h_i^{-p}}{\sum_{j=1}^{n} h^{-p}{}_i} \qquad (4)$$

The weights used to estimate the function are expressed as any exponent of the distance in inverse proportion to the distance.

In the Equations 3-4; (Krige, 1951)

p; Known as force parameter and show exponent,

h_i; Spatial distance between sample points and interpolated points,

w_i; Weights are doing and the sum of the values must be 1.

f_i= Known altitude values.

2.2.5. Kriging Method

The kriging method is a geostatistical interpolation method that estimates the optimum values of data at other points using data from known nearby points. The most important feature that distinguishes Kriging from other methods is that a variance value can be calculated for each estimated point or area. This is a measure of the reliability of the predicted value (Yaprak and Arslan, 2008).

The estimation by the Kriging interpolation method has two stages: (i) adaptation to a model: creation of variograms and covariance functions, this is based on the autocorrelation model and (ii) estimation: estimation of the unknown (Öztürk and Kılıç 2016).

Equation 5 used in kriging;

$$N_p=\sum_{i=1}^{n} P_i * N_i \qquad (5)$$

Where;

n = Number of points in the model,

N_i = N_p, The geoid undulation values used in the calculation of

N_p = The required undulation value

P_i = The weight values for each N_i value used in the calculation of N_i.

Kriging technique provides more objective results than other estimation techniques and also gives minimum variance and standard deviation of estimation.

3. APPLICATIONS

Root Mean Square Error (RMSE), Mean Absolute Error (MAE) and determination coefficient (R^2) were used as comparison criteria. The formulas of the criteria are given in the Equations 6-7-8.

$$RMSE=\sqrt{\frac{1}{N}\sum_{i=1}^{N}(Z_o-Z_e)^2} \qquad (6)$$

$$MAE=\frac{1}{N}\sum_{i=1}^{N}\left|Z_o-Z_e\right| \qquad (7)$$

$$R^2=\left(\frac{N*\left(\sum Z_o*Z_e\right)-\left(\sum Z_o\right)*\left(\sum Z_e\right)}{\sqrt{\left(N*\sum Z_o^2\right)-\left(\sum Z_o\right)^2*\left(N*\sum Z_e^2\right)-\left(\sum Z_e\right)^2}}\right)^2 \qquad (8)$$

The distribution of the data used in the analysis is different for each package. Packages A (training data 90% - test data 10%), B (80% - 20%), C (70% - 30%), D (60% - 40%), E (50% - 50%). Table 2 shows the distributions.

Table 2. Table of data distributions

Packages	Training Data %	Test Data %
A	90	10
B	80	20
C	70	30
D	60	40
E	50	50

Table 3-7 shows the analysis results according to the comparison criteria of the test set of the A, B, C, D, E package respectively.

All analysis results are given in the tables below. When the results were examined, the Kriging method was the first to reach the best results in both training and test data in all packages. RMSE = 1.121, MAE = 0.635, R^2 = 0.999 in the B package. Secondly, the IDW, GRNN and RBANN method has achieved the best result. Finally, the MANN method solves the problem most accurately.

Table 3. A pack test data results

Test	Method	Input		
A (10%)		(i; x)	(i; y)	(ii; x,y)
RMSE	MANN	32.878	45.769	18.430
	RBANN	35.406	29.130	10.224
	GRANN	**32.699**	**45.634**	**2.357**
	Average	33.661	40.178	10.337
MAE	MANN	24.182	35.126	12.766
	RBANN	28.225	23.882	6.794
	GRANN	**24.036**	**34.951**	**1.278**
	Average	25.481	31.320	6.946
R^2	MANN	0.595	0.213	0.873
	RBANN	0.529	0.681	0.961
	GRANN	**0.599**	**0.218**	**0.998**
	Average	0.574	0.371	0.944

Table 4. B pack test data results

Test	Method	Input		
B (20%)		(i; x)	(i; y)	(ii; x,y)
RMSE	MANN	33.515	46.934	18.326
	RBANN	36.323	29.447	10.376
	GRANN	**33.360**	**46.762**	**2.315**
	Average	34.399	41.048	10.339
MAE	MANN	24.633	35.784	12.774
	RBANN	28.230	24.027	6.677
	GRANN	**24.480**	**35.603**	**1.282**
	Average	25.781	31.805	6.911
R^2	MANN	0.598	0.211	0.880
	RBANN	0.528	0.690	0.961
	GRANN	**0.602**	**0.217**	**0.998**
	Average	0.576	0.373	0.947

Table 5. C pack test data results

Test	Method	Input		
C (30%)		(i; x)	(i; y)	(ii; x,y)
RMSE	MANN	33.334	47.325	18.188
	RBANN	36.303	34.099	10.319
	GRANN	**33.222**	**47.157**	**2.292**
	Average	34.286	42.860	10.267
MAE	MANN	24.506	36.097	12.660
	RBANN	28.853	27.844	7.085
	GRANN	**24.267**	**35.963**	**1.279**
	Average	25.875	33.301	7.008
R^2	MANN	0.607	0.208	0.883
	RBANN	0.534	0.589	0.962
	GRANN	**0.609**	**0.213**	**0.998**
	Average	0.583	0.337	0.948

Table 6. D pack test data results

Test	Method	Input		
D (40%)		(i; x)	(i; y)	(ii; x,y)
RMSE	MANN	33.316	46.948	18.080
	RBANN	350.732	33.814	9.902
	GRANN	**33.154**	**46.745**	**2.711**
	Average	139.067	42.502	10.231
MAE	MANN	24.437	35.847	12.554
	RBANN	308.732	27.552	6.438
	GRANN	**24.170**	**35.656**	**1.307**
	Average	119.113	33.018	6.766
R^2	MANN	0.600	0.207	0.882
	RBANN	0.101	0.589	0.965
	GRANN	**0.604**	**0.213**	**0.997**
	Average	0.435	0.336	0.948

Table 7. E pack test data results

Test	Method	Input		
E (50%)		(i; x)	(i; y)	(ii; x,y)
RMSE	MANN	33.279	46.857	17.947
	RBANN	35.675	35.816	10.349
	GRANN	**33.119**	**46.690**	**2.613**
	Average	34.024	43.121	10.303
MAE	MANN	24.377	35.925	12.542
	RBANN	28.268	27.698	6.890
	GRANN	**24.126**	**35.759**	**1.308**
	Average	25.590	33.127	6.913
R^2	MANN	0.599	0.206	0.884
	RBANN	0.540	0.536	0.961
	GRANN	**0.603**	**0.212**	**0.998**
	Average	0.581	0.318	0.947

Table 8. IDW and Kriging (KRI) methods data results

PACKS	Method	RMSE	MAE	R^2
A	IDW	1.638	0.881	0.999
	KRI	1.115	0.639	0.999
B	IDW	1.540	0.862	0.999
	KRI	1.121	0.635	0.999
C	IDW	1.129	0.651	0.999
	KRI	1.427	0.782	0.999
D	IDW	2.207	0.970	0.998
	KRI	1.763	0.677	0.998
E	IDW	2.158	1.012	0.998
	KRI	1.687	0.701	0.998

4. DISCUSSION

In the study of Demir and Keskin, multilayer artificial neural network and regression analysis were applied, and they used the data package as training (80%) and testing (20%). Multilayer neural network gave better results. However, a comparison between artificial neural networks was not carried out in the study. In this study, we have done modeling with different data packages using 3 different artificial neural network methods. According to the comparison criteria, the results of the generalized artificial neural network gave closer results than the multilayer artificial neural network. This study demonstrates the accuracy between training and testing, as well as supporting and enhancing the work of Demir and Keskin (Demir et al., 2020).

5. CONCLUSION

In the study, 14362 coordinate data were modeled using artificial neural network and interpolation techniques. IDW and Kriging methods from interpolation techniques, Radial Based Artificial Neural Network, Multilayer Artificial Neural Network and Generalized Artificial Neural Network methods were used in artificial neural network methods. Data in ANN A (90% -10%), B (80% -20%), C (70% -30%), D (60% -40%), E (50% -50%) rates of training and testing packages, and the study was carried out for three different input combinations.

When the results are examined; It was determined that the Kriging method gave the best modeling (with the least error) in the A, B, D and E packages, and the IDW method showed the best modeling in the C package. While the R^2 values are close to each other, error values are listed as follows; RMSE values of the results of the packet, the order is as follows; A package = 1.115 and B Package = 1,121 with Kriging C Package = 1.129 with IDW method. The ranking of MAE values are; A package = 0,639, B package = 0,635 with Kriging method, C Package= 0.651 with IDW. Then comes the Generalized Artificial Neural Network for all packets then Radial-Based Artificial Neural Network, and finally the Multilayer Artificial Neural Network.

While it is observed that the results of the modeling made with 2 inputs from the GRANN models give an R^2 value close to each other, the order is as follows; C package = 0.9982, B package = 0.9981 A package = 0.9979. RMSE values of the packets also gave similar results, the order is as follows; C package = 2.2924 B Package = 2.3146, A package = 2.3572. The ranking of MAE values are; A package = 1.2777, C package = 1.2788, B Package = 1.2820.

Author contributions

Esra Aslı Çubukçu: Methodology, Application, Writing-Original draft preparation, **Vahdettin Demir:** Conceptualization, Methodology, Application, Reviewing and Editing. **Mehmet Faik Sevimli:** Last Reviewing and Editing.

Conflicts of interest

The authors declare no conflicts of interest.

REFERENCES

Akçın H, Kutoğlu H Ş & Terlemezoğlu B (2005). Deniz dibi topoğrafyasının yapay sinir ağlarıyla modellenmesi. TMMOB Harita ve Kadastro Mühendisleri Odası 10. Türkiye Harita Bilimsel ve Teknik Kurultayı, Ankara, Turkey.

Alp M & Cığızoğlu K (2004). Modeling the precipitation-flow relationship with different artificial neural network methods. İTÜ Engineering Journal, 3(1), 80–88.

Arı A & Berberler M E (2017). Interface design for solving prediction and classification problems with artificial neural networks. Acta Infologica, 1(2), 55–73.

Arslanoğlu M & Özçelik M (2005). Improvement of numerical terrain elevation data. TMMOB Chamber of Surveying and Cadastre Engineers 10. Scientific and Technical Congress of Turkey, Ankara, Turkey.

Çakır L & Yılmaz N (2014). Polynomials, radial basis functions and multilayer perceptron neural network methods in local geoid determination with GPS/levelling. Meas. J. Int. Meas. Confed., 57, 148–153.

Çakır L (2015). Sayısal Yükseklik Modellerinde Klasik ve Esnek Hesaplama Yöntemlerinin Karşılaştırılması. TMMOB Harita ve Kadastro Mühendisleri Odası, 15. Türkiye Harita Bilimsel ve Teknik Kurultayı, Ankara, Turkey.

Demir V & Ülke Keskin A (2020). Height modeling with artificial neural networks (Samsun-Mert River Basin). Gazi Mühendislik Bilim. Dergisi, 6, 54–61.

Demirkesen A C (2003). Sayısal yükseklik modellerinin analizi ve sel basman alanlarının belirlenmesi. TUJK 2003 Yılı Bilimsel Toplantısı, Konya, Turkey.

Fang Y C & Wu B-W (2007). Neural network appication for thermal image recognition of low-resolution objects. J. Opt. A Pure Appl. Opt., 9(2), 134–144.

Gemici E, Ardıçoğlu M & Kocabaş F (2013). Akarsularda debinin yapay zekâ yöntemleri ile modellenmesi. Erciyes Üniversitesi Fen Bilimleri Enstitüsü Dergisi, Vol. 29, No. 2, pp 135–143.

Gocic M & Trajkovic S (2013). Analysis of changes in meteorological variables using Mann-Kendall and Sen's slope estimator statistical tests in Serbia. Glob. Planet. Change, 100, 172–182.

Güllü M, Yılmaz M, Yılmaz I & Turgut B (2011). Datum transformation by artificial neural networks for geographic information systems applications. International Symposium on Environmental Protection and Planning: Geographic Information Systems (GIS) and Remote Sensing (RS) Applications (ISEPP), İzmir, Turkey.

Gümüş K & Şen A (2017). Sayisal Yükseklik Modellerinin doğruluğunu etkileyen faktörlerin varyans analizi ile istatiksel olarak incelenmesi, Ömer Halisdemir Üniversitesi Mühendislik Bilimleri Dergisi, 6(1), 46-58.

Hani A F M, Sathyamoorthy D & Sagayan Asirvadam V (2011). Method for computation of surface roughness of digital elevation model terrains via multiscale analysis. Computers & Geosciences 37, 177–192.

Karan O, Eraslan A & Kurnaz S (2004). Topografik bilgiler ve uydu görüntü verilerini kullanarak 3 boyutlu alan tanıma sistemi. Havacılık Ve Uzay Teknoloji Dergisi, 4, 31–40.

Kesikoğlu H M, Çiçekli Y S & Kaynak T (2020). The identification of seasonal coastline changes from landsat 8 satellite data using artificial neural networks and k-nearest neighbor. Turkish Journal of Engineering (TUJE), 4(1), 47-56.

Khosa F V, Feig G T, Van der Merwe M R, Mateyisi M J, Mudau A E & Savage M J (2019). Evaluation of modeled actual evapotranspiration estimates from a land surface, empirical and satellite-based models using in situ observations from a South African semi-arid savanna ecosystem. Agric. For. Meteorol. l. 279, 1-20.

Klingseisen B, Metternicht G & Paulus G (2008). Geomorphometric landscape analysis using a semi-automated gıs-approach. Environmental Modelling & Software, 23(1), 109–121.

Konakoğlu B, Çakır L & Gökalp E (2016). 2D Coordinate transformation using artificial neural networks. ısprs - ınt. arch. photogramm. Remote Sens. Spat. Inf. Sci., 42, 183–186.

Lei W & Qi X (2010). The application of BP neural network in GPS elevation fitting. In Proceedings of the 2010 International Conference on Intelligent Computation Technology and Automation; IEEE, 698–701.

Niederheiser R, Rutzinger M, Bremer M & Wichmann V (2018). Dense ımage matching of terrestrial imagery for deriving high-resolution topographic properties of vegetation locations in alpine terrain. Int. J. Appl. Earth Obs. Geoinf., 66, 146–158.

Okkan U & Dalkılıç H Y (2012). Radyal tabanlı yapay sinir ağları ile kemer barajı aylık akımlarının modellenmesi. İMO Teknik Dergi, 5957–5966.

Özturk D & Kılıc F (2016). Geostatistical approach for spatial interpolation of meteorological data. Annals of the Brazilian Academy of Sciences, 88(4), 2121–2136.

Öztürk A, Allahverdi N & Saday F (2022). Application of artificial intelligence methods for bovine gender prediction. Turkish Journal of Engineering, 6(1), 54-62.

Öztürk D, Şişman A, Şişman Y & Maraş E E (2010). Coğrafi bilgi sistemleri ile sayısal yükseklik modelinden topoğrafik ve morfolojik özelliklerin üretilmesi. VI. Ulusal Coğrafya Sempozyumu, 37-46, Ankara, Turkey.

Papik K, Molnar B, Schaefer R, Dombovari Z, Tulassay Z, & Feher J (1998). Application of neural networks in medicine - A review. Med. Sci. Monit., 4(3), 538–546.

Parlak A, İslamoğlu Y, Yaşar H & Eğrisöğüt A (2006). Application of artificial neural network to predict specific fuel consumption and exhaust temperature for a diesel engine. Appl. Therm. Eng., 26(8–9), 824–828.

Partal T, Kahya E & Cığızoğlu K (2008). Yağış verilerinin yapay sinir ağları ve dalgacık dönüşümü yöntemleri ile tahmini. İTÜ Mühendislik Dergisi, 7(3), 73–85.

Poggio T & Girosi F (1990). Regularization algorithms for learning that are equivalent to multilayer networks. Science, 247(4945), 978–982.

Schulmann T, Katurji M & Zawar-Reza P (2015). Seeing through shadow: Modelling surface irradiance for topographic correction of Landsat ETM+ data. ISPRS J. Photogramm. Remote Sens., 99, 14–24.

Sürel A (2006). Genelleştirilmiş regresyon yapay sinir ağının su kaynakları mühendisliğinde kullanımı, Master Thesis, Istanbul Technical University, Istanbul, Turkey

Şahin İ & Yakar M (2007). Accuracy Assessment of the Effect of Digital Elevation Models Generated from Different Sources on Orthophoto. 45–59.

Taylan E D & Damçayırı D (2016). Isparta bölgesi yağış değerlerinin IDW ve Kriging enterpolasyon yöntemleri ile tahmini. Teknik Dergi, 27(3), 7551-7559.

Tierra A, Dalazoana R & De Freitas S (2008). Using an Artificial Neural Network to Improve the Transformation of Coordinates between Classical Geodetic Reference Frames. Computers & Geoscience, 34, 181–189.

Usul N & Paşaoğulları O (2003). Effect of scale and grid size for hydrological modeling. International Conference of GIS and Remote Sensing in Hydrology, Water Resources and Environment, 91-101.

Wang P, Du J, Feng X & Kang G (2006). Effect of Uncertainty of Grid DEM on TOPMODEL: Evaluation and Analysis. Chinese Geographical Science, 16(4), 320–326.

Yakar M (2008). Digital Elevation Model Generation By Robotic Total Station Instrument. Experimental Techniques, 33(2), 52 – 59.

Yakar M, Yilmaz H M & Yurt K (2009). The Effect Of Grid Resolution In Defining Terrain Surface. Experimental Techniques 34 (6), 23-29.

Yan L (2008). Based on the Triangular Grid Digital Elevation Model of the Terrain Modeling. World Academy of Science, Engineering and Technology, 4, 401–403.

Yaprak S & Arslan E (2008). Kriging yönteminin geoit modellemesinde kullanılabilirliğinin araştırılması, İtü Dergisi, 7(5), 51-62.

Krige D G (1951) A Statistical Approach to Some Mine Valuations and Allied Problems at The Witwatersrand. Master's thesis, University of Witwatersrand, Johannesburg, 272p

Zhang X, Yu T & Zhao J (2020). Surface generation modeling of micro milling process with stochastic tool wear. Precision Engineering, 61, 170–181.

Turkish Journal of Engineering – 2022; 6(3); 206-210

Turkish Journal of Engineering

https://dergipark.org.tr/en/pub/tuje

e-ISSN 2587-1366

Strengthening of fire damaged reinforced beams by using ferro cement

Al Amin*[1], **Shorup Chowdhury Tamal** [2], **A. K. M. Fayzul Bari** [1], **Milan Mazumder** [1], **Md. Ariful Hasan** [1]

[1]*European University of Bangladesh, Faculty of Civil Engineering, 2/4, Gabtoli, Mirpur, Dhaka-1216, Bangladesh*
[2]*Soil & Foundation Ltd., Assistant Engineer, Shamoli, Dhaka-1207, Bangladesh*

Keywords
Fire
Ferro cement
Weir mesh
Flexural strength
Erroneous design

ABSTRACT

Now-a-days repair and rehabilitation of the existing structures in developing countries has become solitary of the most thought-provoking tasks in Civil Engineering sector. Imperfections, fiasco and general distress in the structures can be the outcome of fundamental deficiency produced by inaccurate design, poor workmanship or overloading of the construction. It can also be instigated by corrosion, fire and natural calamities. A spoiled or distrait structure can be modernized to an acceptable level of performance at a reasonable cost by different approaches is called retrofitting. One of these techniques consists of strengthening fire damaged concrete beams by applying Ferro cement with wire mesh. Two types of Ferro cement with wire mesh are used with single layer and double layer in beam. One third point load test according to ASTM C78-02 is performed to measure the flexure performance of four specimens. The ultimate load carrying capacity for using the single layer Ferro cement strengthening, double layer Ferro cement strengthening showed an improvement of 46% and 72% respectively over the fire damaged specimens.

1. INTRODUCTION

Concrete is a stone like operational substantial with great load resounding capacity, improved structural performance, brilliant method and financial property. The excellent performance is accomplished by strengthening the core concrete with restriction. When the transversal strain of the concrete is better than that of the strengthening material, the shipping stress between the concrete and strengthening material proliferations with the axial load, which restrains the event of micro cracks in concrete. For this reason, the axially load carrying ability and distortion performance are significantly improved.

From several investigations it's been found that Ferro cement is a perfect substantial for reintegration as well as re-strengthening of structures for the reason that it progresses crack confrontation joint with great toughness, the power to be cast into any form, fast construction with no heavy machinery, small supplementary weight enforced and low cost of construction. In Bangladesh Ferro cement material is extensively utilized in repairing and strengthening of distressed structural elements of the buildings. This versatile material has enormous potentials as a protective covering of the structural elements against corrosion within the coastal areas of the country. It's documented that in Bangladesh conventional formwork normally contributes 20% to 25% of the value of ferroconcrete. Significant economic advantages may occur if the Ferro cement cover are often used as permanent formwork for ferroconcrete beams. Additionally, structural benefits could also be obtained if the Ferro cement layer are often made to act compositely with the concrete core of the support. Ferro cement may be a sort of thin-wall ferroconcrete commonly constructed of Portland cement mortar, reinforced with closely spaced layers of unremitting and comparatively minor diameter wire mesh. It's considered to be an extension of reinforced beam. Most of the research works regarding Ferro cement ferroconcrete beams are limited to the evaluation of the superior performance of those

---

* **Corresponding Author**

*(alamin.ce18@gmail.com) ORCID ID 0000-0001-6517-0105
(tamal.chowdhury555@gmail.com) ORCID ID 0000-0002-5058-2403
(fayzul.bari20@gmail.com) ORCID ID 0000-0002-6529-5933
(milaneng.duet@gmail.com(ORCID ID 0000-0002-9348-6753
(arifrainge@gmail.com) ORCID ID 0000-0002-5964-2089

Cite this article

Amin A, Tamal S C, Bari A K M F, Mazumder M & Hasan Md A (2022). Strengthening of fire damaged reinforced beams by using ferro cement. Turkish Journal of Engineering, 6(3), 206-210

Research Article / DOI: 10.31127/tuje.925199

Received: 22/04/2021; Accepted: 31/05/2021

beams as compared to the standard ferroconcrete beams. But the composite behavior of Ferro cement concrete technology with comparatively better mechanical goods and durability than normal ferroconcrete. Inside convinced loading restrictions, it acts as a constant elastic material and these limits are broader than of normal concrete Material.

The studies by presents the experimental performance of concrete when improved by great modulus of elasticity carbon FRP (Tepfers and De Lorenzis, 2003) That firming up attains a big intensification of both the concrete strength besides the axial strain ductility that are reliant on mostly on the lateral pressure provided by the FRP and on its axial severity (Rafeeqi et al. 2005). However, the upper the modulus of elasticity of the strengthening is the lower its deformability to disaster. When strengthening concrete with materials of various modulus of elasticity and of an equivalent lateral severity, the strengthening usefulness in terms of load ability and strain at failure is higher for the fabric of lower modulus of elasticity. Thus, the competence of ultralow modulus of elasticity materials like polypropylene is prophesied to be amazing parameter for strengthening.

1.1. OBJECTIVE

In this research, the suitability and effectiveness of the Ferro-cement strengthening system to repair RC beams damaged by heating are investigated. The particular objectives of the present study are as follows:

1. To oversee the effects of strengthening and evaluate experimentally the ultimate load carrying capacities of fire damaged reinforced concrete beam when it is retrofitted by ferro cement with wire mesh;
2. To compare the performance (load carrying capacities, deflection) of specimens at different state under one third point loading test.

1.2. LITERATURE REVIEW

Rcc beams to study the efficiency of visibly attached molded ferro cement plates in solidification beams display shear misery. The qualified efficiency of the attaching media (C-S mortar, epoxy) employed in attaching the molded F.C Plates to the ends of beams are calculated. Ferro cement is occupied on account of striking for this solicitation on its high lastingness, little load cheap in cost, better lifetime of action and exact valuation of the additional strength expanded (Anggawidjaja et. al. 2006).

Shear mode of disaster in beams is undesired mostly being a fragile disaster. Consequently, strength has been prepared by these people to discover the capacities of ferro cement in transporting the inelastic mode to yielding mode. Ferro cement shawl and similarly spread-out strips with one or two layers of woven square mesh are accessible and associated with RC beam designed as shear undersupplied in both (Choi 2008; Dai et al. 2011). These investigators from their studies had determined that the strengthened beam displayed a marked enhancement in enactment at facility load, significantly upgraded ductility at decisive with either a yielding shear catastrophe or ostensibly a conversion from shear to flexure mode of disaster. Besides ferro cement wraps are humbler than ferrrocement strips. Another thing of reputation inferred is that the augmentation in load resounding capability isn't significant, still is contemporary. Service range had been prepared to upsurge the rigorousness of strengthened beams and also decreases the crack width and rebound as associated with un-strengthened beam [Amin et al. 2021; Colombo and Felicity 2007).

The compressive strength of concrete may reduce up to 50% when the concrete is exposed to 600°C. At 800°C, the residual compressive strength of the concrete is only 20% of the original value. Furthermore, normal-strength concrete experiences a sharper loss in tensile splitting strength than compressive strength at 600°C. Exposure to high temperatures may also change the pore structure of concrete through pore structure coarsening, which leads to increased permeability but reduced durability of the concrete. After exposure to 600°C, the cumulative pore volume in normal-strength concrete increases twice. At temperatures higher than 600°C, extreme C-S-H gel dehydration and pore structure coarsening contribute to the strength loss of the concrete. Fires in concrete structures rarely result in serious global structural damage, and most of the damaged structures can be successfully reinstated. Therefore, repair of fire-damaged concrete structures is a more viable and economical option than demolition and rebuilding (Zahid et al. 2018).

2. METHODOLOGY

Total procedure is performed by a flow diagram which are shown in below;

The specimens are cast into wooden frame as beam. This casting process is measured because of the slight extent of beam cross section. Hand compaction is applied to dense the concrete with the use of a 16 mm (diameter) tamping rod. Each time the slump value is measured and it is between 80– 105mm. Beam specimens are demolded after 24 hours of casting.

2.1. MATERIALS INVESTIGATION

The material properties are determined according to ASTM standard method and they are summarized below;

Table 1. Properties of Materials

Materials	Properties	Unit	Value
Binder (OPC)	Specific Gravity		3.15
Fine Aggregate	Specific Gravity (SSD)		2.50
	Absorption	%	3.36
	Unit Weight	Kg/m³	1629
	FM		2.58
Coarse Aggregate	Specific gravity (SSD)		2.82
	Void	%	28.90
	Absorption	%	2.02
	Unit Weight	Kg/m³	1619
	FM		4.68
Reinforcement	Yield Strength	MPa	450
	Ultimate Strength	MPa	520
Concrete	Compressive strength	MPa	19.1

To prepare the normal strength concrete according to the ACI standard a suitable mix design ratio is used. The expected compressive strength is 3000 psi after 28 days. Cement: Sand: Coarse Aggregate (1: 1.5: 3), Water: Cement is 0.48, Nominal maximum size of Coarse aggregate 12.80 mm.

a). Mixing procedure b). Slump test

Figure 2. Preparation of Concrete

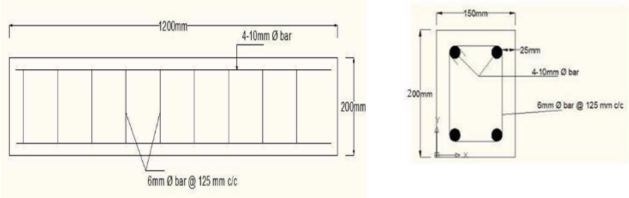

a). Longitudinal section b). Cross-section

Figure 3. Sectional view of specimen

The flexural strength of plain concrete is almost wholly dependent upon the tensile strength. Experiments show, however, that the modulus of rupture is considerably greater than the strength in tension. Flexural strength is of importance in the design of concrete pavements. 3rd point loading system for the test of flexural strength of this specimen.

a). Casting b). lab setup

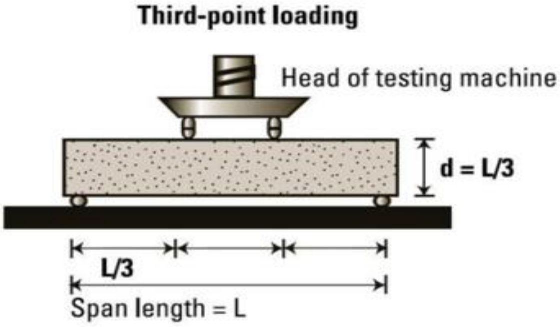

c). 3rd point loading system

Figure 4. Beam casting and setup for test

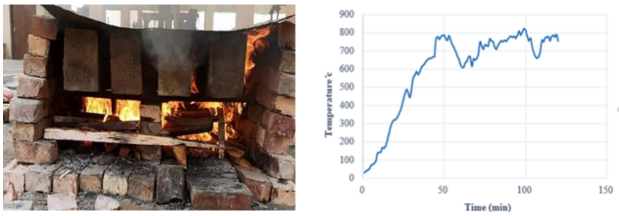

a). Damage by fire b). Temperature and time

Figure 5. Process of beam damage

For heating the beams, a chamber is made by using bricks, CI sheets and steel reinforcements. The temperature is measured by thermocouple and digital meter. The highest temperature during fire of building is 805 ⁰c and temperature varied at a range of 700-800 ⁰c for two hours and then cooled to room temperature. When the beams are cooled down, there are some cracks and spalling of concrete seen on beams.

As concrete is weak in tension, cracks and spalling formed in the tension zone of the beams under fire, the concrete in the tension zone become ineffective. The depth of the cracks is show in beam within 1 inch. Hence, soffit of the beams (tension zone clear cover) is chiseled, cleared of loose debris and cleaned with wire brush.

Figure 6. Chiseling of beam

After fire damaged, samples are strengthened with a Ferro cement and wire mesh (single layer and double layer). A single layer square shaped steel wire mesh having wire spacing of 10 mm and thickness of 0.6 mm is used.

Figure 7. External strengthening of beam

A rich mortar ratio of cement/sand 1:2 and w/c ratio 0.4 is selected. The sand is used which the sample passing by No.16 sieve is 80%. Hand plastering is used for the period of the strengthening process. Mortar is pressed through the pores of wire mesh. Plastering is properly done to confirm an even and smooth surface. The Ferro cement strengthened samples are additional cured for 7 days. It necessitates a huge amount of water and proper supervision for the period of curing process, due to rich mortar and low water-cement ratio.

3. RESULTS AND DISCUSSION

The ultimate load resounding capabilities of both control and strengthened beams are determined by third point loading method. The lateral deformations at mid height and of the specimens are also recorded with an incremental load. The load vs deflection diagram for all types of specimens has been established through dial gauge readings. The effect of strengthening has been evaluated by comparing the results with control specimens.

Table 2. Load capacity of several specimens

Name of Specimen	Ultimate Load (kN)	Improvement over fire damage Specimen (%)	Decline over control Specimen (%)
Control beam	114	-	-
Fire damaged specimen	61	-	46
Single layer Ferro cement strengthened	89	46	22
Double layer Ferro cement strengthened	105	72	08

The flexural strength characterizes the maximum stress practiced inside the material at its moment of rupture. Most of the specimens fail due to flexure failure. Flexure cracks are developed at the mid-section, after that flexure shear cracks as well as web shear crack are developed before the beam is failed.

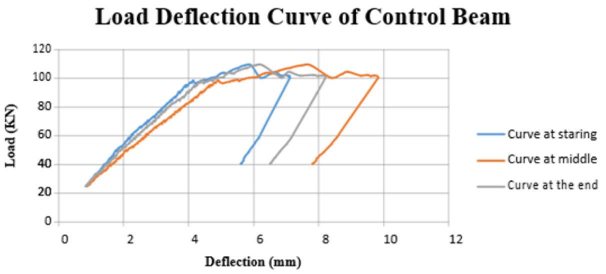

a). Control beam

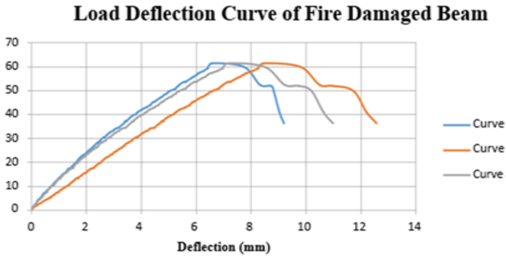

b). Fire damaged beam

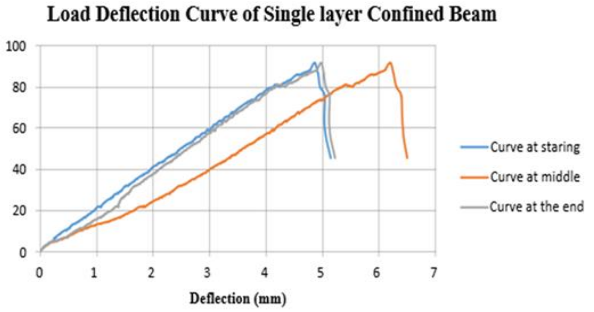

c). Single layer Ferro cement strengthened beam

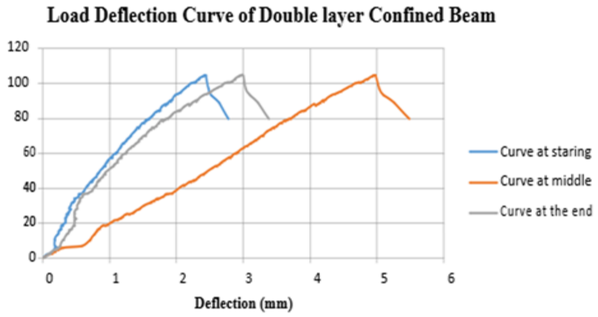

d). Double layer Ferro cement strengthened beam

Figure 8. Load deflection curve of specimens

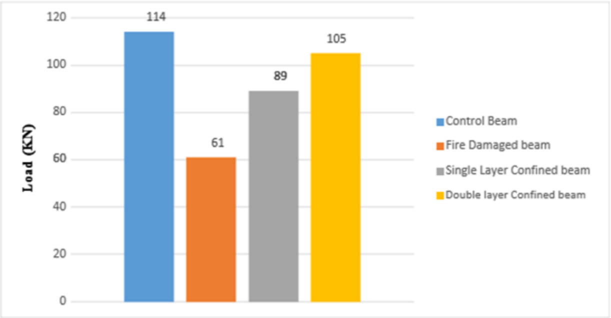

Figure 9. Load capacity of several specimens

Due to the strengthening effect, the deformations first initiated in the Ferro cement layers. After the failure of the layer, the core failure takes place. In case of single- and double-layer Ferro cement strengthened concrete beams, the crack is initiated simultaneously from the base and top of the beam. After initiation, with the increase of load the cracks are propagated. The propagation of cracks is slow due to the presence of thickly populated wire mesh. Both cases showed great improvement in ultimate load carrying capacity and slow crack formation over the fire damaged specimens.

a). Fire damaged beam

b). single layer Ferro cement strengthened beam

Figure 10. Cracking and failure pattern of specimens

4. CONCLUSION

The behavior of RC beams is subjected to heating and cooling and the repair of such damaged beams by wrapping with Ferro cement and wire mesh at different layer. The level of heating exposure considerably reduced the residual concrete compressive strength by about 46 %. The ultimate load carrying capacity for using single layer Ferro cement with wire mesh strengthening, double layer Ferro cement with wire mesh strengthening show an improvement of 46% and 72% respectively over the fire damaged specimens. The Flexural strength of RC beams increases directly proportion to the number of Ferro cement with wire mesh layers is used. The Ferro cement with wire mesh confinement with two layers show greater improvement than the confinement technique with one layer, both in load carrying capacity and slow crack formation.

5. RECOMMENDATIONS

Based on the findings of this research, it is considered that further research should be undertaken to the behavior of strengthened concrete beams under uniformly distributed loading. The following suggestions ought to be taken into consideration both point and uniformly distributed loading.

- The shrinkage and creep of concrete can be investigated when exposed to fire;
- Bond behavior and thermal properties of concrete when exposed to fire may be checked;
- The effect of mix proportions, types of coarse aggregates heating rate and burning time can be overlooked.

ACKNOWLEDGEMENT

The author wants to express thankfulness to Almighty ALLAH at first that the research is completed. The author would like to express his greatest gratitude to his beloved parents and sister for their unconditional love, caring and passions. The author is also grateful to all the laboratory technicians, Department of Civil Engineering for their co-operation to this research.

Author contributions

Al Amin: Writing-Original draft preparation **Shorup Chowdhury Tamal:** Conceptualization, Methodology **A. K. M. Fayzul Bari:** Investigation, Visualization **Milan Mazumder:** Data curation **Md. Ariful Hasan**: Writing-Reviewing and Editing

Conflicts of interest

The authors declare no conflicts of interest.

REFERENCES

Amin A, Pial M A, Ahmad M & Ahamed M J (2021). Comparison in Strengthening of RCC Concrete Column Using Ferrocement and Polypropylene Fiber Rope. Eurasian Journal of Science Engineering and Technology, 2(1), 12-19.

Anggawidjaja D, Ueda T, Dai J & Nakai H (2006). Deformation capacity of RC piers by new fiber-reinforced polymer with large fracture strain. Cem. Concr. Compos. 28(10), 914–927.

Choi J H (2008). Seismic retrofit of reinforced concrete circular beams using stainless steel wire mesh composite. Can. J. Civ. Eng., 35(2), 140–147.

Colombo M & Felicity R (2007). New NDT techniques for the assessment of fire damaged concrete structures. Fire Safety Journal, 42 (6–7), 461–472.

Dai J-G, Bai Y-L & Teng J G (2011). Behavior and modeling of concrete confined with FRP composites of large deformability. Journal of Composites for Construction, 15(6), 963-973.

Rafeeqi S F A, Lodi S H & Wadalawala Z R (2005). Behaviour of reinforced concrete beams strengthened in shear. Journal of Ferro cement, 35(1), 479.

Tepfers R & De Lorenzis L (2003). Bond of FRP reinforcement in concrete-a challenge. Mechanics of composite materials, 39(4), 315-328.

Zahid M M, Bakar B A, Nazri F M, Ahmad M M & Muhamad K (2018, March). Review of repair materials for fire-damaged reinforced concrete structures. In IOP Conference Series: Materials Science and Engineering (Vol. 318, No. 1, p. 012023). IOP Publishing.

Turkish Journal of Engineering
https://dergipark.org.tr/en/pub/tuje
e-ISSN 2587-1366

Clarifying the impact of climatic parameters on vegetation in Moulvibazar district

Mst. Mahbuba Khatun*[1], Debajani Chakraborty [1], Ifterkharul Alam [2]

[1]*Sylhet Agricultural University, Faculty of Agricultural Engineering and Technology, Department of Irrigation and Water Management, Sylhet, Bangladesh*
[2]*University of International Business & Economics, Faculty of Public Administration, Department of Customs Administration, Beijing, China*

Keywords
GLAM NDVI
MAKESENS
Lag effect
Cross-correlation
Trend

ABSTRACT

In this research, the temporal trends of vegetation from 2000 to 2019 as well as meteorological variables contribution to vegetation change were investigated using the GLAM NDVI, rainfall and temperature data. The MAKESENS revealed that the vegetation growth rate was slow, particularly on a yearly time scale. On the other hand, the rainfall and temperature had a major impact on vegetation growth on a monthly-time scale with a time lag. The lagged effect of rainfall and temperature on vegetation was shown to be a promotion (based on cross-correlation analysis). There was high value of r (0.804) between vegetation and rainfall for a certain lag period, which was significant ($P \leq 0.05$) as per the cross-correlation. Rainfall had a 4-month lag effect on vegetation development, while temperature had a 5 (r = 0.74), − 2 (r = 0.84), − 3 (r = 0.68) month lag effect on vegetation growth. This study's findings revealed changes in vegetation and highlighted the importance of rainfall and temperature in regulating vegetation dynamics. Finally, this study recommended that the effect of more climatic variables on vegetation should be investigated in the context of human activities to better conserve the environment.

1. INTRODUCTION

Vegetation is demonstrated by the Normalized Differential Vegetation Index (NDVI) (Tucker 1979) and is also a common tool for depicting biodiversity transition (Nemani et al. 2003). The evolution of satellite sensor technologies has resulted in obtaining these changes more efficiently and effectively (Shen et al. 2016). To a large extent, these technologies have been used in identifying the location of surface vegetation (Chu et al. 2019) over a long period with high spatial and temporal resolution (Rasmus and Simon 2012). Eastman et al. (2013) used NDVI to assess the validity of remote sensing data, especially for evaluating green vegetation and understanding the moisture content of the vegetation in a given region (Delbart et al. 2005; Jackson et al. 2004).

NDVI is also used in drought and ecosystem monitoring (Gu et al. 2008; Gu et al. 2007). As a result, several studies have shown that NDVI is capable of studying vegetation changes at different scales. NDVI was employed to investigate the spatiotemporal distribution of vegetation (Liu and Lei 2015, Zhang et al. 2013). Furthermore, Shilong et al. 2011 investigated vegetation temporal trends in Eurasia's temperate and boreal regions using the NDVI.

Generally, vegetation connects water, soil, environment, and other natural substances (Nemani et al. 2003). At various scales, the NDVI–climate relationship has been well described in many studies. In regions with abundant water supplies, global warming promotes vegetation growth, while in areas with limited water resources, vegetation growth is seriously hampered (Feng et al. 2016). Rainfall and temperature, which have major effects on vegetation growth and distribution, are the two most important factors affecting vegetation change (Pei et al. 2019; Xu et al. 2015). Nowadays, there are noticeable changes in global climate and environment (Na et al. 2018). The climatic and anthropogenic influences on variations in vegetation patterns and functions are major concerns in ecosystem research (Li et al. 2019). The temperature increased plant activity in the Northern Hemisphere (Mao et al. 2013; Piao et al. 2015), while rainfall had a significant

---

* **Corresponding Author**

*(mahbubakhatun212@gmail.com) ORCID ID 0000-0002-2177-6161
(debajanisharmi@gmail.com) ORCID ID 0000-0001-9695-4340
(CMW202054005@uibe.edu.cn) ORCID ID 0000-0002-3494-8081

Cite this article

Khatun M M, Chakraborty D & Alam I (2022). Clarifying the impact of climatic parameters on vegetation in Moulvibazar district. Turkish Journal of Engineering, 6(3), 211-222

Research Article / DOI: 10.31127/tuje.930293

Received: 30/04/2021; Accepted: 06/06/2021

impact on NDVI in arid and semi-arid areas (Camberlin et al. 2007; Piao et al. 2011). Also, the early greening of the meadow steppe vegetation is aided by spring climate warming, whereas, the issue of weather change was mitigated by the water shortage of traditional steppe and desert steppe vegetation (Zhao et al. 2015). Rainfall, on the other hand, has a major impact on the variation of vegetation at the inter-annual time scale, whilst, at the monthly time level, the vegetation development is affected by both temperature and rainfall (Liu and Wang 2012).

As a result, the primary concern of researchers is the relation between vegetation and climate due to its clear indicative effect on the ecological system (Eastman et al. 2013). For example, lag period and variation of vegetation due to climatic parameters was investigated by Wu et al 2015. The cross-correlation method of comparing a data set at consecutive lags is applied to assess the time lag effect (Davis 2002). Time series measurements must be taken at corresponding times in a cross-correlation study, i.e., two variables must be calculated at the same time (Posavec et al. 2017). A time series is generated when a collection of observations is organized in a systematic order based on their dates of occurrence. A trend, on the other hand, is a consistent change over time in the time series characteristics (Patra 2008). Detecting the existence of trends can be done using a variety of methods. Sun et al. 2021, for instance, investigated the seasonal changes in the normalized difference vegetation index (NDVI) and then evaluated the spatiotemporal pattern of vegetation using Sen's tendency estimation as well as the Mann–Kendall significance test. Multiple regression, Sen's, and Mann–Kendal methods were used to quantify the effects of rainfall, temperature, and human activities on vegetation (Li et al. 2019). A computer software model named MAKESENS is used for trend analysis which is relying on the nonparametric Mann-Kendall test for trend and nonparametric Sen's method for trend magnitude (Salmi et al. 2002).

Around 63 percent of Bangladesh's tea is produced in Moulvibazar (Islam and Al-Amin 2019). Since vegetation estimation and site characterization are still in their infancy in Bangladesh, the study of vegetation in context of rainfall and temperature has yet to be investigated in this rapidly growing town of Moulvibazar. Therefore, understanding vegetation evolution and change characteristics as a result of climate change necessitates a detailed study of the vegetation-rainfall, temperature relationship.

The study purposes were to analyze the temporal variability and trend of NDVI and other meteorological parameters in the Moulvibazar district. Apart from this, another one is to investigate the relationship between NDVI and climatic factors. This research in particular, investigates the impact of climatic variables on vegetation variation and the subsequent vegetation lag caused by climatic factors. The study clarified the relationship between NDVI and climatic variables, evaluated the correlation at different time scales, and estimated the timing of NDVI response to climatic variables, all of which are important for future studies.

2. MATERIALS and METHOD

2.1. Study Site Description

Moulvibazar district is located at Sylhet division in Bangladesh's north-eastern region (Kabir et al. 2014). The climate in Moulvibazar is humid subtropical. Monsoons, high temperatures, high humidity, and heavy rainfall characterize the climate of Moulvibazar. The hot season begins in early April and lasts until July. Moulvibazar has a mean annual temperature of 24.7 °C. A total of 2,805 mm of precipitation occurs each year (Wikipedia 2020). This town (Fig. 1) has a landscape with a Holocene flood plain, a low raised terrace, and sporadic hillocks from the geomorphological context (Rahman et al. 2018).

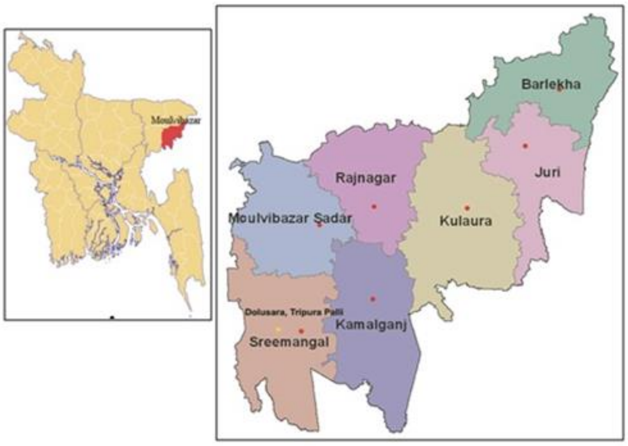

Figure 1. Moulvibazar district

The research used the Global Agriculture Monitoring (GLAM) Terra MODIS 8-day NDVI data in CSV format (https://glam1.gsfc.nasa.gov/) from 2000 to 2019 to investigate the vegetation's temporal distribution. For any given year, this website provides MODIS NDVI images and graphs. The annual NDVI trend can also be compared to the long-term average (NDVI Anomalies) on this website (ARSET Advanced NDVI Webinar Series 2020). NASA Goddard Space Flight Center's GIMMS (Global Inventory Monitoring and Modeling Studies) division, USDA FAS (US Department of Agriculture Foreign Agricultural Service), the South Dakota State University Geographic Information Science Center of Excellence and the University of Maryland-Department of Geography initiated a collaborative research project named GLAM (Becker-Reshef et al. 2010). The project, which started in 2002, is co-financed by USDA-FAS and NASA. It provides timely, easily accessible, remotely sensed data which is scientifically validated for crop condition monitoring and production assessment (USDA FAS 2020). The meteorological data (precipitation and temperature) from 2000 to 2019 within the study area were collected from the Power Data Access Viewer-NASA POWER (https://power.larc.nasa.gov/data-access-viewer/) to examine their impact on vegetation.

2.2. Methods

Initially, the PNG (Portable Network Graphics) formation, which was downloaded from the website https://glam1.gsfc.nasa.gov/, was used to evaluate the oversimplified view of NDVI in the Moulvibazar region. The annual trend of climatic factors and NDVI was then determined using the MAKESENS software. Furthermore, the monthly trend of NDVI was examined in this regard. The correlation was also examined to analyze the influence of climatic variables on vegetation, and the lag period was determined using the cross-correlation process. The website https://exceluser.com/1069/ provided the ready-to-use cross-correlation excel spreadsheet.

2.2.1. The oversimplified view of NDVI in Moulvibazar

For Moulvibazar, an image of NDVI with NDVI anomaly was taken from the GLAM website (https://glam1.gsfc.nasa.gov/) (Fig. 2). An NDVI anomaly is the difference between the average NDVI for a given month in a given year and the average NDVI for the same month over a fixed number of years. This method can be used to compare the health of vegetation in a given month and year relative to what is considered natural, which can be a good indicator of drought or deteriorating vegetation health (ARSET Advanced NDVI Webinar Series 2020).

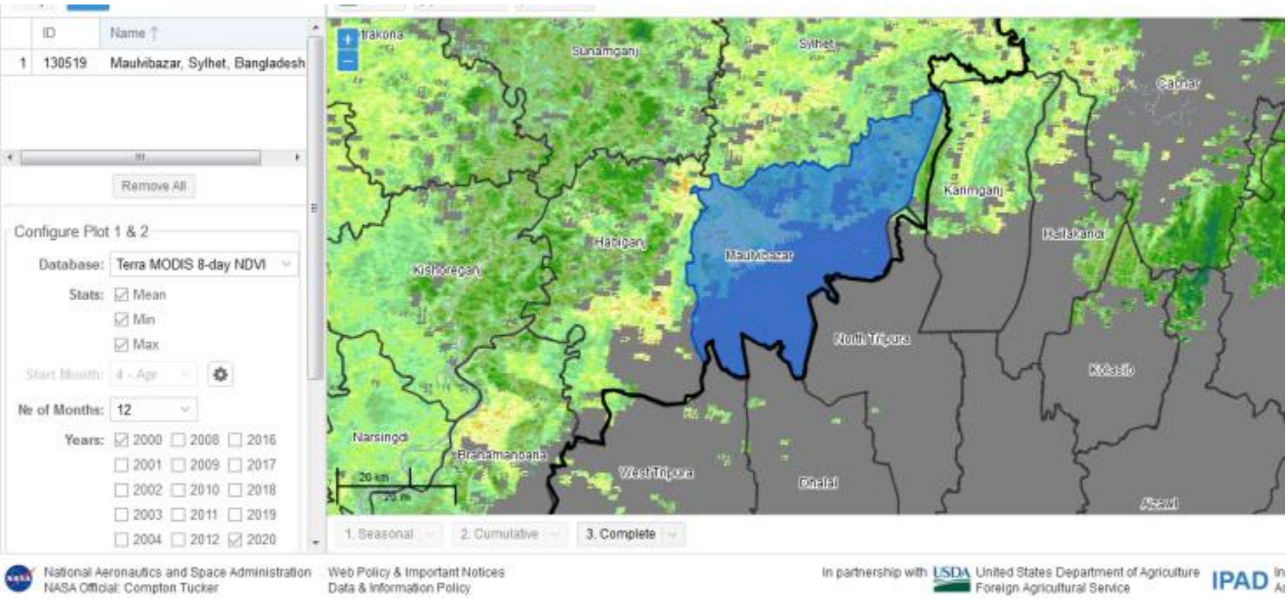

	ID	Name
1	130519	Maulvibazar, Sylhet, Bangladesh

Configure Plot 1 & 2

Database: Terra MODIS 8-day NDVI

Stats: ☑ Mean ☑ Min ☑ Max

Start Month: 4 - Apr

№ of Months: 12

Years: ☑ 2000 ☐ 2001 ☐ 2002 ☐ 2003 ☐ 2004 ☐ 2008 ☐ 2009 ☐ 2010 ☐ 2011 ☐ 2012 ☐ 2016 ☐ 2017 ☐ 2018 ☐ 2019 ☑ 2020

Figure 2. Selection of Moulvibazar district

2.2.2. Trend analysis

For analyzing the sloping pattern of time-series, Sen et al. proposed the Sen's estimation process (Li et al. 2019; Meng et al. 2020). It is a computational method that has the advantage of not being influenced by a lack of data. The MAKESENS method was then employed to calculate the NDVI time series' sloping pattern. The following is the formula:

$$f(t) = Qt + B \qquad (1)$$

The *f(t)* was a monotonically increasing or decreasing time function, the constant was *B* and the slope was *Q*. To obtain the slope estimate *Q* in Eq. (ii), all data value pairs' slopes were first estimated (Li et al. 2019; Meng et al. 2020; Salmi et al. 2002):

$$Q_i = \frac{x_j - x_k}{j - k} \qquad (2)$$

Here *j* and *k* are the years, and x_j and x_k are the annual values of these years where $j > k$. If the time series had n values x_j the slope Q_i is estimated by $N = n\ (n-1)/2$. Sen's slope estimator was the median of these *N* values of Q_i (Salmi et al. 2002).

Sen's tendency estimation approach does not provide statistical significance tests for the trend, so the MAKESENS method was used to assess the trend. Since it is nonparametric statistical test, this technique is widely used to detect a monotonic pattern in climate. The MAKESENS method (Li et al.,2019; Meng et al. 2020; Salmi et al. 2002) was as follows:

$$Z = \begin{cases} \left(\frac{S-1}{\sqrt{VAR(S)}}\right) & if\ S > 0 \\ 0 & if\ S = 0 \\ \left(\frac{S+1}{\sqrt{VAR(S)}}\right) & if\ S < 0 \end{cases} \qquad (3)$$

$$S = \sum_{k=1}^{n-1} \sum_{j=k+1}^{n} sgn(x_j - x_k) \qquad (4)$$

$$sgn(x_j - x_k) = \begin{cases} 1 & if\ x_j - x_k > 0 \\ 0 & if\ x_j - x_k = 0 \\ -1 & if\ x_j - x_k < 0 \end{cases} \tag{5}$$

$$VAR(S) = \frac{1}{18}\left[n(n-1)(2n+5) - \sum_{p=1}^{q} t_p(t_p-1)(2t_p+5)\right] \tag{6}$$

Where S denoted the test statistic and VAR(S) denoted variance of S. q was the number of tied groups and in the pth group, tp was the number of data values. For time series with less than ten data points, the S test was used, and for time series with ten or more data points, the standard approximation (Z) was used.

The number of annual values in the data series under investigation was denoted by the letter n. For four different significance levels in MAKESENS, the two-tailed test was used α: 0.1, 0.05, 0.01, and 0.001. An upward (downward) trend is indicated by a positive (negative) Z value (Salmi et al. 2002).

2.2.3. Relationship and Lag Time Analysis

The lag relationship between hydrothermal factors and vegetation is more pronounced. Therefore, studying the NDVI–climate relationship on a monthly time scale may be more realistic. Climate change affects vegetation in a variety of ways. Vegetation does not always react to climate change immediately, indicating that there is a time lag in vegetation due to climate change. The NDVI–climate relationship was investigated on two-time scales in this study: (i) monthly average NDVI and climatic variables from 2000 to 2019, and (ii) annually average NDVI and climatic variables from 2000 to 2019. In the first case, the NDVI and climate factor mean monthly sequences (January to December) from 2000 to 2019 were used as two sets of variables, and the value of correlation coefficients between them was estimated. On the other hand, the yearly average series of NDVI and climatic factors from 2000-2019 were taken for the second case. The value of correlation coefficients between NDVI and climatic factors was determined in the same way as in the first case. The following is the related formula (Wang et al. 2020; Li et al. 2018):

$$R_{xy}\ (r) = \frac{\sum_{i=1}^{n}[(x_i-\bar{x})(y_i-\bar{y})]}{\sqrt{\sum_{i=1}^{n}[(x_i-\bar{x})^2(y_i-\bar{y})^2]}} \tag{7}$$

where R_{xy} is the Pearson correlation coefficients between variable *x* and variable *y*, with a value between −1 and 1, *n* is the sample size, x_i is the value of NDVI in the *i*th month, and y_i is the mean monthly climate factors in the *i*th month, where $\bar{x}$ and $\bar{y}$ are the means of the two variables, respectively. In addition, the ANOVA findings were used to test the significance of the correlation coefficients.

The response time is known as the lag time that corresponds to the maximum of the cross-correlation function (Cai and Ofterdinger 2016). In this analysis, the mean response time of the NDVI in the study region to climatic events was calculated using a cross-correlation function between climatic factors (rainfall, temperature) and NDVI time-series. In order to estimate lag time, a specially developed cross-correlation Excel spreadsheet program was used. The correlation (r) was estimated by the value of NDVI and climatic parameters. The calculation was done by the value of current and previous 1–5-month climatic parameters with the value of NDVI. Furthermore, r was also calculated by the current as well as the previous 1–5 months' NDVI values with climatic factors.

3. RESULTS

3.1. General View of NDVI

Before conducting in-depth studies on NDVI in Moulvibazar, a general view of NDVI would assist in vegetation assessment. Throughout the study period, the range of NDVI values within the study area was shown in Fig. 3 and 4. The NDVI values ranged from - 1 to 0.90 across the entire study region. Besides that, the graphical representation (Fig. 3) depicted a comparison of the NDVI mean from 2001 to 2018 with the 8-day NDVI values. The graph beneath it (Fig. 4) depicted the fluctuation of negative and positive NDVI anomalies over time. Over Moulvibazar, the highest positive anomaly pattern was observed in 2013 and 2017, while the highest negative anomaly pattern was discovered at the end of 2010. In comparison to the positive anomaly pattern, the study zone had more negative anomalies.

3.2. Annual Pattern of Climatic Factors and NDVI

In Fig. 5, the trend of mean annual climatic factors (rainfall, temperature) and NDVI in the Moulvibazar district (as determined by MAKESENS) was illustrated. The trends of NDVI and rainfall (except temperature) were statistically significant at different levels (Table 1). The trend's alternative hypothesis was rejected in temperature, as shown by the blank cell of significance. The NDVI and rainfall both showed a significant upward trend based on positive Z values, with an increased rate of 0.003/year and 0.149 mm/year, respectively (Table 1). The NDVI trend was significant at a level of 0.05 for the entire observation period, while the rainfall time series trend was significant at a level of 0.1. In the case of temperature, however, the rate was zero.

3.3. Monthly Pattern of NDVI

The trends (by MAKESENS) of mean monthly NDVI were shown in Fig. 6. The trends were statistically significant at different levels excluding in months January, June, September, and October (Table 2). The null hypothesis of the trend was accepted in these months, as shown by the significance blank cell. Depending on the positive Z values, the NDVI displayed a noticeable upward trend, which varied between 0.002 and 0.007 per month.

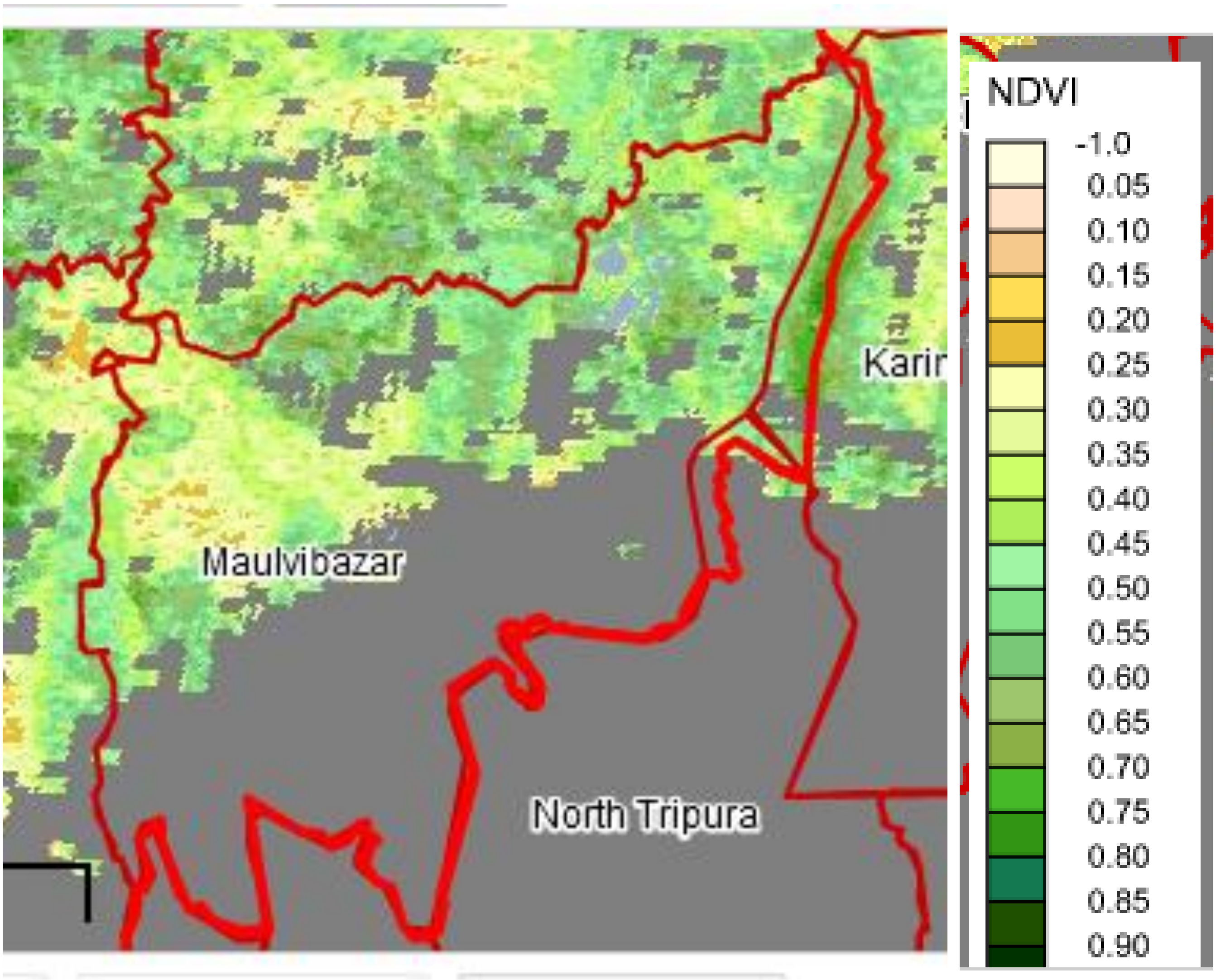

Figure 3. NDVI value in Moulvibazar

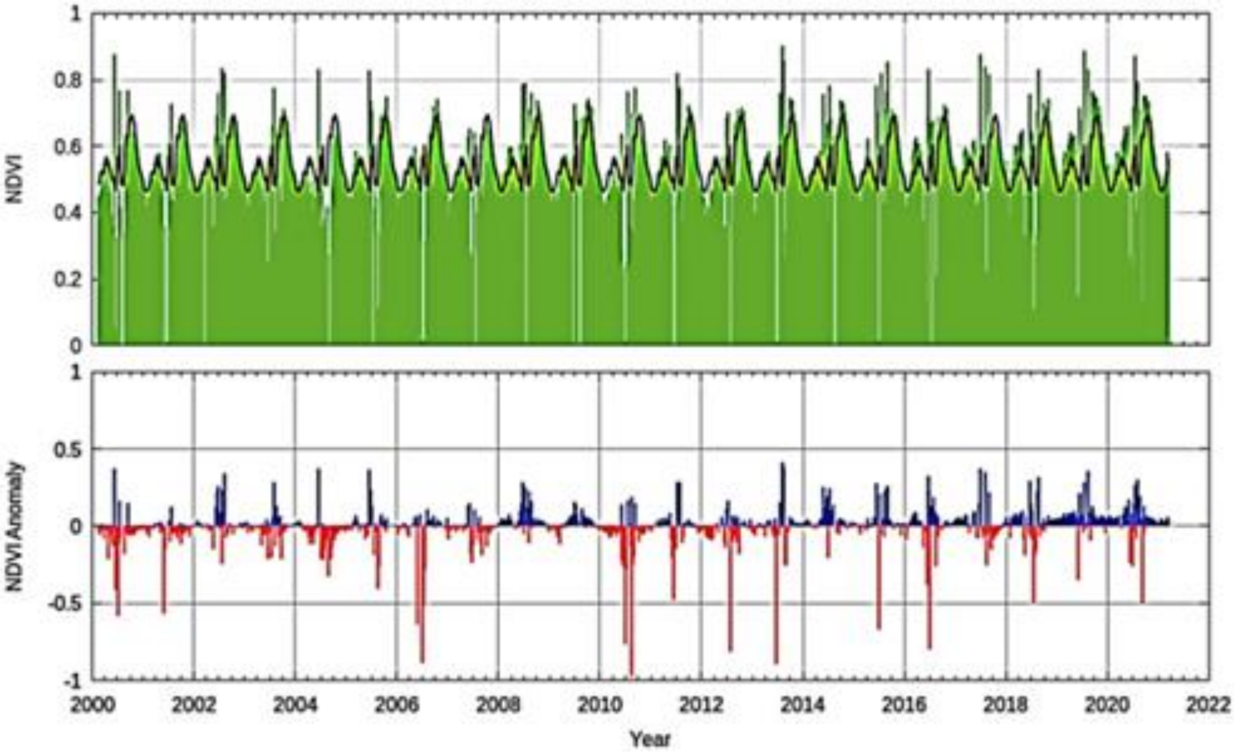

Figure 4. NDVI and NDVI anomaly in Moulvibazar

Table 1. Annual trend of climatic factors and NDVI

Events	First Period	Last Period	Test Z	Rate of Change per Year, Q	Constant, B	Significance of Trend, **α**
NDVI	2000	2019	2.37	0.003	0.50	0.05
Rainfall (mm)	2000	2019	1.78	0.149	5.18	0.1
Temperature (°C)	2000	2019	0.00	0.000	24.40	

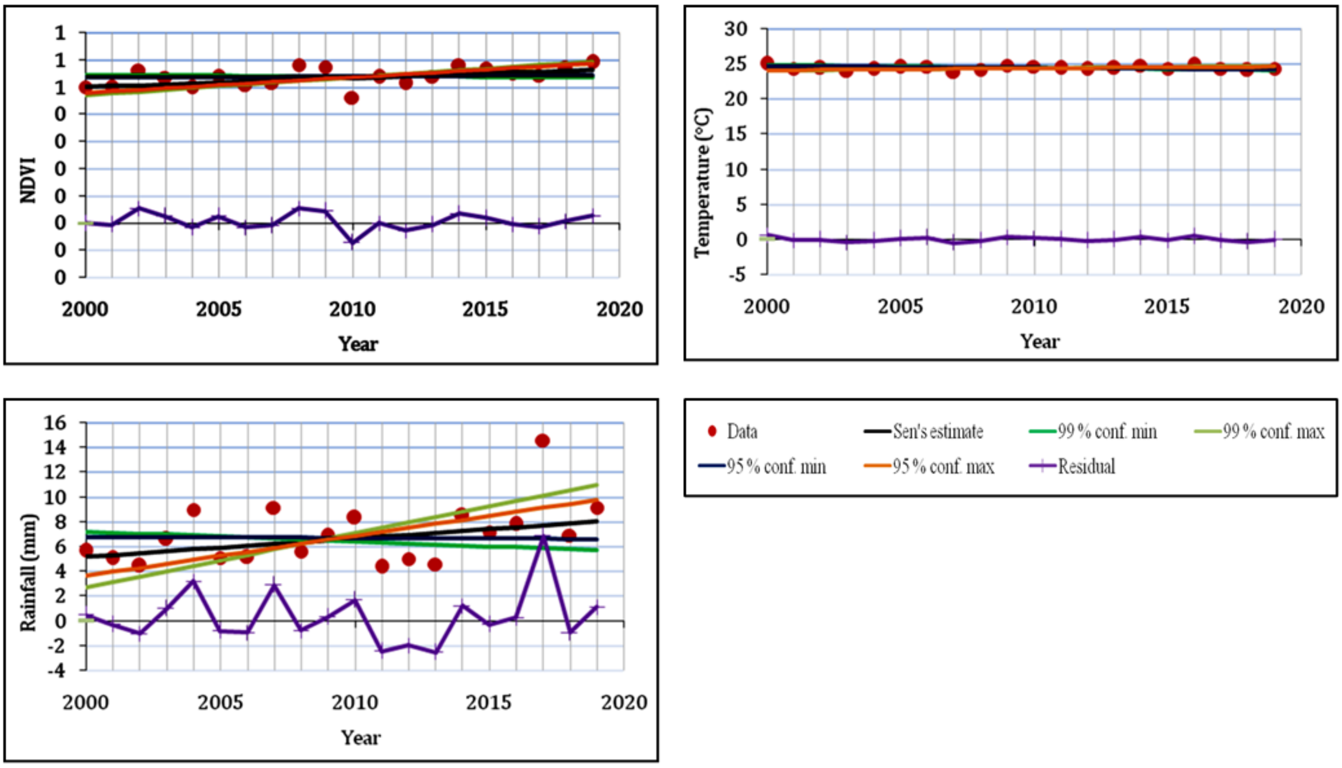

Figure 5. Trends of mean annual NDVI and climatic factors

Table 2. Monthly trend of climatic factors and NDVI

Month	First Period	Last Period	Test Z	Rate of Change per Year, Q	Constant, B	Significance of Trend, **α**
Jan	2000	2019	0.91	0.001	0.46	
Feb	2000	2019	2.04	0.003	0.47	0.05
Mar	2000	2019	1.91	0.003	0.50	0.1
Apr	2000	2019	2.11	0.003	0.53	0.05
May	2000	2019	2.50	0.005	0.48	0.05
Jun	2000	2019	0.55	0.004	0.46	
Jul	2000	2019	-0.49	-0.003	0.50	
Aug	2000	2019	1.98	0.007	0.47	0.05
Sep	2000	2019	1.07	0.002	0.62	
Oct	2000	2019	1.46	0.002	0.67	
Nov	2000	2019	2.08	0.003	0.58	0.05
Dec	2000	2019	2.70	0.002	0.50	0.01

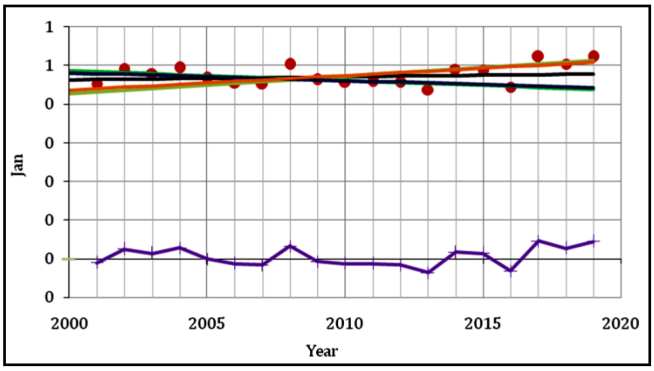
1
1
0
0
0
0
0
0
Jan
2000
2005
2010
2015
2020
Year

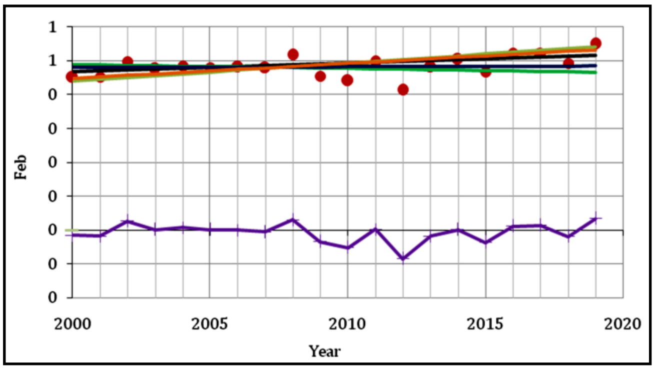
1
1
0
0
0
0
0
0
0
Feb
2000
2005
2010
2015
2020
Year

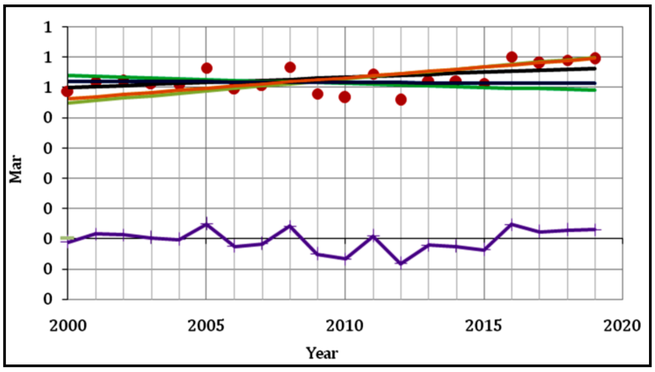
1
1
1
0
0
0
0
0
0
0
Mar
2000
2005
2010
2015
2020
Year

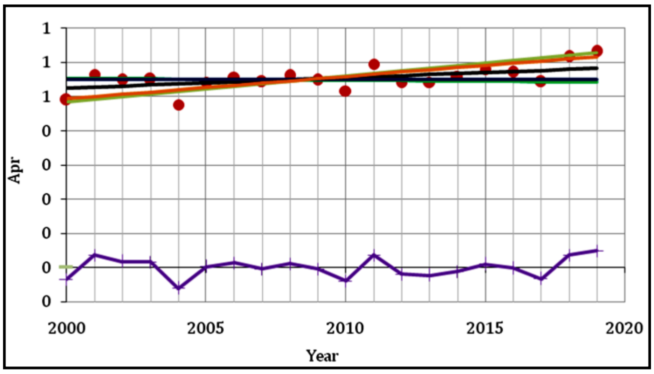
1
1
1
0
0
0
0
0
0
Apr
2000
2005
2010
2015
2020
Year

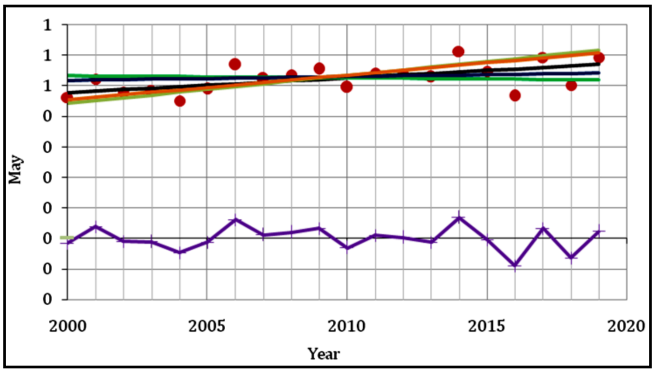
1
1
1
0
0
0
0
0
0
0
May
2000
2005
2010
2015
2020
Year

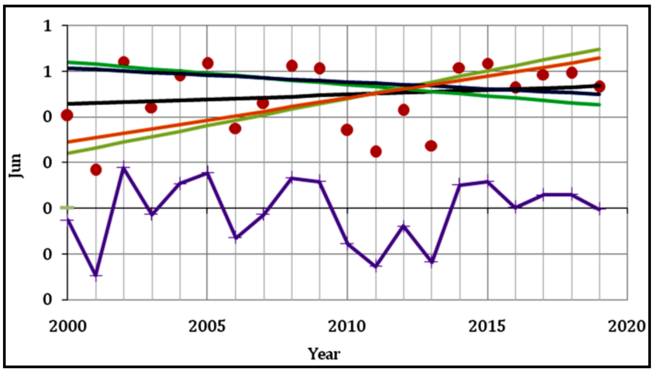
1
1
0
0
0
0
0
Jun
2000
2005
2010
2015
2020
Year

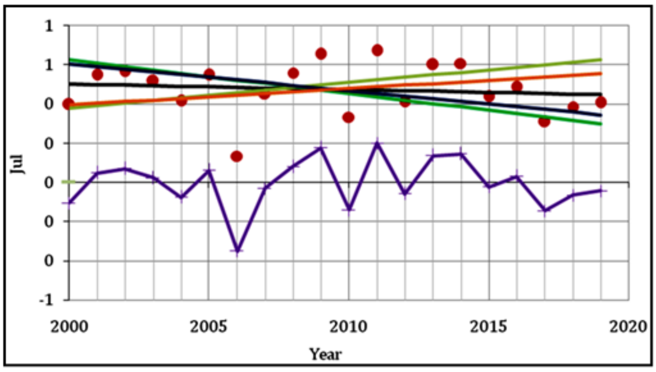
1
1
0
0
0
0
0
-1
Jul
2000
2005
2010
2015
2020
Year

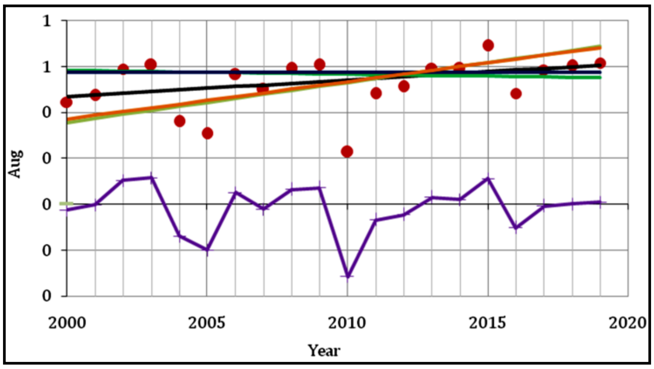
1
1
0
0
0
0
0
Aug
2000
2005
2010
2015
2020
Year

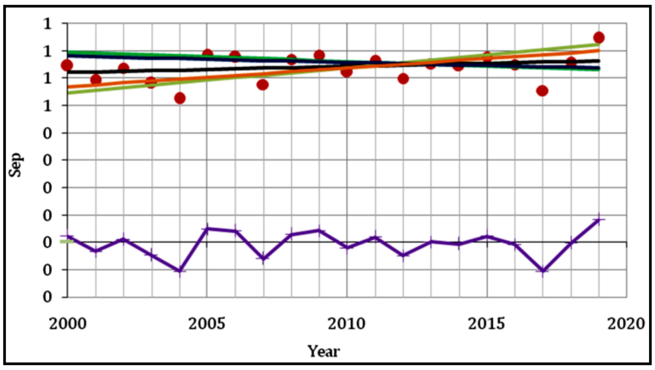
1
1
1
1
0
0
0
0
0
0
0
Sep
2000
2005
2010
2015
2020
Year

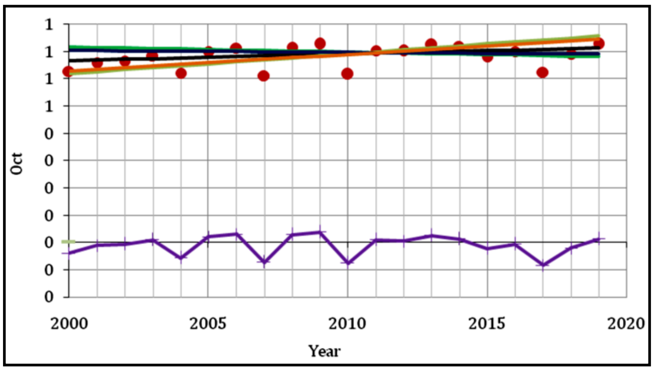
1
1
1
1
0
0
0
0
0
0
0
Oct
2000
2005
2010
2015
2020
Year

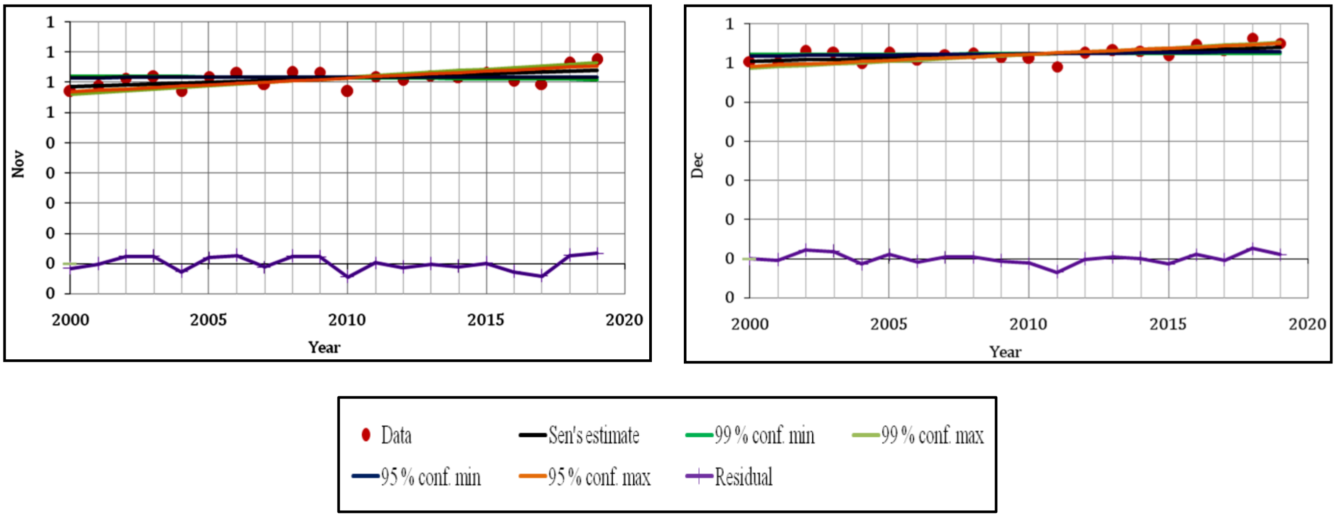

Figure 6. Trends of mean monthly NDVI time series

3.4. Relationships between Climatic Variables and Vegetation

Rainfall and temperature were used in this analysis to demonstrate their impact on NDVI. Rainfall showed an irregular gradient in different years (Fig. 7 (right)), while the distribution of rainfall is highly unequal in month-wise (Fig. 7 (left)) variance. The areas with high rainfall values were observed in 2017 (14.57 mm) (Fig. 7(right)) and in June (15.45 mm) (Fig. 7(left)). On the other side, the low values were distributed mainly in 2011 (4.39 mm) (Fig. 7(right)) and in January (0.16 mm) (Fig. 7(left)). The mean annual rainfall was 6.96 mm (Fig. 7(right)) over the study area and it increased from April to October (Fig. 7(left)) over the study period. The lowest rainfall was observed from November to March (Fig. 7(left)). On the other hand, the temperature also varied (Fig. 8) with the lowest values mainly in January (17.22 °C) and in 2007 (23.92 °C), and with the highest values mainly in July (27.78 °C) and in 2000 (25.07 °C). The areas with high temperature values were noticed from March to October, whereas, low temperature values were observed from November to February (Fig. 8 (left)). From 2000 to 2019, the mean NDVI value in the study region showed distinct characteristics (Fig. 7 and 8). The NDVI fluctuated in a small range maintaining a stability in the region with the lowest value of 0.47 (July) and 0.46 (2010), and the highest value of 0.68 (October) and 0.59 (2019). Almost similar results in the case of annual NDVI with the highest (2017) and lowest (end of 2010) values were also found from section 3.1 (Fig. 4). Every year, the lower values of NDVI were appeared between January and February. On the other side, the higher values were appeared from July to October indicating NDVI changed in a predictable pattern (Fig. 7 (left) and 8 (left)). From the analysis, the highest NDVI was noticed in October while the highest rainfall was found in June. So, the monthly NDVI value was increased corresponding to rainfall with about 4 months lag. Similarly, the monthly NDVI value was increased corresponding to temperature with about 6 months lag. However, the annual relationship was found uneven in both cases.

The correlations R^2 (r) between the climatic parameters and NDVI were evaluated at two-time scales to determine the effects of each on vegetation: (i) one is monthly (Fig. 9(left), 10(left)), and (ii) another is annually (Fig. 9(right), 10(right)). As shown in Fig. 9 and 10, an insignificant correlation was observed with positive value, indicating that both rainfall and temperature had less impact on vegetation over the study area. According to the above results, NDVI with a certain lag time showed frequent changes as climatic factors changed on a regular basis.

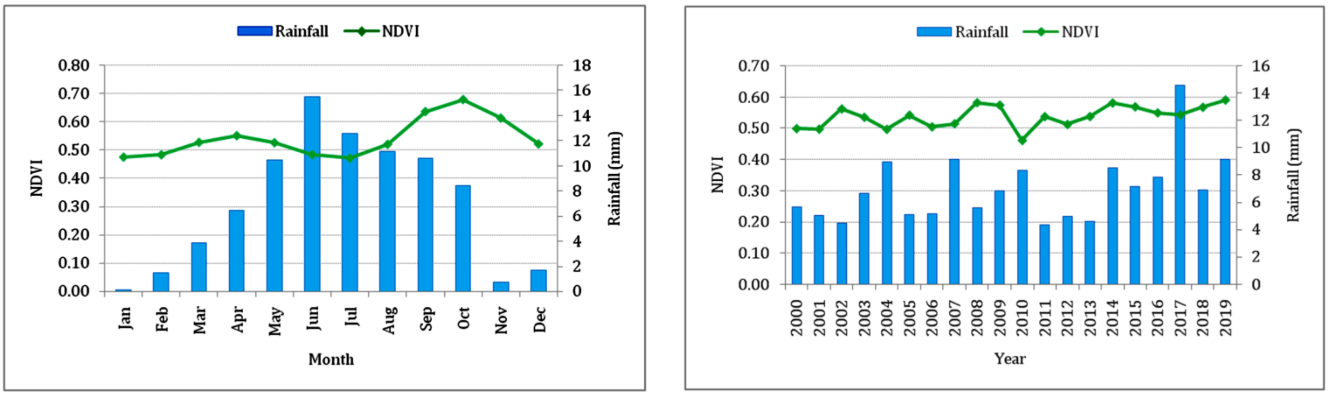

Figure 7. Changes in NDVI and rainfall: (left) monthly average, (right) yearly average

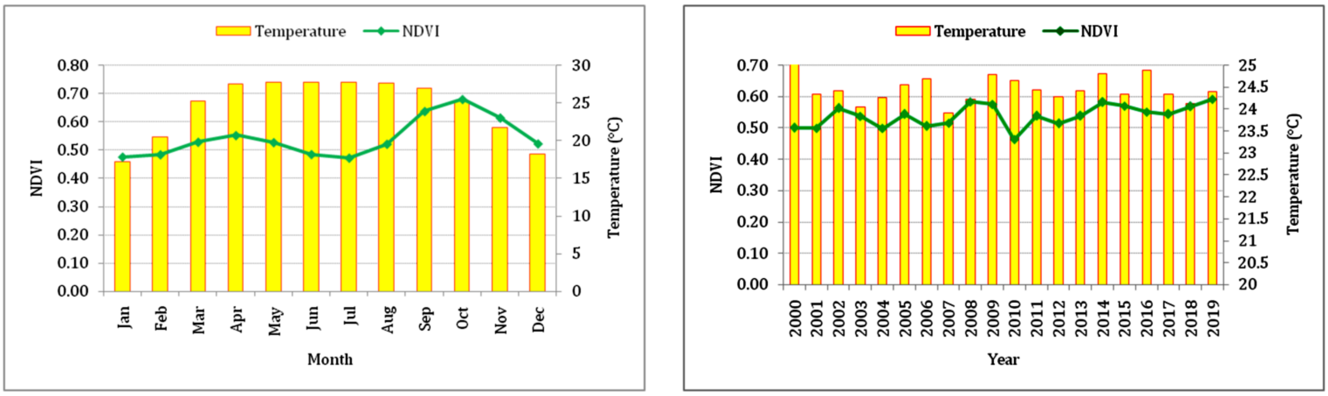

Figure 8. Changes in NDVI and temperature: (left) monthly average, (right) yearly average

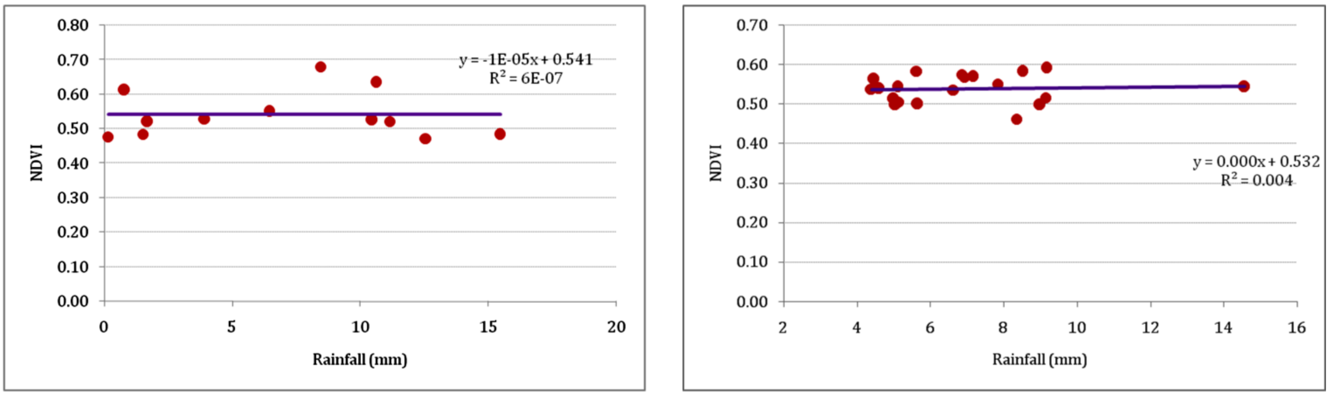

Figure 9. Relation between vegetation and Rainfall: (left) monthly, (right) yearly

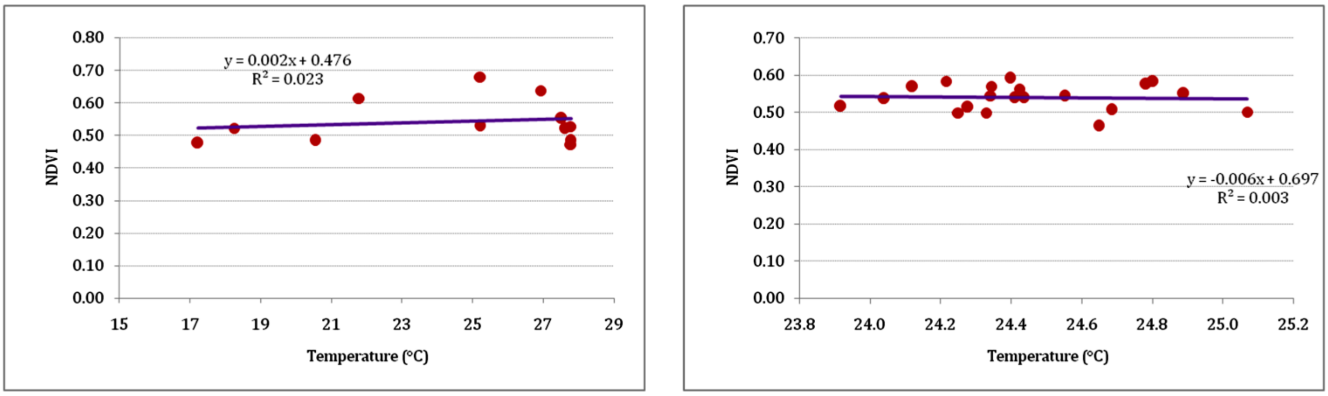

Figure 10. Relation between NDVI and Temperature: (left) monthly, (right) yearly

3.5 Analysis of Lag Period

Since the relationship between monthly NDVI values and climate factors was inconsistent in annual analysis (Fig. 9(right) and 10(right)), the lag between monthly NDVI values and climatic factors was investigated. Fig. 11 depicted the values of the correlations between NDVI and rainfall as well as temperature from 2000 to 2019. The current and previous months' NDVI and climate variables were compared, and the month with the highest correlation coefficient was chosen as the lagged month. At subsequent lags, both positive and negative comparisons are made, with the zero-lag representing the alignment of two data sets at their source.

In terms of rainfall, the study discovered a clear positive relationship (Fig. 11(left)) between NDVI and rainfall in May (r = 0.804, P[1]=0.016), suggesting that vegetation was lagged by four months in receiving rainfall from May. In case of temperature (Fig. 11(right)), the lagged months of NDVI were March, April and June. However, the significant positive correlation in month June (r = 0.74, P = 0.05) and March (r = 0.84, P = 0.002), April (r = 0.68, P = 0.045) indicated that there was monthly lag (5 months, — 2 – 3 months) vegetation due to temperature.

---

[1] *P* indicates significance level. If *P* exceeds 0.05, then it will be insignificant.

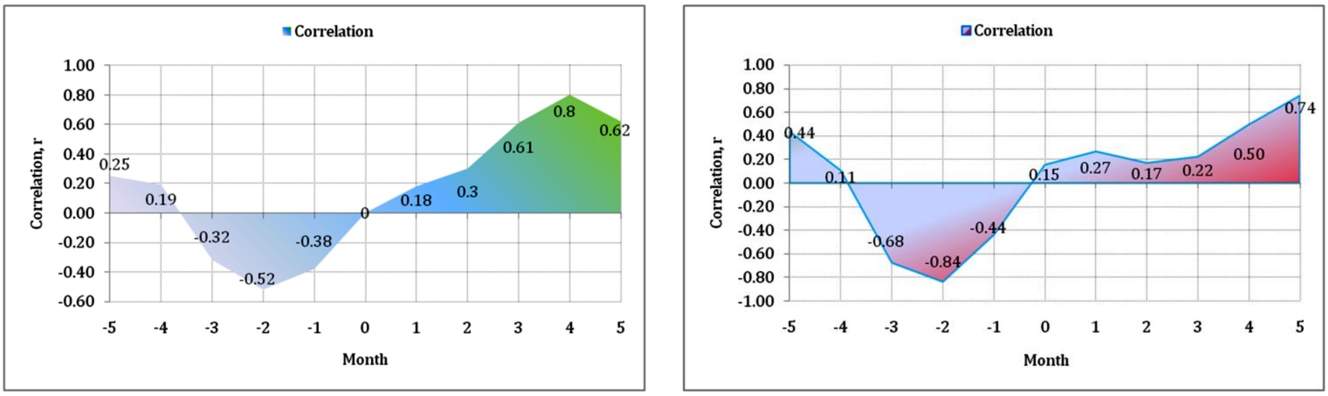

Figure 11. Correlation coefficients between climatic factors: (left) rainfall, (right) temperature and vegetation

4. DISCUSSION

Over the last few decades, vegetation is influenced largely by the effect of human disturbance (Yu et al. 2018), rainfall and temperature change (Li et al. 2019). As a result, studying vegetation change and how it responds to climate change would provide vital information for management of environmental resources (Sun et al. 2021; Li et al. 2019).

The highest (0.59) and lowest (0.46) NDVI values were reported in this analysis in 2019 and 2014, respectively. The NDVI values were ranged from – 1 to 0.09 across the sample region. Various factors promoted the development of vegetation, in which reainfall and temperature playing a significant role (Jiang and Wang 2016). Significant climate change has resulted in the rising of current vegetation pattern (Wang et al. 2005). The NDVI–climate relationship has been difficult to uncover. Some research looked at the influences of rainfall, temperature and anthropogenic activities on arable land in a quantitative way (Shi et al. 2016). Studies have found that the most significant factors influencing vegetation growth were climatic parameters (Pei et al. 2019).

Climate conditions, on the other hand, impact certain places at different time scales. A distinctive relationship between vegetation and climatic factors was observed in different case of annual and monthly time scales. According to MAKESENS there were significant increasing trends ($P < 0.05$) observed in vegetation growth and rainfall. Similarly, a significant upward trend was also found in vegetation coverage on the Loess Plateau (Sun et al. 2015). In terms of an annual basis trend, the rate of vegetation growth was 0.003. Meanwhile, based on the monthly trend, a growth rate of 0.002 to 0.007 was observed. The increasing rate of rainfall, on the other hand, was 0.149 mm/year, which suggested a low growth rate of rainfall on annual basis.

The highest NDVI value was found in October, while the highest rainfall was identified in June in this study. The explanation for this could be that there was sufficient moisture condition for the development of vegetation as there was too much rain in June, with some of it remaining in the subsurface in October. On the other hand, the highest temperature was recorded in July, and the highest NDVI growth was recorded in October. The reason for this could be that decomposition and mineralization of organic matter would be accelerated as the enzymatic activities of photosynthesis would be stimulated due to rise of temperature (Wan et al. 2005).

NDVI was influenced by temperature and rainfall, and cross-correlation analysis revealed a time lag for climate influences. In general, cross-correlation was defined as the degree to which two series were correlated in terms of lag between them, as well as the method of comparing them at successive lags (Davis 2002). Generally, time lags occurred as different climatic variables changed (Davenport and Nicholson 2007). The NDVI reached at a high value of r (0.804) due to rainfall for a certain lag period, which was significant ($P < 0.05$) according to the cross-correlation. Rainfall had a 4-month lag effect on vegetation development, while temperature had a 5 (r = 0.74), − 2 (r = 0.84), and − 3 (r = 0.68) month lag effect on vegetation growth. Sun et al. 2021 also discovered that rainfall in the end of growth period had a lag of 1-2 months on vegetation development, whereas the temperature in the middle of the growth period had a lag impact of one month.

5. CONCLUSION

The current study used the MAKESENS software, cross-correlation, and ANOVA significance test to investigate the trends of NDVI and their lag period due to climatic conditions. The NDVI's temporal variation revealed that vegetation growth was low, particularly on the yearly-time scale (0.003/year). Furthermore, an assessment revealed that vegetation growth on the monthly-time scale was strongly dominated by rainfall and temperature. Finally, the delayed impact of rainfall and temperature on vegetation was revealed. Rainfall from January to April had a four-month lag effect on vegetation growth, while temperature had a 5, - 2, - 3 months lag on vegetation growth. This study's findings revealed changes in vegetation and highlighted the importance of rainfall and temperature in regulating vegetation dynamics.

This study was limited to find out the temporal variation of vegetation. Instead of considering spatiotemporal data, only MODIS NDVI temporal data were used in this scenario. The effect was assessed using two climatic variables (temperature and rainfall), though there were many other variables, including human activity, which were not addressed. Therefore, to better preserve the environment, the effects of climatic conditions on NDVI should be analyzed under the circumstance of global climate change. Meanwhile, the human activities on vegetation should be analyzed quantitatively.

Author contributions

Mst. Mahbuba Khatun: Conceptualization, Methodology, Software, Data curation, Writing-Original draft preparation. **Debajani Chakraborty:** Validation, Writing-Reviewing and Editing. **Ifterkharul Alam:** Visualization, Investigation.

Conflicts of interest

The authors declare no conflicts of interest.

REFERENCES

ARSET Advanced NDVI Webinar Series (2020). Winter 2016, Session 3, MODIS NDVI Time Series. Available online: accessed on November 25, 2020, Retrieved from https://appliedsciences.nasa.gov/sites/default/files/202011/ndvipart3exercise.pdf.

Becker-Reshef I, Justice C, Sullivan M, Vermote E, Tucker C, Anyamba A, Small J, Pak E, Masuoka E, Schmaltz J, Hansen M, Pittman K, Birkett C, Williams D, Reynolds C & Doorn B (2010). Monitoring Global Croplands with Coarse Resolution Earth Observations: The Global Agriculture Monitoring (GLAM) Project. Remote Sensing, 2(6), 1589–1609.

Cai Z & Ofterdinger U (2016). Analysis of groundwater-level response to rainfall and estimation of annual recharge in fractured hard rock aquifers, NW Ireland. Journal of Hydrology, 535, 71-84.

Camberlin P, Martiny N, Philippon N & Richard Y (2007). Determinants of the interannual relationships between remote sensed photosynthetic activity and rainfall in tropical Africa. Remote Sensing of Environment, 106(2), 199–216.

Chu H, Venevsky S, Wu C & Wang M (2019). NDVI-based vegetation dynamics and its response to climate changes at Amur-Heilongjiang River Basin from 1982 to 2015. Science of the Total Environment, 650, 2051–2062.

Davenport M L & Nicholson S E (2007). On the relation between rainfall and the normalized difference vegetation index for diverse vegetation types in east Africa. International Journal of Remote Sensing, 14(12), 2369–2389.

Davis J C (2002). Statistics and Data Analysis in Geology. John Wiley & Sons, Inc., New York, Third Edition, ISBN: 978-0-471-17275-8.

Delbart N, Kergoat L, Toan T L, Lhermitte J & Picard G (2005). Determination of phenological dates in boreal regions using normalized difference water index. Remote Sensing of Environment, 97(1), 26– 38.

Eastman J R, Sangermano F, Machado E A, Rogan J & Anyamba A (2013). Global trends in seasonality of normalized difference vegetation index (NDVI), 1982–2011. Remote Sensing, 5(10), 4799–4818.

Exceluser, 2020: Accessed on 25-6-2020, Retrieved from https://exceluser.com/1069/.

Feng X, Fu B, Piao S, Wang S, Ciais P, Zeng Z, Lü Y, Zeng Y, Li Y, Jiang X & Wu B (2016). Revegetation in China's Loess Plateau is approaching sustainable water resource limits. Nature Climate Change, 6, 1019–1022.

GLAM, 2020: Accessed on 25-6-2020, Retrieved from https://glam1.gsfc.nasa.gov/.

Gu Y, Brown J F, Verdin J P & Wardlow B (2007). A five-year analysis of MODIS NDVI and NDWI for grasslanddrought assessment over the central Great Plains of the United States. Geophysical ResearchLetters, 34(6).

Gu Y, Hunt E, Wardlow B, Basara J B, Brown J F & Verdin J P (2008). Evaluation of MODIS NDVI and NDWI for vegetation drought monitoring using Oklahoma Mesonet soil moisture data. Geophysical ResearchLetters, 35(22).

Islam M N & Al-Amin M (2019). Life behind leaves: Capability, poverty and social vulnerability of tea garden workers in Bangladesh. Labor History, 60(5), 571–587.

Jackson T J, Chen D, Cosh M, Li F, Anderson M, Walthall C, Doriaswamy P & Hunt E R (2004). Vegetation water content mapping using Landsat data derived normalized difference water index for corn and soybeans. Remote Sensing of Environment, 92(4), 475– 482.

Jiang C & Wang F (2016). Environmental Change in the Agro-Pastoral Transitional Zone, Northern China: Patterns, Drivers, and Implications. International Journal of Environmental Research and Public Health, 13, 165.

Kabir M H, Hasan N, Rahman M M, Rahman M A,Khan J A, Hoque N T, Bhuiyan M R Q, Mou S M, Jahan R &Rahmatullah M (2014). A survey of medicinal plants used by the Deb barma clan of the Tripura tribe of Moulvibazar district, Bangladesh. Journal of Ethnobiology and Ethnomedicine, 10(19).

Li C, Wang J, Hu R, Yin S, Bao Y & Ayal D Y (2018). Relationship between vegetation change and extreme climate indices on the Inner Mongolia Plateau, China, from 1982 to 2013. Ecological Indicators, 89, 101–109.

Li Y, Xie Z, Qin Y & Zheng Z (2019). Estimating Relations of Vegetation, Climate Change, and Human Activity: A Case Study in the 400 mm Annual Precipitation Fluctuation Zone, China. Remote Sensing, 11, 1159.

Liu S L & Wang T (2012). Climate change and local adaptation strategies in the middle Inner Mongolia, northern China. Environmental Earth Sciences, 66, 1449–1458.

Liu Y & Lei H (2015). Responses of natural vegetation dynamics to climate drivers in China from 1982 to 2011. Remote Sensing, 7(8), 10243–10268.

Mao J, Shi X, Thornton P E, Hoffman F M, Zhu Z &Myneni R B (2013). Global Latitudinal-Asymmetric Vegetation Growth Trends and Their Driving Mechanisms: 1982- 2009. Remote Sensing, 5(3), 1484–1497.

Meng X, Gao X, Li S & Lei J (2020). Spatial and temporal characteristics of vegetation NDVI changes and the driving forces in Mongolia during 1982–2015. Remote Sensing, 12(4), 603.

Na L, Na R, Zhang J, Tong S, Shan Y, Ying H, Li X &Bao Y (2018). Vegetation Dynamics and Diverse Responses to Extreme Climate Events in Different Vegetation Types of Inner Mongolia. Atmosphere, 9(10), 394.

Nemani R R, Keeling C D, Hashimoto H, Jolly W M, Piper S C, Tucker C J, Myneni R B & Running S W (2003). Climate-driven increases in global terrestrial net primary production from 1982 to 1999. Science, 300, 1560–1563.

Patra K C (2008). Hydrology and water resources engineering. New Delhi: Narosa Publishing House, Second edition, ISBN:978-81-7319-846-5.

Pei Z, Fang S, Yang W, Wang L, Wu M, Zhang Q, Han W &Khoi D N (2019). The Relationship between NDVI and Climate Factorsat Different Monthly Time Scales: A Case Study of Grasslands in Inner Mongolia, China (1982–2015). Sustainability, 11(24), 7243.

Piao S, Tan J, Chen A, Fu Y H, Ciais P, Liu Q, Janssens I A, Vicca S, Zeng Z, Jeong S J, Li Y, Myneni R B, Peng S, Shen M &Penuelas J (2015). Leaf onset in the northern hemisphere triggered by daytime temperature. Nature Communications, 6, 6911.

Piao S, Wang X, Ciais P, Zhu B, Wang T & Liu J (2011). Changes in satellite-derived vegetation growth trend in temperate and boreal Eurasia from 1982 to 2006. Global Change Biology, 17(10), 3228–3239.

Posavec K, Vukojević P, Ratkaj M & Bedeniković T (2017). Cross-correlation Modelling of Surface Water–Groundwater Interaction Using the Excel Spreadsheet Application. The Mining-Geology-Petroleum Engineering Bulletin, 25-32.

Rahman M Z, Hossain M S, Kamal A S M M, Siddiqua S, Mustahid F & Farazi A H (2018). Seismic site characterization for Moulvibazar town, Bangladesh. Bulletin of Engineering Geology and the Environment, 77, 1451–1471.

Rasmus F & Simon R P (2012). Evaluation of Earth Observation based global long term vegetation trends—Comparing GIMMS and MODIS global NDVI time series. Remote Sensing of Environment, 119, 131–147.

Salmi T, Maatta A, Anttila P, Ruoho-Airola T & Amnell T (2002). Detecting Trends of Annual Values of Atmospheric Pollutants by the Mann-Kendall Test and Sen's Slope Estimates -The Excel Template Application MAKESENS. User Manual, Air Quality, Finnish Meteorological Institute, Helsinki, Finland. Accessed on 25-9-2020, Retrieved from https://en.ilmatieteenlaitos.fi/documents/30106/335634754/MAKESENS Manual_2002.pdf/25bbe115-7f7e-4de3-97d8-5a96ac88499f.

Shen X J, Liu B H & Zhou D W (2016). Using GIMMS NDVI time series to estimate the impacts of grassland vegetation cover on surface air temperatures in the temperate grassland region of China. Remote Sensing Letters, 7, 229–238.

Shilong P, Wang X, Ciais P, ZHU B, Wang T & Liu J (2011). Changes in satellite-derived vegetation growth trend in temperate and Boreal Eurasia from 1982 to 2006. Global Change Biology, 17(10), 3228–3239.

Shi X, Wang W & Shi W (2016). Progress on quantitative assessment of the impacts of climate change and human activities on cropland change. Journal of Geophysical Sciences, 26, 339–354.

Sun H, Wang J, Xiong J, Bian J, Jin H, Cheng W & Li A (2021). Vegetation Change and Its Response to Climate Change in Yunnan Province, China. Advances in Meteorology, 2021, 1-20.

Sun W Y, Song X Y, Mu X M, Gao P, Wang F & Zhao G J (2015). Spatiotemporal vegetation cover variations associated with climate change and ecological restoration in the Loess Plateau. Agricultural and Forest Meteorology, 209, 87–99.

Tucker C J (1979). Red and photographic infrared linear combinations for monitoring vegetation. Remote Sensing of Environment, 8(2), 127–150.

USDA FAS (2020). GLAM-Global Agricultural Monitoring. Accessed on 21-9-2020, Retrieved from http://www.pecad.fas.usda.gov/glam.cfm (accessed on November 21, 2020).

Wan S, Hui D, Wallace L & Luo Y (2005). Direct and indirect effects of experimental warming on ecosystem carbon processes in a tallgrass prairie. Global Biogeochemical, Cycles, 19(2), GB2014, doi:10.1029/2004GB002315.

Wang X, Chen F H, Dong Z & Xia D (2005). Evolution of the southern Mu Us Desert in north China over the past 50 years: An analysis using proxies of human activity and climate parameters. Land Degradation & Development, 16(4), 351–366.

Wang Y, Shen X, Jiang M & Lu X (2020). Vegetation change and its response to climate change between 2000 and 2016 in marshes of the Songnen plain, northeast China. Sustainability, 12(9), 3569.

Wikipedia, 2020: Moulvibazar. Accessed on 25-6-2020, Retrieved from https://en.wikipedia.org/wiki/Moulvibazar.

Wu D, Zhao X, Liang S, Zhou T, Huang K, Tang B & Zhao W (2015). Time-lag effects of global vegetation responses to climate change. Global Change Biology, 21(9), 3520–3531.

Xu Y, Yang J & Chen Y (2015). NDVI-based vegetation responses to climate change in an arid area of China. Theoretical and Applied Climatology, 126, 213–222.

Yu X, Ding S, Zou Y, Xue Z, Lyu X & Wang G (2018). Review of rapid transformation of floodplain wetlands in northeast China: roles of human development and global environmental change. Chinese Geographical Science, 28(4), 654–664.

Zhang Y, Gao J, Liu L, Wang Z, Ding M & Yang X (2013). NDVI-based vegetation changes and their responses to climate change from 1982 to 2011: a case study in the Koshi river basin in the middle Himalayas. Global and Planetary Change, 108, 139–148.

Zhao X, Hu H, Shen H, Zhou D, Zhou L, Myneni R B & Fang J (2015). Satellite-indicated long-term vegetation changes and their drivers on the Mongolian Plateau. Landscape Ecology, 30, 1599–1611.

Turkish Journal of Engineering
https://dergipark.org.tr/en/pub/tuje
e-ISSN 2587-1366

The modelling, simulation, and implementation of wireless power transfer for an electric vehicle charging station

Mehmet Çiçek*[1], Mustafa Gençtürk[1], Selami Balcı[2], Kadir Sabancı[2]

[1]Karamanoglu Mehmetbey University, Graduate School of Natural and Applied Sciences, Department of Electrical and Electronics Engineering, Karaman, Turkey
[2]Karamanoglu Mehmetbey University, Faculty of Engineering, Department of Electrical and Electronics Engineering, Karaman, Turkey

Keywords
Wireless Power Transfer
Electric Vehicle
Charging Station

ABSTRACT

Recently, with the developing environmental awareness, electric vehicles are increasing even more. For this reason, different searches have emerged to solve the problems related to meeting the energy needs of electric vehicles and charging their batteries quickly and reliably. One of these ideas is wireless power transfer (WPT) battery charging systems, which researchers have focused on for the past two decades. In this study, a wireless charging station that can be used to charge the batteries of electric vehicles is designed and examined by applying it to a prototype vehicle. Also, it is examined that the designed system can be adapted with renewable energy sources (such as solar energy) independently of a local energy source. It is aimed with the WPT prototype to realize a more efficient system for the 10 W power level and 86 kHz. The electromagnetic modelling of WPT is designed using ANSYS-Electronics/Maxwell software. Ultimately, the power electronics circuit performance of this system was analyzed with ANSYS Electronics / Simplorer software for co-simulation.

1. INTRODUCTION

Wireless power transmission (WPT) has become a popular topic, especially in the last two decades. Many researchers study it with much greater interest. WPT based on the principle of transmitting electrical power with magnetic coupling (Kuzey, 2017; Tesla, 1900b). The emergence of WPT and the implementation of this principle has become possible after nearly two centuries (Fawwaz and Ulaby, 2015; Sun et al., 2018). At the end of this process, Nikola Tesla made some experiments on the wireless transmission of electrical energy in 1899 and received a patent on WPT on March 20, 1900 (Tesla, 1898, 1900a).

After the applicability of WPT in different fields was understood, it has started to be understood that the power transmission method could also take different forms. The first MASER (Microwave Amplification by Stimulated Emission of Radiation) oscillator, which was developed in 1954, is seen as the first example (Schawlow et al., 1960). This invention would later lead to the discovery of LASER (Light Amplification by Stimulated Emission of Radiation) in 1960 (Maiman, 1967).

The effects of WPT on medical electronics started with the use of implant devices. John Schuder proposed the transcutaneous WPT system to supply the energy needs of implant devices in 1961 (Mahmud, 2016; Schuder, 2002).

On the other hand, William Brown designed an antenna, which is called rectenna (rectifying antenna) in 1964. And he used the rectenna to canalize the microwaves to a model helicopter, which we can call a simple drone. This drone's energy was sourced from the microwave beam by using WPT. In his presentation,

---

* **Corresponding Author**

*(mehmetcicek1789@gmail.com) ORCID ID 0000-0003-2816-2020
(mustafagencturk00@gmail.com) ORCID ID 0000-0001-5198-4896
(sbalci@kmu.edu.tr) ORCID ID 0000-0002-3922-4824
(kadirsabanci@kmu.edu.tr) ORCID ID 0000-0003-0238-9606

Cite this article

Çiçek M, Gençtürk M, Balcı S & Sabancı K (2022). The modelling, simulation, and implementation of wireless power transfer for an electric vehicle charging station. Turkish Journal of Engineering, 6(3), 223-229

Research Article / DOI: 10.31127/tuje.930933

Received: 01/05/2021; Accepted: 29/06/2021

William C. Brown transferred 270 watts of power to a height of 50 ft (15.24 m) (Brown, 1965, 1969).

Also, Peter E. Glaser came up with the idea of SPS (Solar Energy System) or SBPS (Solar Based Power System) in 1973, where WPT systems could be applied. Thus, a diversity of resources is provided for WPT systems, which will lead to many different research and investigation areas in the future (Glaser, 1973).

Zhao *et al.* conducted studies on electromagnetic induction and WPT in 2012 (Zhang and Zhao, 2014). Although WPT was on the researcher's sights from time to time in the last century, it is not received the expected attention due to its inefficiency and difficulties in implementation. Nevertheless, in 2007, researchers at MIT (Massachusetts Institute of Technology) transmitted a 60 W power level to a distance of 2 meters with WPT (Kurs et al., 2007).

In the other studies conducted for the last 20 years, researchers focused on resonance magnetic coupling studies because of the low efficiency of magnetic induction and inductively coupled systems.

Thrimawithana *et al.* controlled the voltage induced in the primary coils with the control technique they performed on the primary side and provided inductive power transfer by regulating the primary current. Also, they transferred 150 W power to the secondary side at a frequency of 20kHz and compared the results of the experimental and the simulation results (Thrimawithana and Madawala, 2010).

Imura and Hori 2011 analyzed the relationship between the air gap and the efficiency by using the Neumann formula and equivalent circuit for magnetic resonance coupling.

Kuzey, in his thesis in 2017, designed a WPT system that can be used in charging electric vehicle batteries. He cross-examined the 20 cm and 30 cm air-gapped WPT topologies for two models for 15 kW and 45 kW power levels. He found the maximum efficiency of the system in the ideal condition of 15 kW power to be 75.38% (Kuzey, 2017; Kuzey et al., 2017). On the other hand, Lee examined in his study in 2019 that WPT systems can be adapted in different sizes in places where it is difficult to reach. Also, he transferred 47 W power with 52% efficiency with WPT at a distance of 60 cm which is the approach distance of the high voltage lines (Lee et al., 2019).

In 2020, Ustun *et al.* 2020 developed a simulation model by using an artificial bee colony algorithm to predict the variables of the inductively coupled WPT system designed for electric vehicles. In their study, they determined that the analysis of the WPT circuits related to the charging efficiency can be easily calculated with the proposed model without considering long time simulation and complex equations.

WPT can also be used as a new charging technique for Unmanned Aerial Vehicles (UAVs). Le et al. 2020 analyzed different WPT charging technique for UAVs. they searched WPT near-field techniques capacitive, inductive, and resonant inductive coupling methods for UAVs in their study. They addressed possible ways to apply these techniques for UAVs.

Frechter and Kuperman 2020 presented the analytical investigation and design of a WPT system for a through-glass AC power transfer system in their study.

Recent technological advances are also showed us that there are some other new ways to produce a WPT system. Kim et al tried to secure sustainable electrical power in human bodies by using an active photonic WPT approach in their study. They designed an active photonic WPT which is consists of a pair of the skin-attachable photon source patch and the photovoltaic device array integrated into a flexible medical implant (Kim et al., 2020).

Despite all studies, WPT efficiency is still a disadvantage of this system. Yan *et al.* designed and analyzed a multi-transmitter system for greater WPT efficiency. This system also aimed more efficiency under lateral-misalignment conditions (Yan et al., 2020). Assawaworrarit *and Fan 2020.* searched for the increase of WPT's efficiency by using a switch-mode implementation.

The energy harvesting system is also a different type of WPT. Kim *et al.* 2020 used this idea to design a WPT system. They tested WPT efficiency at different modulation types and at different waveforms. Shen *et al.* 2021, designed a closed-loop WPT with adaptive waveform and beamforming.

The alignment of the receiver and the transmitter is also an important variable for WPT’s efficiency. Liu *et al.* 2021 examined the electrical parameters of a compensation inductance and the transmitter to determine the receiver position.

WPT has some other application areas such as insulation from environmental conditions. Wang *et al.* examined a single-phase shaded-pole induction motor system with WPT. They achieved a WPT's efficiency of 77% with a 20 mm transfer distance (Wang et al., 2021).

At WPT systems, the design and the shape of receiver and transmitter coils are very significant factors for efficiency. Yakala *et al.* 2021 studied the circular transmitter and receiver coils design for WPT system in battery charging applications of electrical vehicles. They designed a power pad for WPT. It can transfer the power of 3.7 kW for a distance of 100 mm, at a vertical offset of 150 mm (Yakala et al., 2021) .

Today, the awareness of human health and the environment is very developed, so one of the first questions that come to mind regarding this technology is the effects of WPT on human health and the environment. Although researches which are about WPT effect on humans health is still ongoing, they show that the magnetic field in WPT technology is within the international boundaries for human health (Baikova et al., 2018; Christ et al., 2013; Kuzey et al., 2017; Sun et al., 2018).

In this study, the charging system of electric vehicles, which is one of the application and research areas of WPT, is designed as a prototype. Also, it is examined the energy-storing obtained from the alternative energy source (Solar energy). So that the designed system can be kept ready for use independent of the grid. In the designed WPT system, it is aimed to achieve optimum efficient power transfer with minimum air gap and low coupling coefficient. For a 10 W model with a 1.5-2 cm parametric distance value, the WPT in power transmission is examined. First of all, the variables of the designed WPT system are calculated. Then, with these variables, coils are designed in ANSYS Electronics/Maxwell software and the magnetic model simulation of WPT is examined. The performance of the model is analyzed by simulating the designed and simulated transceiver (transmitter and receiver) coils simultaneously with the WPT electrical equivalent circuit model created in ANSYS Electronics/Simplorer software. Then, the designed and simulated system is applied and finally, the simulation results are compared with the application results.

2. MATERIAL AND METHOD

2.1. Examination of the Basic Circuit Block Diagram of the Designed WPT System

The block diagram showing the basic circuit structure of the designed WPT system is shown in Figure1. On the block diagram, the supply of the system is modelled from both the renewable energy source and the network. A high frequency switched DC / AC inverter is designed for the charging station. Then, transmitter coil design and calculations are made. After the charging station is completed, a receiver coil, AC / DC rectifier and battery measurement and monitoring system are placed on the vehicle to feed the vehicle battery.

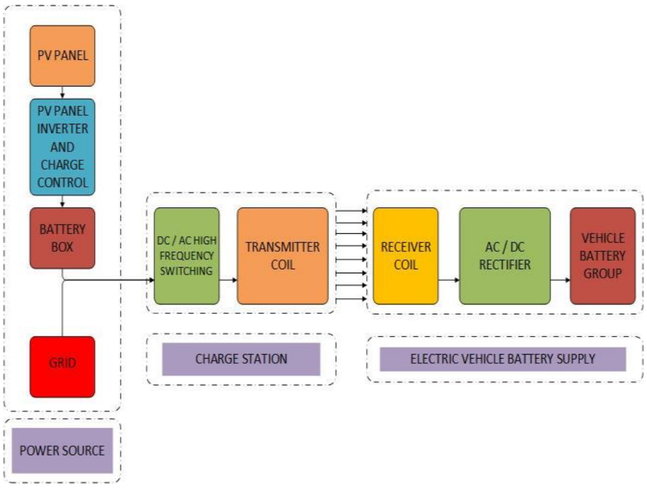

Figure 1. The block diagram of proposed WPT system

2.2. Determination of the Resonance Frequency for Designed WPT System

In this study, the "Tank Circuit", which is based on the electromagnetic resonance circuit (RLC circuit) and can store very large energies with ideally infinite oscillation, is used to provide resonance. However, due to the absolute existing resistance and physical limitations, the resonance frequency has to be calculated at a certain value. There are two common types of resonant-tank circuits. The first one is the series tank circuit which is given in Figure 2, and the other one is the parallel tank circuit which is given in Figure 3.

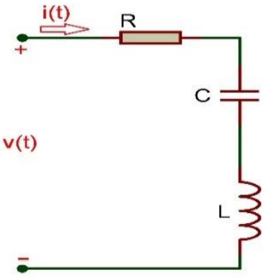

Figure 2. Series RLC circuit

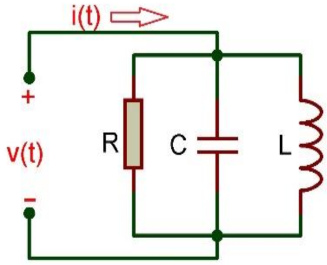

Figure 3. Parallel RLC circuit

For a given frequency value, the inductance (L) and capacitance (C) become equal for the maximum current to flow through the circuit in the resonance state. First of all, the transmitter and the receiver coils are calculated and designed. The inductance value (L) of the coils is calculated by Equation 1 (Chapman, 2012; Cheng, 1983).

$$L = \frac{\mu_0 . N^2 . A}{l} \tag{1}$$

Where, μ_0 permeability of the vacuum, N is the number of turns, l is the length of the coil, and A is the diameter of the coil wire. In this case, the resonance frequency (ω_0) is calculated by Equation 2.

$$\omega_0 = \frac{1}{\sqrt{LC}} \tag{2}$$

The resonance frequency is calculated for the designed WPT system in this study which is aimed at 10 W power transmission at 86 kHz.

2.3. Simulation Studies

The variables determined in the system designing and modelling are used in the ANSYS Electronics/Maxwell software to create the magnetic model of the coils.

The designed model in the Maxwell is shown in Figure 4. In this model, the grey-coloured coil is the primary coil with 22 turns which is the transmitter and the green-coloured coil is the secondary coil with 10 turns which is the receiver coil.

The inductance values of the designed coils are also examined in the simulation studies. Mutual inductance and self inductances of the coils are shown in Figure 5.

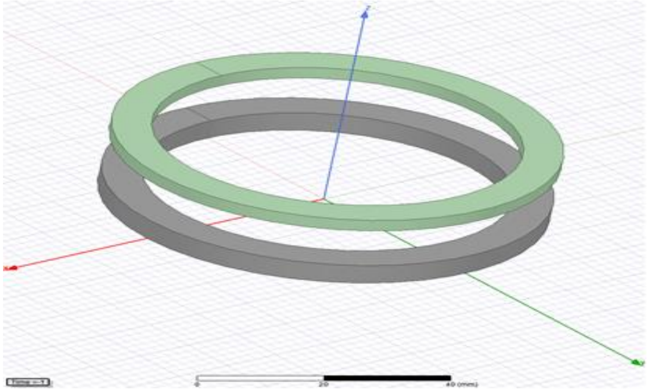

Figure 4. Designed coils with Ansys-Maxwell

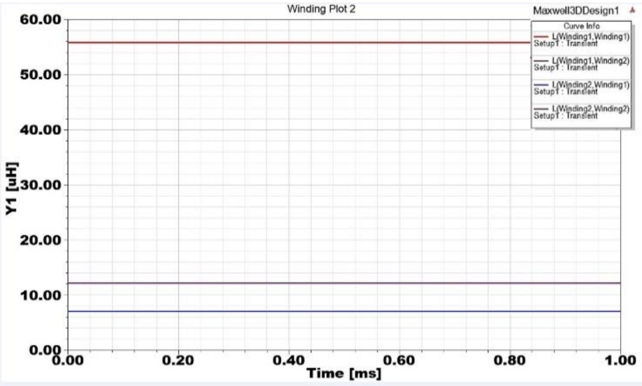

Figure 5. The mutual and self inductances of coils

In this modelling, magnetic flux distribution and coupling effect are also examined. Magnetic flux distribution and coupling effect are shown in Figure 6.

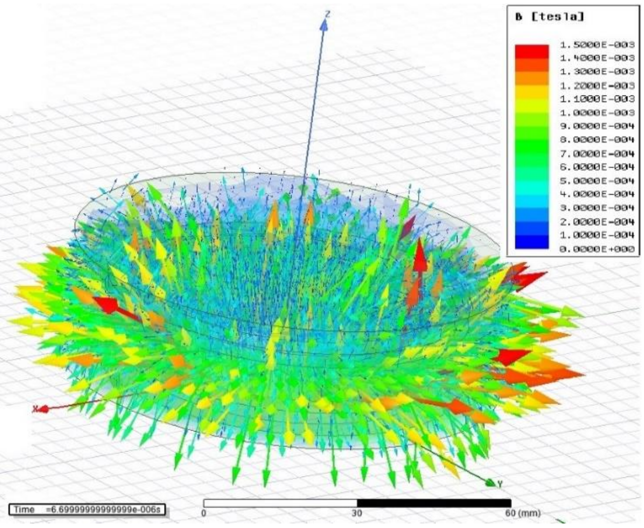

Figure 6. Magnetic flux distribution and coupling effect

An electrical equivalent circuit model for the designed WPT system is designed in the ANSYS Electronics/Simplorer program. Afterwards, the ANSYS Electronics/Simplorer program is simulated simultaneously with realized transceiver coil models in the Maxwell. The performance of the whole of the designed system is analyzed. The Simplorer circuit model of the designed WPT system is shown in Figure 7.

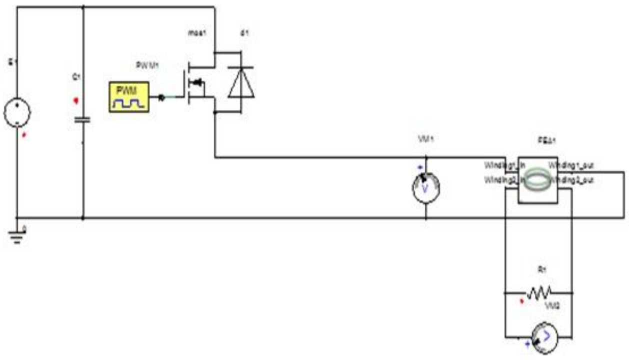

Figure 7. Ansys - Simlporer circuit model

The design of the receiver circuit to be placed on the model vehicle is also made along with the simulation studies of the receiver and transmitter coils. A real-time voltmeter is added to the design on the receiver circuit. The voltmeter shows the voltage level to be obtained from the receiver coil. Thus, it is aimed that this measurement is not affected by the current battery of the model vehicle with the D1 diode. The designed receiver coil measurement circuit and AC / DC rectifier circuit diagram are shown in Figure 8.

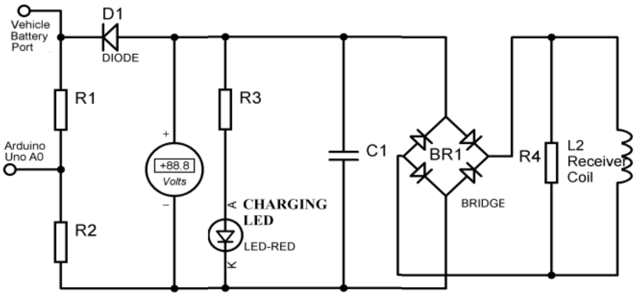

Figure 8. The circuit of the vehicle side

2.4. Realization of The Designed Model

The model which was designed and simulated, manufactured as a prototype. The list of used materials is shown in Table 1.

Table 1. The technical specifications of WPT circuit

Materials	Function
Arduino Uno	The control unit at the model vehicle
Arduino Nano	The control unit of PWM
Mosfet (Driver Module of IRF520 MOSFET)	The switching unit at the WPT system
The Designed Coils:	
0.60 mm^2 10 Turns-Reciver Coil 0.60 mm^2 22 Turns – Transmitter Coil	The components which are used for energy transfer at the WPT system
LCD	The element used to see the voltage and distance values on the model vehicle
Ultrasonic Distance Sensor (HC-SR04)	The element used to prevent misaligned problems
PV Module	Power Source of the WPT system

The receiver circuit of the designed model is assembled to the model vehicle. The assembly of the receiver coil and the rectifier circuit is shown in Figure 9.

Figure 9. The assembly of the receiver circuit

A charging station has also made for the electric vehicle. Theoretical, the energy which is obtained by the PV module is stored at the battery cell. Afterwards, the energy is switched by the designed WPT system at 86 kHz frequency. The designed charging station is shown in Figure 10.

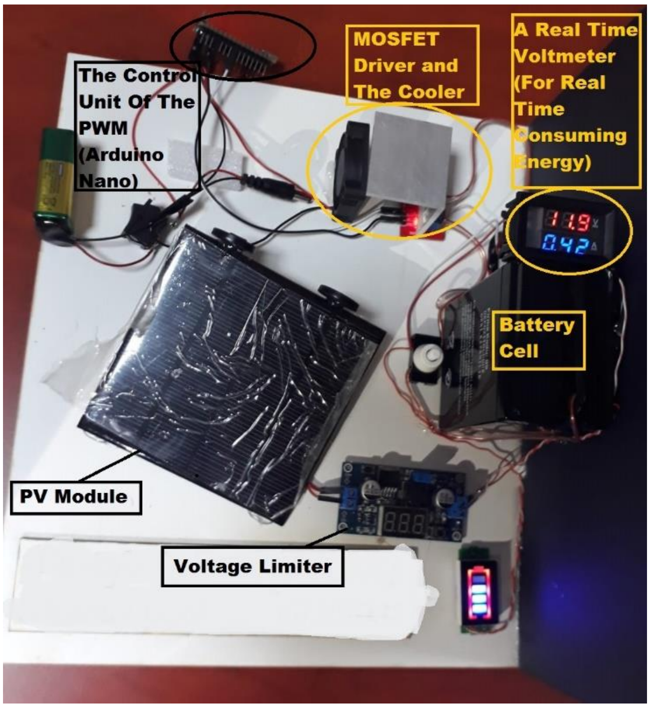

Figure 10. The PV panel and the WPT system

The charging station and the WPT system are designed as a whole system which is combined with the vehicle and the station. After that, all components are assembled and the designed system is manufactured. The final situation of the manufactured system is shown in Figure 11.

Figure 11. Prototype imaging of the designed wireless charging station

3. RESULTS

In this study, a WPT system that is operated at 86 kHz frequency is designed, simulated, and implemented. The maximum efficiency of WPT is obtained 75% at the ideal condition for a 10 W power value. The output signals of the designed system are also performed simulation and experimental tests at the 95% power level. Thus, the output signals obtained as a result of these tests are shown in Figures 12 and 13, respectively.

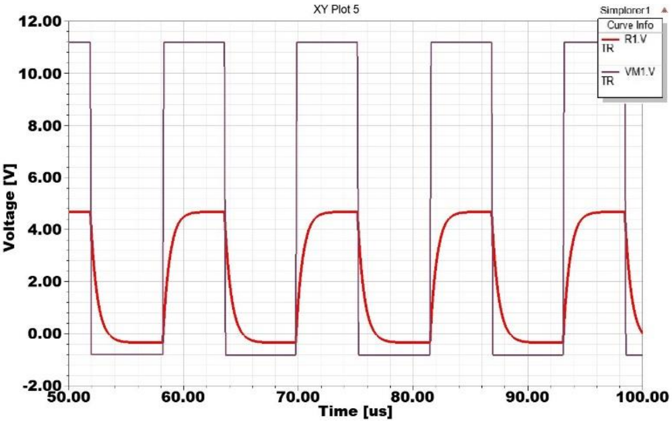

Figure 12. The output signal with simulation reports

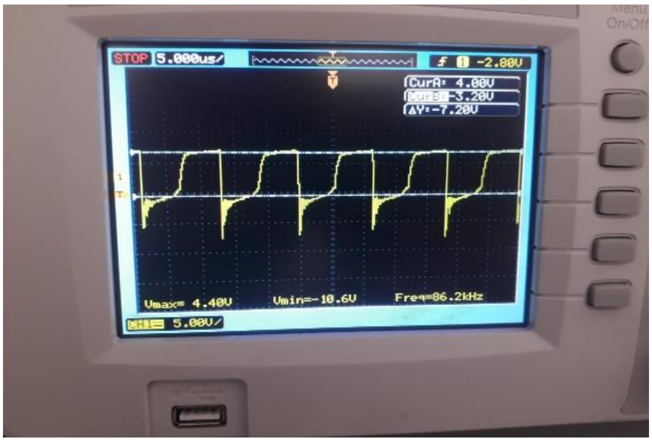

Figure 13. The output signal with scope image reports

4. CONCLUSION

This paper presents a charging station for electric vehicles based on WPT. The proposed WPT system is designed, simulated and implemented. The designed system shows that WPT charging systems can be realized independently from the grid by using alternative energy sources. In addition, the designed WPT system is derived from the flyback converter topology. Firstly, the power electronics circuit of the WPT system was simulated with the Ansys-Simplorer software. The optimum distance value between the coils is determined. Then the prototype of the WPT system is built and experimental studies are carried out at 86 kHz and 10 W. According to the experimental studies, the maximum efficiency of the WPT system was found to be 75% in the ideal state of the topology. The results obtained in the study showed that a similar application can be applied to real vehicles with real high power level.

ACKNOWLEDGEMENTS

The authors would like to acknowledge Karamanoğlu Mehmetbey University for their support at the 1st National Engineering and Technology Congress.

The authors also would like to acknowledge the financial support of the Scientific and Technological Research Council of Turkey under project number TUBITAK-1139B411802253 providing support under 2209-B Industry Oriented Undergraduate Research Project Support Program.

Author contributions

Mehmet Çiçek: Conceptualization, Design, Writing draft preparation, Literature review, Software (ANSYS Electronics), Visualization, Design of the electronic circuits, Investigation, Critical review. **Mustafa Gençtürk:** Conceptualization, Design, Writing draft preparation, Literature review, Software (Arduino), Visualization, Design of the electronic circuits, Investigation, Critical review. **Selami Balcı:** Conceptualization, Methodology, Design, Software (ANSYS Electronics), Data collection and/or processing, Analysis and interpretation, Critical review, Inspection. **Kadir Sabancı:** Conceptualization, Methodology, Software (Arduino), Data collection and/or processing, Analysis and interpretation, Design of the electronic circuits, Critical review, Inspection

Conflicts of interest

The authors declare no conflicts of interest.

REFERENCES

Assawaworrarit S & Fan S (2020). Robust and efficient wireless power transfer using a switch-mode implementation of a nonlinear parity–time symmetric circuit. *Nature Electronics*, *3*(5), 273–279.

Baikova E, Romba L, Valtchev S, Melicio R & Pires V F (2018). *Electromagnetic Influence of WPT on Human's Health. October 2018*, 141–161.

Brown W C (1965). *Experimental Airborne Microwave Supported Platform*.

Brown W C (1969). *Microwave To DC Converter*.

Chapman S J (2012). *Electric Machinery Fundamentals*.

Cheng D K (1983). *Field and Wave Electromagnetics*.

Christ A, Douglas M G, Roman J M, Cooper E B, Sample A P, Waters B H, Smith J R & Kuster N (2013). Evaluation of wireless resonant power transfer systems with human electromagnetic exposure limits. *IEEE Transactions on Electromagnetic Compatibility*, *55*(2), 265–274.

Fawwaz T, Ulaby U R (2015). *Fundamentals of applied electrostatics*.

Frechter Y & Kuperman A (2020). Analysis and design of inductive wireless power transfer link for feedback-less power delivery to enclosed compartment. *Applied Energy*, *278*(August), 115743.

Glaser P (1973). *Method and Apparatus for converting solar Radiation to electrical Power*. 1–4.

Imura T & Hori Y (2011). Maximizing air gap and efficiency of magnetic resonant coupling for wireless power transfer using equivalent circuit and Neumann formula. *IEEE Transactions on Industrial Electronics*, *58*(10), 4746–4752.

Kim J, Seo J, Jung D, Lee T, Ju H, Han J, Kim N, Jeong J, Cho S, Seol J H & Lee J (2020). Active photonic wireless power transfer into live tissues. *Proceedings of the National Academy of Sciences of the United States of America*, *117*(29), 16856–16863.

Kurs A, Karalis A, Moffatt R, Joannopoulos J D, Fisher P & Soljačić M (2007). Wireless power transfer via strongly coupled magnetic resonances. Science, *317*(5834), 83–86.

Kuzey S (2017). *Elektrikli Araç İçin Endüktif Manyetik Bağlı Güç Aktarım Sistemi Tasarımı*. Gazi Üniversitesi.

Kuzey S, Balci S & Altin N (2017). Design and analysis of a wireless power transfer system with alignment errors for electrical vehicle applications. *International Journal of Hydrogen Energy*, *42*(28), 17928–17939.

Le A, Truong L, Quyen T, Nguyen C & Nguyen M (2020). Wireless Power Transfer Near-field Technologies for Unmanned Aerial Vehicles (UAVs): A Review. *EAI Endorsed Transactions on Industrial Networks and Intelligent Systems*, *7*(22), 162831.

Lee S H, Yi K P & Kim M Y (2019). 6.78-MHz, 50-W wireless power supply over a 60-cm distance using a GaN-based full-bridge inverter. *Energies*, *12*(3).

Liu Z, Wang L, Tao C, Li F, Guo Y, Li S & Zhang Y (2021). Receiver Position Identification Method of Wireless Power Transfer System Based on Magnetic Integration Inductance. *IEEE Transactions on Industry Applications*, *9994*(c), 1–1.

Mahmud M H (2016). *Efficient Wireless Power Charging of Electric Vehicle by Modifying the Magnetic Characteristics of the Medium* (Issue August).

Maiman T H (1967). *Ruby laser system*. 3,353,115.

Schuder J C (2002). Powering an artificial heart: Birth of the inductively coupled-radio frequency system in 1960. Artificial Organs, 26(11), 909–915.

Shen S, Kim J & Clerckx B (2021). *Closed-Loop Wireless Power Transfer with Adaptive Waveform and*

Beamforming: Design, Prototype, and Experiment. 1–9.

Sun L, Ma D & Tang H (2018). A review of recent trends in wireless power transfer technology and its applications in electric vehicle wireless charging. Renewable and Sustainable Energy Reviews, 91(December 2016), 490–503.

Tesla N (1898). Method of and Apparatus for Controlling Mechanism of Moving Wessels.

Tesla N (1900a). Apparatus For Transmission of Electrical Energy. In ACM SIGGRAPH Computer Graphics.

Tesla N (1900b). N. Tesla. System of Transmission of Electrical Energy. 1–6.

Thrimawithana D J & Madawala U K (2010). A primary side controller for inductive power transfer systems. Proceedings of the IEEE International Conference on Industrial Technology, 661–666.

Ustun D, Balci S & Sabanci K (2020). A parametric simulation of the wireless power transfer with inductive coupling for electric vehicles, and modelling with artificial bee colony algorithm. *Measurement: Journal of the International Measurement Confederation*, *150*, 107082.

Wang H, Chau K T, Lee C H T & Jiang C (2021). Wireless Shaded Pole Induction Motor with Half-bridge Inverter and Dual-Frequency Resonant Network. *IEEE Transactions on Power Electronics*, *8993*(c), 1–1.

Yakala R K, Pramanick S, Nayak D P & Kumar M (2021). Optimization of Circular Coil Design for Wireless Power Transfer System in Electric Vehicle Battery Charging Applications. *Transactions of the Indian National Academy of Engineering*, *0123456789*.

Yan Z, Yang B, Liu H, Chen C, Waqas M, Mai R & He Z (2020). Efficiency Improvement of Wireless Power Transfer Based on Multitransmitter System. *IEEE Transactions on Power Electronics*, *35*(9), 9011–9023.

Zhang Y & Zhao Z (2014). Frequency splitting analysis of two-coil resonant wireless power transfer. *IEEE Antennas and Wireless Propagation Letters*, *13*(2), 400–402.

Turkish Journal of Engineering
https://dergipark.org.tr/en/pub/tuje
e-ISSN 2587-1366

Single and multisite detailed kinetic models for the adsorption and desorption of NO_2 over Cu based NH_3-SCR catalyst

Selmi Erim Bozbağ[*1]

[1] *Koç University, College of Engineering, Department of Chemical and Biological Engineering, Sarıyer, Istanbul, Turkey*

Keywords
NO_2 storage
NH_3 storage
Kinetic model
TPD
NH_3-SCR

ABSTRACT

Kinetic modeling of NH_3 Selective Catalytic Reduction (NH_3-SCR) of NOx in Cu-chabazite washcoated monolithic reactors has recently become an important task for design, control and calibration of heavy-duty engine aftertreatment systems. Development of detailed and accurate kinetic models rely on the correct simulation of the NO_2 and NH_3 storage at different conditions. Here, different kinetic schemes for NO_2 adsorption and desorption were developed and compared to experimental data. For this purpose, firstly, realistic values of the active Cu sites in the Cu-zeolite were obtained using the temperature programmed desorption (TPD) of NH_3 and NO_2 which showed fractional coverages of 0.04 and 0.17 for the so-called ZCuOH and Z_2Cu species which reside in the 8 and 6 membered rings (MR) of the zeolitic framework, respectively. Active site concentrations were used in the kinetic models which included simultaneous formation of nitrate/nitrite species or the formation of HNO_3 intermediate which in turn resulted in the formation of nitrates or nitrites over the ZCuOH. Models also included or excluded the NO_2 storage over the so called secondary Z_2Cu sites. It was shown that models taking into account HNO_3 intermediate formation along with two NO_2 storage sites were better fits to the experimental data.

1. INTRODUCTION

Ammonia Selective Catalytic Reduction (NH_3-SCR) is a widely used technology in the aftertreatment systems (ATS) of the lean-burn diesel powered light or heavy-duty vehicles for the abatement of harmful and toxic oxides of nitrogen (NOx). NH_3-SCR reactors usually are monolithic reactors with microchannels wash coated with active catalyst materials where NOx originating from the engine and NH_3 fed using the thermolysis of urea solution sprayed to the reactor undergo SCR reactions. Cu exchanged zeolites especially Cu-chabazites including Cu-SSZ-13 are the catalyst of choice by many original equipment manufacturers (OEMs) for NH_3-SCR process due high deNOx performance in a wide range of temperature and good hydrothermal stability (Gao et al. 2013; Paolucci et al. 2016a).

Over the recent years, there have been significant developments in the kinetic modeling of NH_3-SCR processes for NOx abatement which are usually aimed to be used in the design, calibration and control of SCR units (Bozbag et al. 2020b; Chatterjee et al. 2005; Chatterjee et al. 2007; Daya et al. 2018; Daya et al. 2020a; Dhillon et al. 2019; Gao et al. 2021; Olsson et al. 2015; Selleri et al. 2019; Supriyanto et al. 2015; Usberti et al. 2020). Unlike many industrial reactors, the reactors in the aftertreatment system are continually exposed to highly transient conditions in many cases due to different road conditions, speed and torque generated by the engine. These conditions require the models to be predictive in a variety of conditions for the calibration and control of urea dosage and for the prediction of downstream NOx and NH_3 concentrations. Thus, the underlying SCR mechanisms should be well emulated by the models otherwise cumulative NOx emissions could not be well predicted (Bendrich et al. 2020). Both NO_2 and NH_3 could be stored in Cu-chabazite catalysts at greater quantities and the surface NH_3 and NO_2 related species are important contributors to the catalytic mechanism of NH_3-SCR of NOx according to many authors (Bendrich et al. 2018; Bozbag et al. 2018; Clark et al. 2020; Greenaway et al. 2020; Janssens et al. 2015; Paolucci et al. 2017). Therefore, realistic kinetic modeling of NO_2 and NH_3 adsorption and desorption is crucial to correctly

---

[*] **Corresponding Author**

*(sbozbag@ku.edu.tr) ORCID ID 0000-0003-4471-2301

Cite this article

Bozbağ S E (2022). Single and multisite detailed kinetic models for the adsorption and desorption of NO_2 over Cu based NH_3-SCR catalyst. Turkish Journal of Engineering, 6(3), 230-237

Research Article / DOI: 10.31127/tuje.931038

Received: 01/05/2021; Accepted: 07/09/2021

represent the NH_3-SCR mechanism in order to obtain highly accurate transient NH_3-SCR models. This requires a realistic insight to the concentrations of the active sites on the catalyst for the calculation of total species rates using the mean field approximation where active site concentration normalized rate constants are used (Bozbag et al. 2020a; Daya et al. 2020b). It has been shown that the combined analysis of NH_3-TPD and NO_2-TPD profiles of Cu-chabazites could be used to quantify the concentration of two different Cu species often encountered in Cu-chabazites which are usually referred to as ZCuOH and Z_2Cu which occupy the 8MR and 6MR in the zeolite framework, respectively (Marberger et al. 2018; Paolucci et al. 2016b). Us and others (Bozbag et al. 2020a; Leistner et al. 2017; Luo et al. 2016) had shown that the NH_3-TPD peaks with centers at around 320 and 450°C could be associated with Cu species residing at 6MR and 8MR, respectively. Combined with the known NH_3/Cu stoichiometry (Luo et al. 2017), one can calculate the surface concentrations. According to (Villamaina et al. 2019), NO_2-TPD could be used to titrate the ZCuOH concentrations which could be used as a validation of the surface concentrations obtained from NH_3-TPD. Along this line, different NO_2 adsorption-desorption mechanisms were modeled in the literature (Bendrich et al. 2018; Colombo et al. 2012; Olsson et al. 2009). While some of the models take into account the HNO_3 intermediate formation reactions (Bendrich et al. 2018) some do not (Colombo et al. 2012; Olsson et al. 2009). Moreover, these different NO_2 adsorption-desorption kinetic schemes have not been compared over the same fresh Cu-chabazite catalyst. Therefore, implications of using these different chemical schemes are yet to be discovered. There is also no model in the literature which accounts for multisite adsorption and desorption of NO_2.

For the case of the adsorption of NH_3 over Cu-chabazite, it has recently been suggested that upon adsorption, some Cu species undergo NH_3 solvation within the zeolitic cage and these NH_3 solvated Cu species which are in dynamic mobility might play a role in the SCR mechanism (Paolucci et al. 2017) or may not (Daya et al. 2021). On the other hand, in the literature, the active site values associated with the NH_3 adsorption desorption models is usually done quite arbitrarily and do not generally reflect the true number of active sites associated with adsorption and therefore the rate parameters associated with adsorption are usually lumped parameters. Thus, there is no multi-site kinetic model in the literature where the active site values used in the NH_3 adsorption-desorption model were validated by the NO_2 adsorption-desorption experiments as well.

In this study, a relatively easy method to evaluate different Cu species in Cu-chabazites based on NO_2 and NH_3 adsorption/desorption experiments is proposed and used to develop multisite kinetic models for NH_3 and NO_2 adsorption and desorption. The performance of different kinetic schemes for simulating NO_2 adsorption and desorption were compared to the experimental data obtained using a commercial Cu-chabazite catalyst. The mechanistic implications of using different models were determined.

2. METHOD

2.1. Laboratory tests

The catalysts used in this study were a commercial Cu-chabazite based formulation washcoated to cordierite monolith (400 cpsi – 4 mils). A cylindrical core with a length of 2.2 cm and a diameter of 1.9 cm was used in the runs. The experiments were carried out in a synthetic gas bench (SGB) described in (Bozbag et al. 2020a and 2020b). In a typical run, ceramic fiber paper wrapped monolith was loaded in a quartz reactor and placed in an electric tubular furnace (Thermo Scientific Lindberg Blue M) equipped with a PID controller enabling the desired temperatures or ramps for the experiments. The temperature at reactor inlet was constantly monitored using a J-type thermocouple placed 0.5 cm upstream of the catalyst. NH_3 was purchased from Elite Gaz (10% in He balance), NO_2 was purchased from Hatgaz (10% in N_2 balance), CO_2 and N_2 (5.0) were purchased from Airliquide. All gases were connected to and were fed to the reactor using respective calibrated mass flow controllers (Brooks Instruments) and H_2O was delivered using a peristaltic pump (Gilson Minipuls 3). During the experiments, a general mixture which contained CO_2, H_2O and N_2 passed initially through to a pre-heater after which they were fed to the reactor. NO_2 and NH_3, on the other hand, were fed to general mixture stream just before the reactor using three-way valves connected to inlet via compression fittings to avoid undesired gas phase reactions. All lines before and after the reactor was heated to 190 °C. The species concentrations at the outlet of the reactor were continuously monitored using MKS Multigas 2030 FTIR spectrometer. The catalyst was pre-treated (i.e. degreened) at 550 °C in the presence of 5% H_2O, 8% O_2, in N_2 for 2h at 40000 h^{-1} (NTP). Subsequent to the experiments, the catalyst was exposed to a stream consisting of 8% O_2 in N_2 at 550 °C for 30 min to clean the surface of any N-containing residues. All experiments were carried out at with a space velocity of 40000 h^{-1} (NTP). All the gas grades used were 5.0 or above.

NO_2 adsorption/TPD experiment consists of the adsorption, isothermal desorption, and Temperature Program Desorption (TPD) parts. In a typical experiment, NO_2 was introduced to the reactor (500 ppm NO_2, 5% H_2O, 10% CO_2 in N_2 balance), which evidently resulted in an adsorption breakthrough curve. Once adsorption was completed NO_2 feed was cut off and isothermal desorption of weekly bound NO_2 started during which feed stream contained 5% H_2O, 10% CO_2 in N_2 balance. After desorption of weakly bound NO_2 was completed, temperature ramp was started with a rate of 10 °C/min during which feed stream contained 5% H_2O, 10% CO_2 in N_2 balance as well.. NH_3 adsorption/TPD experiment was carried out in a similar manner. Feed conditions, reactor outlet concentrations and reactor inlet temperatures monitored during each experiment were presented in Section 3. Peak deconvolution was carried out using Fityk version 1.3.1. Gaussian peaks were added manually and then optimized using Nelder-Mead Simplex method.

2.2. Modeling

2.2.1. The reactor model

Modeling was performed using GT-POWER, version 2019 (GT-SUITE Exhaust Aftertreatment Application Manual 2019) using the Fixed Mesh (1+1D) solver and the details were provided elsewhere (Bozbag et al. 2020a). Briefly, mass, energy and momentum balances for the gas and washcoat phases were solved for each contributing gaseous and surface species. Film model was used to incorporate external mass transfer and a washcoat diffusion model was used to consider the effects of internal mass transfer.

2.2.2. Kinetic model

Reaction mechanisms and rate expressions for NO_2 adsorption/desorption (Model A, B, C, D) and NH_3 adsorption/desorption are presented in Table 1. The Arrhenius equation was used in the model to account for the temperature dependency of the turnover rate constant, k_j:

$$k_j = A_j e^{\frac{-E_{A,j}}{RT}} \tag{1}$$

where A_j is the pre-exponential factor and $E_{A,j}$ is the activation energy in reaction j. A coverage dependent activation energy function was used to describe the desorption of NH_3 from Z_2Cu sites (Reaction 11b):

$$E_{A,j} = E_{A,j,0}(1-\alpha\theta_k) \tag{2}$$

In Model A, the NO_2 adsorption and desorption occurred over ZCuOH sites accounting the simultaneous formation of ZCuONO and $ZCuNO_3$ surface species (Reaction 1). Formation of NO upon NO_2 adsorption was modeled using Reaction 2. In Model B, the formation of HNO_3 intermediate was accounted and $ZCuNO_3$ formation is based on reaction of ZCuOH and formed HNO_3 (Reaction 6). Model C is similar to Model A except additional NO_2 storage in terms of surface nitrites and desorption reaction were used over Z_2Cu sites. Model D is similar to Model B except additional NO_2 storage in terms of surface nitrites and desorption reaction were used over Z_2Cu sites. Thermal decomposition of surface nitrates was accounted in all of the models (Reactions 3 and 8). NH_3 adsorption and desorption was modeled using the reactions in Table 1.

The pre-exponential factors and activation energy values of Models A-D were optimized using the experimental data via a Genetic Algorithm to minimize the following error function which is also used to compare model performances:

$$Error = \frac{\left(\sum_{t=0}^{D_{\exp}}(y_{NO,meas}-y_{NO,pred})^2 + \sum_{t=0}^{D_{\exp}}(y_{NO_2,meas}-y_{NO_2,pred})^2\right)\Delta t}{2D_{\exp}} \tag{3}$$

Kinetic parameters for NH_3 adsorption/desorption model were also optimized using a similar function.

Table 1 Reactions and Rate Expressions Used in the Models

Reaction Number	Reaction & Rate Expression
Reactions related to NO2 adsorption/desorption for Model A (Rxn. 1-3) and Model C (Rxn. 1-4))	
1	$2ZCuOH + 2NO_2 \leftrightarrow ZCuONO + ZCuNO_3 + H_2O$ $r_{1f} = k_{1f}C_{NO_2}^2\theta_{ZCuOH}^2$, $r_{1b} = k_{1b}\theta_{ZCuNO_3}\theta_{ZCuONO}$
2	$NO_2 + ZCuONO \leftrightarrow NO + ZCuNO_3$ $r_{2f} = k_{2f}C_{NO_2}\theta_{ZCuONO}$, $r_{2b} = k_{2b}C_{NO}\theta_{ZCuNO_3}$
3	$ZCuNO_3 + 0.5H_2O \rightarrow NO_2 + 0.25O_2 + ZCuOH$ $r_{3f} = k_{3f}\theta_{ZCuNO_3}$
4	$Z_2Cu + NO_2 \leftrightarrow Z_2CuONO$ $r_{4f} = k_{4f}C_{NO_2}\theta_{Z_2Cu}$, $r_{4b} = k_{4b}\theta_{Z_2CuONO}$
Reactions related to NO2 adsorption/desorption for Model B (Rxn. 5-8) and Model D (Rxn. 5-9)	
5	$ZCuOH + 2NO_2 \leftrightarrow ZCuONO + HNO_3$ $r_{5f} = k_{5f}C_{NO_2}^2\theta_{ZCuOH}$, $r_{5b} = k_{5b}C_{HNO_3}\theta_{ZCuONO}$
6	$ZCuOH + HNO_3 \leftrightarrow ZCuNO_3 + H_2O$ $r_{6f} = k_{6f}C_{HNO_3}\theta_{ZCuOH}$, $r_{6b} = k_{6b}\theta_{ZCuNO_3}$
7	$NO_2 + ZCuONO \leftrightarrow NO + ZCuNO_3$ $r_{6f} = k_{6f}C_{NO_2}\theta_{ZCuONO}$, $r_{6b} = k_{6b}C_{NO}\theta_{ZCuNO_3}$
8	$ZCuNO_3 + 0.5H_2O \rightarrow NO_2 + 0.25O_2 + ZCuOH$ $r_{8f} = k_{8f}\theta_{ZCuNO_3}$
9	$Z_2Cu + NO_2 \leftrightarrow Z_2CuONO$ $r_{9f} = k_{9f}C_{NO_2}\theta_{Z_2Cu}$, $r_{9b} = k_{9b}\theta_{Z_2CuONO}$
Reactions related to NH3 adsorption/desorption	
10	$NH_3 + Z_2W \leftrightarrow Z_2WNH_3$ $r_{10f} = k_{10f}C_{NH_3}\theta_{Z_2W}, r_{10b} = k_{10b}\theta_{Z_2WNH_3}$
11	$4NH_3 + Z_2Cu1 \leftrightarrow Z_2Cu1(NH_3)_4$ $r_{11f} = k_{11f}C_{NH_3}\theta_{Z_2Cu1}, r_{11b} = k_{11b}\theta_{Z_2Cu1(NH_3)_4}$
12	$3NH_3 + ZCuOH \leftrightarrow ZCuOH(NH_3)_3$ $r_{12f} = k_{12f}C_{NH_3}\theta_{ZCuOH}, r_{12b} = k_{12b}\theta_{ZCuOH(NH_3)_3}$
13	$NH_3 + ZB \leftrightarrow ZBNH_3$ $r_{13f} = k_{13f}C_{NH_3}\theta_{ZB}, r_{13f} = k_{13b}\theta_{ZBNH_3}$

3. RESULTS AND DISCUSSION

Figure 1 displays the typical TPD of NH_3 (Fig. 3a) and TPD of NO_2 (Fig. 3b) over Cu-chabazite. The NH_3-TPD profile was fitted with 3 Gaussian peaks with peaks centers at 355, 474 and 534 °C which were ascribed to Z_2Cu, ZCuOH and Brönsted sites, respectively. Isothermal desorption of NH_3 observed upon the cutting off of the NH_3 feed was associated with species which bound to NH_3 weakly (hereafter referred to as Z_2W sites). Among these sites W and Cu were assumed to occupy two zeolitic sites whereas CuOH and B sites occupied a single zeolite site. The NH_3 storages associated with Z_2W, Z_2Cu, ZCuOH and Brönsted sites (ZB) were 119.1, 107.6, 34.2 and 9.7 mol/m^3. NO_2-TPD profile was fitted with two Gaussian peaks with peak centers at 302 and 365 °C and with NO_2 storage values of 5.9 and 12.3 mol/m^3, respectively. The peak at the 365 °C was assigned to NO_2 storage at ZCuOH species according to the literature (Villamaina et al. 2019) and the peak at the 302 °C was tentatively assigned to NO_2 storage on Z_2Cu species.

To develop a kinetic model based on realistic active site values, these storage values need to converted to active site concentration values via invoking a stoichiometric reaction between NH_3 or NO_2 and the active sites (Table 2). In the literature, it was shown that the ZCuOH sites could accommodate 3 NH_3 molecules, whereas the Z_2Cu sites could accommodate 4 (Villamaina et al. 2019). This stoichiometry was implemented in the kinetic model developed in this study. The measured NH_3 storage associated with the ZCuOH sites (34.2 mol/m^3) was in excellent agreement with the ZCuOH surface concentrations obtained using the NO_2-TPD which was 12.3 mol/m^3 which is approximately 3 times higher than the NH_3 storage measured for this site in line with the ZCuOH/NH_3 stoichiometry reported in the literature (Luo et al. 2017; Luo et al. 2016; Villamaina et al. 2019). Zeolitic site density occupied by each active site and corresponding fractional coverages were thus calculated based on the stoichiometries given in Table 1 and were presented in Table 2. For example, the fractional coverage of Z_2Cu sites in zeolite was calculated via dividing the NH_3 storage associated with this site by 4 (Reaction 11) followed by multiplication by 2 since 1 Cu site is occupied two zeolite sites. The fractional coverage values given in Table 2 were then used to develop the realistic active site based 4-site kinetic model of the adsorption and desorption of NH_3 over Cu-chabazite. From Table 2, it is clear that the NO_2 storage associated with Z_2Cu sites is low as compared to the fractional coverage of Z_2Cu sites obtained from NH_3-TPD, this indicated that only a small portion of the Z_2Cu sites could accommodate NO_2.

Table 2. Storage values and site density of the active sites

Sites	NO_2 stored[a]	NH_3 stored[a]	Site density[a]	Fractional coverage
Z_2W	0	119.1	238.1	0.76
Z_2Cu	5.9	107.6	53.7	0.17
ZCuOH	12.3	34.2	12.3	0.04
ZB	0	9.7	9.7	0.03

[a]: Units of mol/m^3

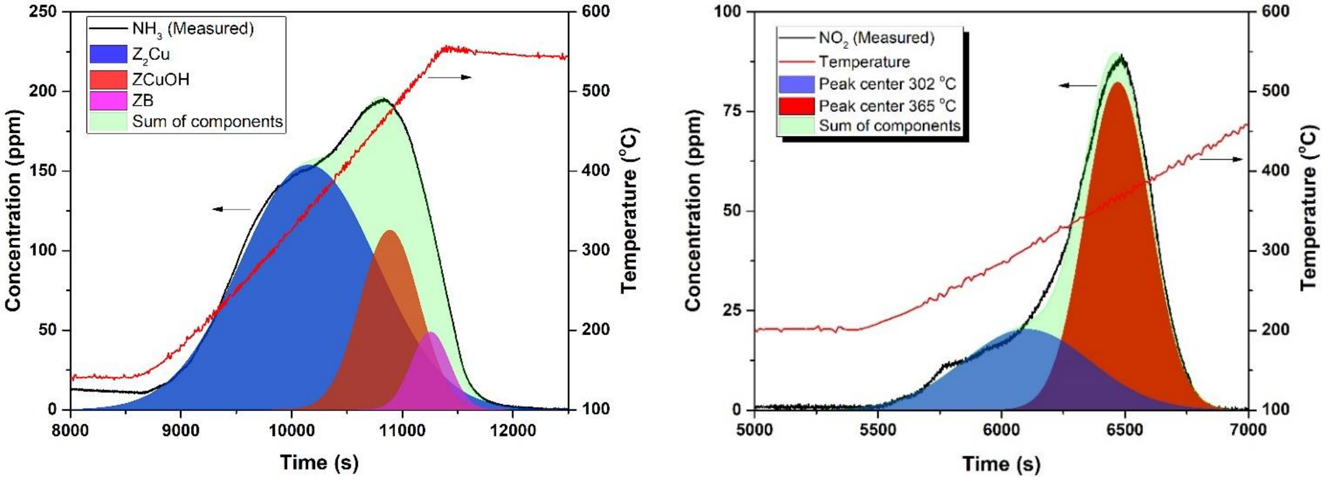

Figure 1. TPD profiles with deconvoluted components (a) NH_3, (b) NO_2.

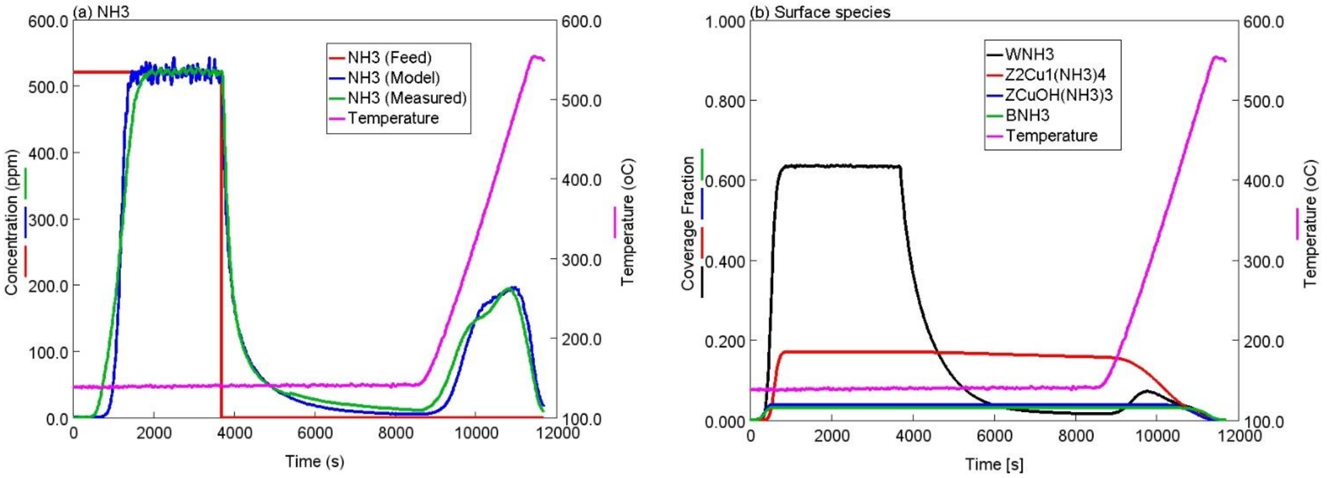

Figure 2. (a) Experimental and predicted NH_3 concentrations during NH_3 adsorption/TPD experiment (b) Simulated fractional coverages for the experiment given in (a).

Measured and modeled NH_3 outlet concentrations during NH_3 adsorption, isothermal desorption and TPD experiment are presented in Figure 2a. Here, upon delivery of the NH_3 feed at t=0 s to the reactor, the experimental data showed NH_3 breakthrough which succeeded the time lag period associated with NH_3 storage over the Cu-chabazite catalyst. Isothermal desorption of NH_3 was observed upon termination of the NH_3 feed at t=3699 s which was followed by the NH_3-TPD phase upon increase of the temperature. TPD profile manifested two main peaks with centers around 350 and 470 ˚C in agreement with previous reports (Leistner et al.

2017). Model (Table 1) showed excellent agreement with the measured data throughout the experiment including the adsorption breakthrough, isothermal desorption and TPD phases. The observed bimodal behavior of the TPD phase was well simulated and the relative intensities of the peaks were also well described by the model.

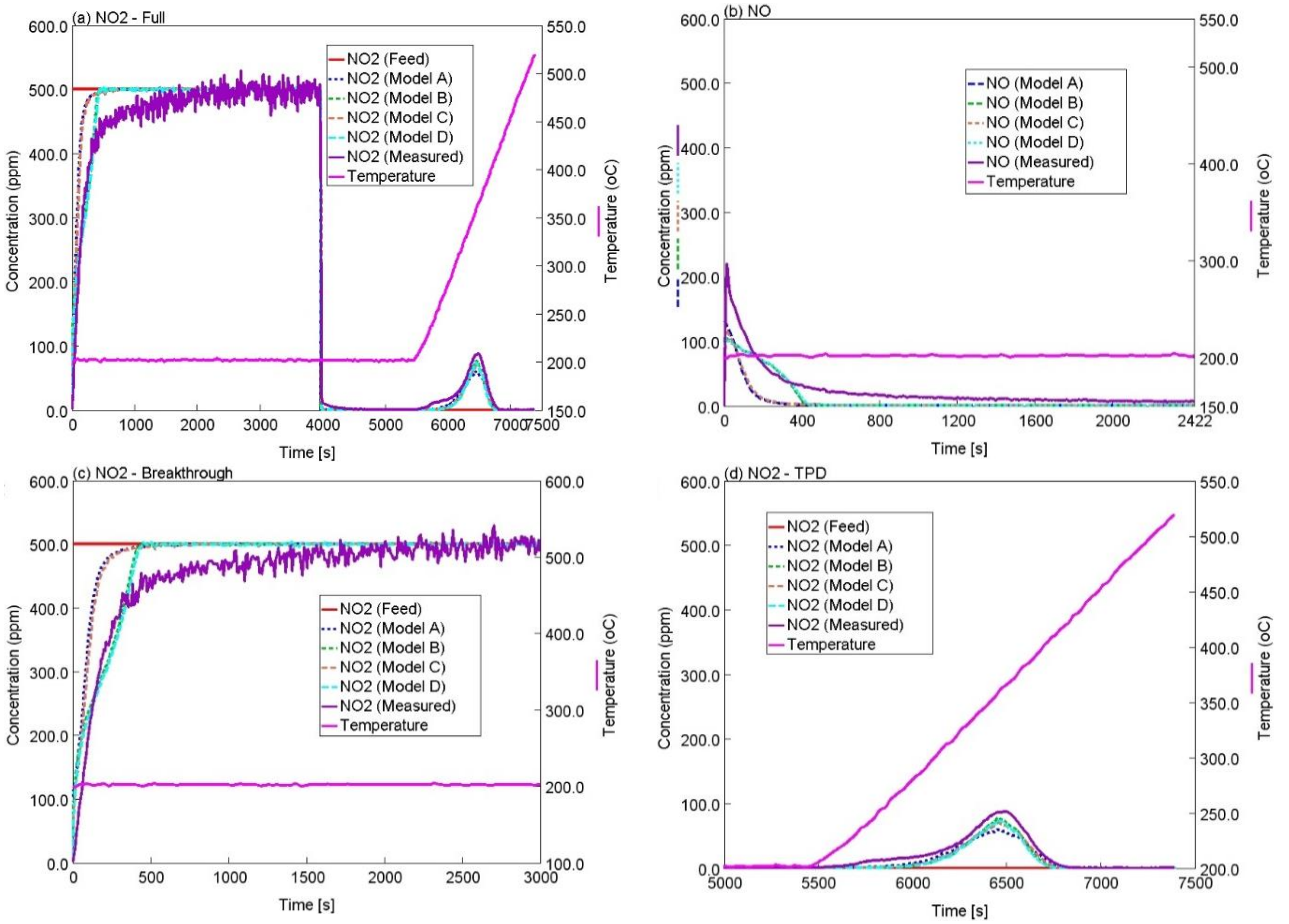

Figure 3. Experimental and predicted effluent concentrations during NO_2 adsorption/TPD experiment (a) NO_2, (b) NO, (c) NO_2 breakthrough region zoomed-up, (d) NO_2-TPD region zoomed-up.

Changes in the fractional coverages of the sites during the NH_3 adsorption and desorption calculated by the model were presented in Figure 2b. All of the NH_3 containing surface species converged to the initial fractional coverage of the corresponding active sites which showed the consistency of the model with measured site densities. Moreover, according to the kinetic model, the temperature centers of the desorption profiles of the $Z_2Cu(NH_3)_4$, $ZCuOH(NH_3)_3$ and $ZBNH_3$ species were in agreement with the deconvoluted temperature centers (355, 474 and 534 °C, respectively) associated with the sites containing the corresponding species obtained from the measured data demonstrating the realistic aspect of the developed kinetic model.

Adsorption and desorption behavior of NO_2 on Cu-chabazite along with its TPD profile is displayed in Figure 3a. NO_2 was fed to the reactor at t=0 which was followed by a slight lag time followed by an adsorption breakthrough which eventually reached the feed concentration which was 500 ppm. The observed lag time is associated with NO_2 stored in the catalyst mostly in terms of nitrates. NO_2 feed was stopped at t= 3969 s, which is followed by the rapid decrease of the NO_2 outlet concentrations as shown in Figure 3a. NO_2 release from the surface was observed in the TPD phase of the experiment. NO_2-TPD profile showed one main peak with temperature center of 363 °C and a shoulder at around 300 °C. The formation of NO is observed upon delivery of NO_2 as shown in Figure 3b. The formation of NO was ascribed to the reaction of NO_2 with ZCuOH sites as kinetically modeled using Reactions 2 and 7 depending on the models. Both NO_2 and NO outlet concentrations were well described by all of the models, however, some models were better than the others. NO_2 breakthrough region is enlarged in Figure 3c which showed Models B and D had better fits as compared to Models A and C. NO_2-TPD region is enlarged in Figure 3d which illustrated that Models B, C and D had similarly well fits to the experimental data whereas the Model A under-predicted NO_2 desorption. Quantitative description of model performances for simulating NO_2 and NO data during this experiment is illustrated in Figure 4 where the value of Eq. 3 for each model is shown. This revealed that the Model B captured the experimental data significantly better than Model A indicating the importance of HNO_3 modeling for NO_2 adsorption/desorption. Additionally, the utilization of second NO_2 storage site (Reactions 4 and 9 in Models C and D, respectively) decreased the error of both Models A and B as shown with the decreased error values of Models C and D, respectively. This indicated that some of the NO_2 was indeed stored on a secondary storage site as this was hinted in NO_2-TPD curve (Fig. 1b) with a shoulder at around 300 °C. Although the storage capacity obtained from NO_2-TPD for Z_2Cu sites was low (which is in agreement with literature which showed that most of NO_2 was stored by the ZCuOH sites), Model C and D resulted in being better fits to experimental data than Models A and B, respectively, indicated that some NO_2 was in fact stored by the Z_2Cu sites at least to some extent. Better fits of Model C and D were due to the incorporation of Reactions 4 and 9 which accounted for additional NO_2 uptake over Cu-chabazite on the Z_2Cu sites.

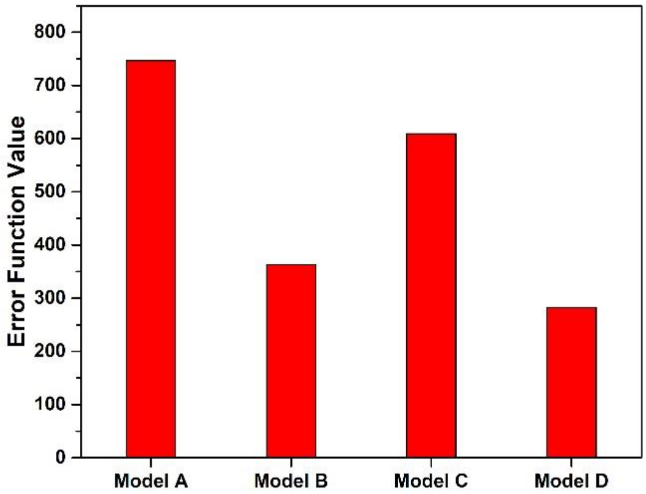

Figure 4. Error function values of different models investigated.

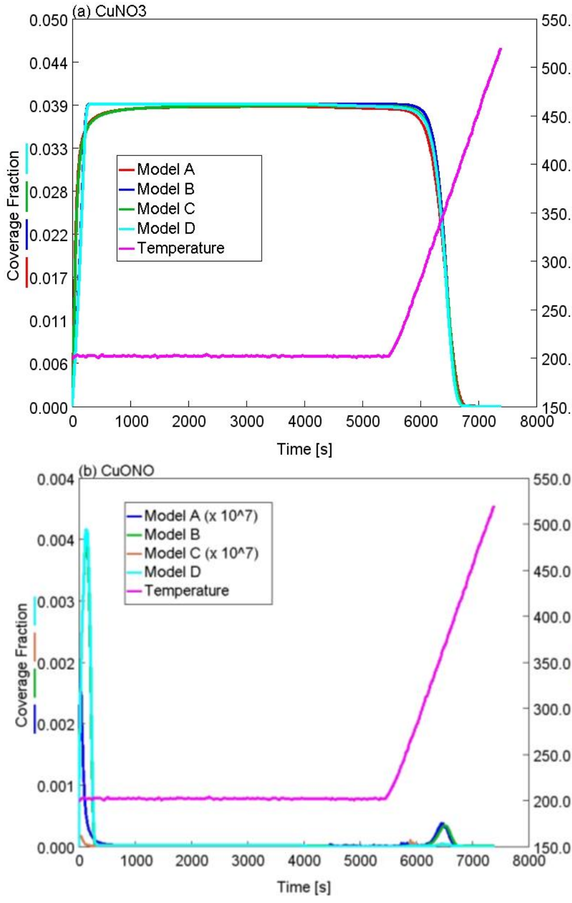

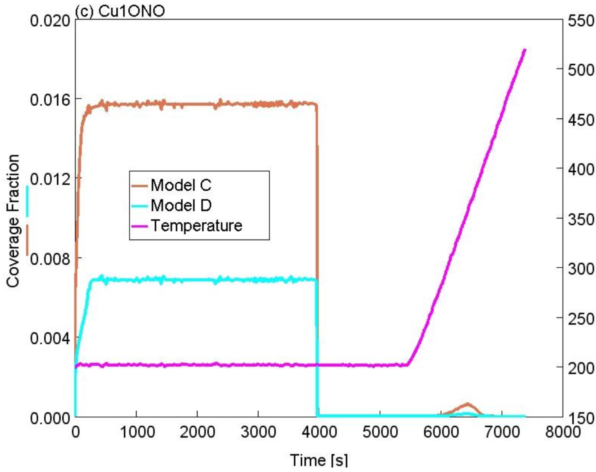

Figure 5. Simulated fractional coverages at the center of the reactor for (a) $ZCuNO_3$, (b) ZCuONO, (c) Z_2CuONO.

The fractional coverages of $ZCuNO_3$ (Figure 5a) and ZCuONO (Figure 5b) at the surface calculated at the center of the reactor showed that the nearly all of the Cu at the surface was in the form of $CuNO_3$ according to Models A and B as the fractional coverage of $ZCuNO_3$ while followed a similar trend to NO_2 breakthrough curve and finally reaching the fractional coverage value of 0.039 which was equal to the initial fractional coverage of ZCuOH. Fractional coverage of the $ZCuNO_3$ species dropped with increase in temperature during the TPD phase of the experiment due to the thermal decomposition (Reaction 3 and 8). Fractional coverage values of CuONO species shown in Figure 5b are very low and suggested that the CuONO species are fast transient intermediates. Calculated fractional coverages of Z_2CuONO are illustrated in Figure 5c which showed lower values as compared those of $ZCuNO_3$ species.

4. CONCLUSION

A method based on a combinatorial use of NH_3-TPD and NO_2-TPD data of Cu-chabazite is proposed to calculate the surface concentrations of ZCuOH and Z_2Cu species. NH_3-TPD calculated concentration of ZCuOH perfectly matched the one obtained from NO_2-TPD. Based on these values, a multisite NH_3 adsorption and desorption model was developed and it described the experimental data in a very successful manner. Moreover, four different NO_2 adsorption/desorption models were developed which included or excluded the HNO_3 intermediate formation and possibility of the NO_2 storage over ZCuOH and Z_2Cu sites. Based on the fits to the experimental data, Model B where HNO_3 intermediate formation is considered showed much lower error function values as compared to Model A where this reaction was not considered indicating a better representation of the experimental data by the Model B. The possibility of Z_2Cu sites for NO_2 storage was also investigated and the models which included the secondary NO_2 storage sites (Models C and D) showed lower error function values as compared to the ones who do not (Models A and B). This pointed out that the importance of modeling of both ZCuOH and Z_2Cu for NO_2 storage which should be taken into account to develop accurate detailed transient kinetic models for NH_3-SCR over Cu-chabazites.

ACKNOWLEDGEMENT

Financial support from Ford Otomotiv San. A.Ş. is gratefully acknowledged.

Conflicts of interest

The authors declare no conflicts of interest.

NOMENCLATURE

A_j	Turnover pre-exponential constant for reaction *j*
C_i	Concentration of species *i* in the gas phase (mol/m^3)
D_{exp}	Simulation duration
$E_{A,j}$	Activation energy for reaction *j* (kJ x mol^{-1})
$E_{A,j,0}$	Activation energy for reaction *j* at zero coverage (kJ x mol^{-1})
k_j	Turnover rate constant for the reaction *j*
r_j	Reaction rate for reaction *j* (mol x s^{-1} x mol$_{site}^{-1}$)
$y_{i,meas}$	Measured molar fraction of species *i* (ppm)
$y_{i,pred}$	Predicted molar fraction of species *i* (ppm)

Greek letters

α	Coverage dependence factor
Δt	Time step
θ_k	Fractional coverage of species k

REFERENCES

Bendrich M, Scheuer A & Votsmeier M (2020). Importance of nitrates in Cu-SCR modelling: A validation study using different driving cycles. *Catalysis Today*. doi: https://doi.org/10.1016/j.cattod.2020.03.015

Bendrich V M, Scheuerb A, Hayesa R E & Votsmeierb M (2018). Unified mechanistic model for Standard SCR, Fast SCR, and NO2 SCR over a copper chabazite catalyst. *Applied Catalysis B: Environmental, 222* 76–87.

Bozbag S E, Şanlı D, Özener B, Hisar G & Erkey C (2020a). An Aging Model of NH3 Storage Sites for Predicting Kinetics of NH3 Adsorption, Desorption and Oxidation over Hydrothermally Aged Cu-Chabazite. *Catalysts, 10*, 411.

Bozbag S E, Şimşek M, Demir O, Şanlı D, Ozener B, Hisar G & Erkey C (2020b). Assessment of the Single-Site Kinetic Model for NH3-SCR on Cu-Chabazite for the Prediction of NOx Emissions in Dynamometer Tests. *Emission Control Science and Technology, 6*, 1.

Bozbag S E, Simsek M, Demir O, Sanli Yildiz D, Ozener H B., Hisar, G., & Erkey, C. (2018). Experimental and theoretical study of NH3 adsorption and desorption over a Cu-chabazite NH3-SCR catalyst. *Turkish Journal of Chemistry, 42*, 1768 – 1780.

Chatterjee D, Burkhardt T, Bandl-Konrad B, Braun T, Tronconi E, Nova I & Ciardelli C (2005). Numerical Simulation of Ammonia SCR-Catalytic Converters: Model Development and Application. *SAE Technical Paper Series, 2005-01-965*.

Chatterjee D, Burkhardt T, Weibel M, Nova I, Grossale A & Tronconi E (2007). Numerical Simulation of Zeolite- and V-Based SCR Catalytic Converters. *SAE Technical Paper Series, 2007-01-1136*.

Clark A H, Nuguid R J G, Steiger P, Marberger A, Petrov A W, Ferri D, . . . Kröcher O (2020). Selective Catalytic Reduction of NO with NH3 on Cu–SSZ-13: Deciphering the Low and High-temperature Rate-limiting Steps by Transient XAS Experiments. *Chemcatchem, 12*(5), 1429-1435. doi:10.1002/cctc.201901916

Colombo M, Nova I & Tronconi E (2012). Detailed kinetic modeling of the NH3-NO/NO2 SCR reactions over a commercial Cu-zeolite catalyst for Diesel exhausts after treatment. *Catalysis Today, 197*(1), 243-255. doi:10.1016/j.cattod.2012.09.002

Daya R, Desai C & Vernham B (2018). Development and Validation of a Two-Site Kinetic Model for NH3-SCR over Cu-SSZ-13—Part 2: Full-Scale Model Validation, ASC Model Development, and SCR-ASC Model Application. *Emission Control Science and Technology, 4*, 172–197.

Daya R, Joshi S Y, Dadi R K, Tang Y, Trandal D, Srinivasan A, . . . Cunningham M (2020a). An explicit reduced-order model of Cu-Zeolite SCR catalyst for embedding in ECM. *Chemical Engineering Journal*, 127473. doi: https://doi.org/10.1016/j.cej.2020.127473

Daya R, Joshi S Y, Luo J, Dadi R K, Currier N W & Yezerets A (2020b). On kinetic modeling of change in active sites upon hydrothermal aging of Cu-SSZ-13. *Applied Catalysis B: Environmental, 263*, 118368. doi: https://doi.org/10.1016/j.apcatb.2019.118368

Daya R, Keturakis C J, Trandal D, Kumar A, Joshi S Y & Yezerets A (2021). Alternate pathway for standard SCR on Cu-zeolites with gas-phase ammonia. *Reaction Chemistry & Engineering*. doi:10.1039/D1RE00041A

Dhillon P S, Harold M P, Wang D, Kumar A & Joshi S Y (2019). Modeling and analysis of transport and reaction in washcoated monoliths: Cu-SSZ-13 SCR and dual-layer Cu-SSZ-13 + Pt/Al2O3 ASC. *Reaction Chemistry & Engineering, 4*(6), 1103-1115. doi:10.1039/C8RE00325D

Gao F, Kwak J H, Szanyi J & Peden C H F (2013). Current Understanding of Cu-Exchanged Chabazite Molecular Sieves for Use as Commercial Diesel Engine DeNO(x) Catalysts. *Topics in Catalysis, 56*(15-17), 1441-1459. doi:10.1007/s11244-013-0145-8

Gao Z, Pihl J, LaClair T & Fricke B (2021). Global kinetic modeling of NH3-SCR with two sites of NH3 storage on Cu-SSZ-13. *Chemical Engineering Journal, 406*, 127120. doi: https://doi.org/10.1016/j.cej.2020.127120

Greenaway A G, Marberger A, Thetford A, Lezcano-González I, Agote-Arán M, Nachtegaal M, . . . Beale A M (2020). Detection of key transient Cu intermediates in SSZ-13 during NH3-SCR deNOx by modulation excitation IR spectroscopy. *Chemical Science, 11*(2), 447-455. doi:10.1039/C9SC04905C

GT-SUITE Exhaust Aftertreatment Application Manual. (2019). Gamma Technologies LLC.

Janssens T V W, Falsig H, Lundegaard L F, Vennestrom P N R, Rasmussen S B, Moses P G, . . . Beato P (2015). A Consistent Reaction Scheme for the Selective Catalytic Reduction of Nitrogen Oxides with Ammonia. *ACS Catalysis, 5*(5), 2832-2845. doi:10.1021/cs501673g

Leistner K, Xie K, Kumar A, Kamasamudram K & Olsson L (2017). Ammonia Desorption Peaks Can Be Assigned to Different Copper Sites in Cu/SSZ-13. *Catalysis Letters, 147*(8), 1882-1890. doi:10.1007/s10562-017-2083-8

Luo J, Gao F, Kamasamudram K, Currier N, Peden C H F & Yezerets A (2017). New insights into Cu/SSZ-13 SCR catalyst acidity. Part I: Nature of acidic sites probed by NH3 titration. *Journal of Catalysis, 348*, 291-299. doi: https://doi.org/10.1016/j.jcat.2017.02.025

Luo J, Wang D, Kumar A, Li J, Kamasamudram K, Currier N & Yezerets A (2016). Identification of two types of Cu sites in Cu/SSZ-13 and their unique responses to hydrothermal aging and sulfur poisoning. *Catalysis Today, 267*, 3-9. doi: https://doi.org/10.1016/j.cattod.2015.12.002

Marberger A, Petrov A W, Steiger P, Elsener M, Kröcher O, Nachtegaal M & Ferri D (2018). Time-resolved copper speciation during selective catalytic reduction of NO on Cu-SSZ-13. *Nature Catalysis, 1*(3), 221-227. doi:10.1038/s41929-018-0032-6

Olsson L, Sjovall H & Blint R J (2009). Detailed kinetic modeling of NOx adsorption and NO oxidation over Cu-ZSM-5. *Applied Catalysis B-Environmental, 87*(3-4), 200-210. doi:10.1016/j.apcatb.2008.09.007

Olsson L, Wijayanti K, Leistner K, Kumar A, Joshi S Y, Kamasamudram K, . . . Yezerets A (2015). A multi-site kinetic model for NH3-SCR over Cu/SSZ-13. *Applied Catalysis B-Environmental, 174*, 212-224. doi:10.1016/j.apcatb.2015.02.037

Paolucci C, Di Iorio J R, Ribeiro F H, Gounder R & Schneider W F (2016a). Chapter One - Catalysis Science of NOx Selective Catalytic Reduction With Ammonia Over Cu-SSZ-13 and Cu-SAPO-34. In C. Song (Ed.), *Advances in Catalysis* (Vol. 59, pp. 1-107): Academic Press.

Paolucci C, Khurana I, Parekh A A, Li S, Shih A J, Li H, . . . Gounder R (2017). Dynamic multinuclear sites formed by mobilized copper ions in NOx selective catalytic reduction. *Science, 357*(6354), 898-903. doi:10.1126/science.aan5630

Paolucci C, Parekh A A, Khurana I, Di Iorio J R, Li H, Albarracin Caballero J D, . . . Schneider W F (2016b). Catalysis in a Cage: Condition-Dependent Speciation and Dynamics of Exchanged Cu Cations in SSZ-13 Zeolites. *J. Am. Chem. Soc., 138*(18), 6028-6048. doi:10.1021/jacs.6b02651

Selleri T, Nova I & Tronconi E (2019). An efficient reduced model of NH3-SCR converters for mobile aftertreatment systems. *Chemical Engineering Journal, 377*, 120053. doi:https://doi.org/10.1016/j.cej.2018.09.214

Supriyanto Wijayanti K, Kumar A, Joshi S, Kamasamudram K, Currier N W, . . . Olsson L (2015). Global kinetic modeling of hydrothermal aging of NH3-SCR over Cu-zeolites. *Applied Catalysis B-Environmental, 163*, 382-392. doi:10.1016/j.apcatb.2014.07.059

Usberti N, Gramigni F, Nasello N D, Iacobone U, Selleri T, Hu W, . . . Tronconi E (2020). An experimental and modelling study of the reactivity of adsorbed NH3 in the low temperature NH3-SCR reduction half-cycle over a Cu-CHA catalyst. *Applied Catalysis B: Environmental, 279*, 119397. doi:https://doi.org/10.1016/j.apcatb.2020.119397

Villamaina R, Liu S, Nova I, Tronconi E, Ruggeri M P, Collier J, . . . Thompsett D (2019). Speciation of Cu Cations in Cu-CHA Catalysts for NH3-SCR: Effects of SiO2/AlO3 Ratio and Cu-Loading Investigated by Transient Response Methods. *ACS Catalysis, 9*(10), 8916-8927. doi:10.1021/acscatal.9b02578

Turkish Journal of Engineering
https://dergipark.org.tr/en/pub/tuje
e-ISSN 2587-1366

A low-cost smart home automation for elderly who has Alzheimer's or age-related memory loss

Ayse Nur Ay*[1], **Baris Cokacar** [1], **Ibrahim Turkmen** [1]

[1]*Sakarya University of Applied Sciences, Mechatronics Engineering Department, Sakarya, Turkey.*

Keywords
Smart home
Automation
LabVIEW
Arduino

ABSTRACT

Technology, which is developing considerable in recent years, have influence on automation systems as well. With the advancement of the technology, people want to remote access systems and artificial intelligent systems that can consider for them. Nowadays, people started to tend smart house systems in order to facilitate their lives and to live more peaceful. In this study, a smart house automation system was designed on LabVIEW platform for people who has age-related memory loss or Alzheimer's or who cannot fulfill their needs. The house performs some functions namely, medication reminder, pulse-control sensor, temperature control and fire alarm, door/window warning system, burglar alarm, and lighting systems. This study is based on, communication via e-mail. If there is any abnormality in the house, the system allows users to have an e-mail about the current situation. Since, the study targets elderly or people who needs medical care, this low-cost design can be very preferable in the future.

1. INTRODUCTION

In 1980, "Smart house" was used as a new concept for the first time. This detail was regarded as historical development of smart houses. In 1984, the first smart house was made in Turkey. The main idea behind this house was just to give a comfortable life style to ordinary people. However later on, many commercial options controlled by individuals were presented.

The house automation systems were continued to be improved in 90's as well. In 1993, Christos Douligeris presented the intelligent home systems. These systems enabled the user to communicate with the system via voice or visual communications. He also divided the house automation products into three categories: interactive smart products, intelligent subsystems, and central home automation systems (Douligeris, 1993).

In 1995, Baki Koyuncu suggested home automation system using phone wires and a PC (Koyuncu, 1995).

In 1998, remote control system carried out by Coskun and Ardam which was considered as a milestone for smart house technologies. Their system included a phone-based remote controller which can detect the user number in order to prevent unknown users for control unit (Coskun & Ardam, 1998).

With the developed technology, the home automation systems began to be more affordable option for people in early 2000s.

Aldrich defined a smart home as the house which is equipped with computing and information technologies and enable security and entertainment to the users via control systems (Aldrich, 2003). The smart houses have been defined as the house which facilitates many technological features that make people life easier. Nowadays, in many studies, different terms were used instead of "smart house" such as smart construction, construction automation system, integrated house and smart building systems. Based on these terms, a smart house can be defined as the house which increases life standards of residents through computer and communication technologies (Mennicken et al. 2014).

Many studies direct their focus on designing smart home automation systems using microcontrollers (Bhardwaj et al. 2015). Soliman et al. designed a real-

---

* **Corresponding Author**

*(ay@subu.edu.tr) ORCID ID 0000-0002-4448-4858
(g160918026@subu.edu.tr) ORCID ID 0000-0002-1752-7832
(g150918023@subu.edu.tr) ORCID ID 0000-0003-4970-1337

Cite this article

Ay A N, Cokacar B & Turkmen I (2022). A low-cost smart home automation for elderly who has Alzheimer's or age-related memory loss. Turkish Journal of Engineering, 6(3), 238-244

Research Article / DOI: 10.31127/tuje.942823

Received: 25/05/2021; Accepted: 18/10/2021

time automation system using arduino and LabVIEW. Their system included temperature management, light energy saving and security camera (Soliman et al. 2017). Zaro et al., 2021 confirmed and extended previous arduino based studies by implementing Wi- Fi connection to the system which enabled users to access to control and monitor the system from anywhere in the house. Even though these developments were remarkable for home automation systems, in case of elderly users who needs medical care, the functions of the systems must be advanced.

With the increase of elderly population in all around the world, a lot of research direct their focus to provide a smart home that can lead them to a better life quality (Pal et al. 2017). With the priority of these people security, the smart systems have been continued to be developed. Particularly, with the necessity of health-monitoring and independent assisted living, smart houses became more preferable for elderly or people who need healthcare especially who have Alzheimer or age-related memory lost. As known, Alzheimer is the most common form of dementia and caring people with Alzheimer is a very challenging task for their family members. Brunete et al. presented that smart-homes can help with Alzheimer's in daily tasks fields and security (Brunete González, et al. 2017). Technological solutions and intelligent assistive technologies for elderly with Alzheimer's were continued to be developed (Ienca et al. 2017; Maresova et al. 2018). Since people with Alzheimer's or who has age-related memory loss may live alone in the house, remote monitoring technologies became more important for automation systems (Muurling et al. 2021).

In this study, a smart house system which targeted especially people who have Alzheimer or age-related memory loss was designed using Arduino microcontroller and LabVIEW platform. According to their needs, different functions have been applied to the system.

2. MATERIALS AND METHOD

In this study, LabVIEW, Arduino UNO R3, Arduino 2 Channel Relay Module, DC6 12V Mini Water Pump, LM335-Z Temperature Sensor, Pulse-Heart Rhythm Sensor, Arduino Motion Sensor, Leds, Fan and 12 V adaptor have been operated. The block diagram of the study is given in Figure 1.

Firstly, these six functions that utilized the automation in the house were set and the circuits were designed on LabVIEW step by step. These functions are namely, medication reminder, pulse-control sensor, temperature control, fire alarm, door/window warning system, burglar alarm, and lighting systems.

All inputs and outputs were available through Arduino communication. Serial communication was used as a communication technique between LabVIEW and arduino. Makerhub serial communication software, which is an add-on of LabVIEW, was downloaded via NI VISA. In this add-on, the arduino, which is connected to the computer with the Com port, was introduced to the LabVIEW. Afterwards, the sensors were connected to the arduino and the data was read through analog and digital data reading methods via LabVIEW.

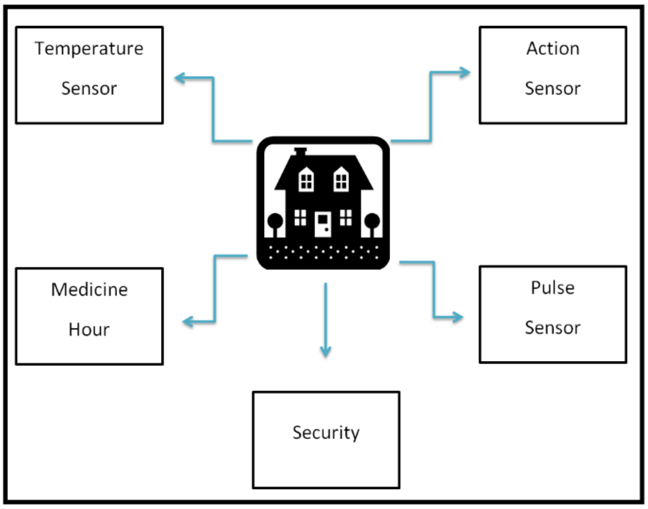

Figure 1. The block diagram of the study.

Digital filters were used for prepocessing of the signals. For example, for the pulse sensor, a band-pass and a band-stop filter were used. The band-pass filter was used to get signals in a certain frequency range in which ECGs can be recognised easily (0,1 -120 Hz) (Ay et al. 2017).

The band-stop filter, which reduces frequencies in a certain range to very low levels, was used to eliminate 50Hz powerline interference.

2.1. Medication Reminder

A medication reminder is one of the most important functions of this study. This application was designed in order to remind a person his/her medical requirements. This option is very useful especially elder people who is suffering from age-related memory loss or Alzheimer.

Working principle of the application was designed over LabVIEW and communication between the app and the user is provided through Wi-Fi and e-mail. Figure 2 represents the LabVIEW block diagram of the medication reminder application.

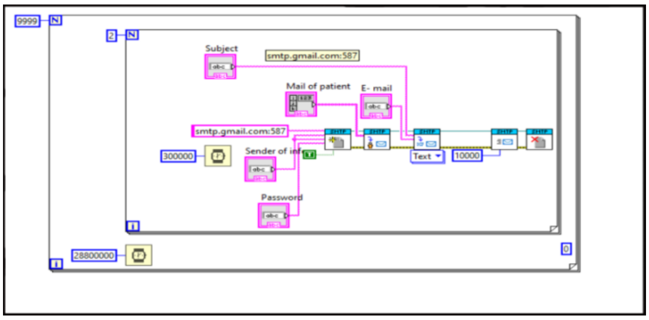

Figure 2. LabVIEW block diagram of the medication reminder.

The front panel of LabVIEW which enables the reminder algorithm to be compiled which can be seen in Figure 3.

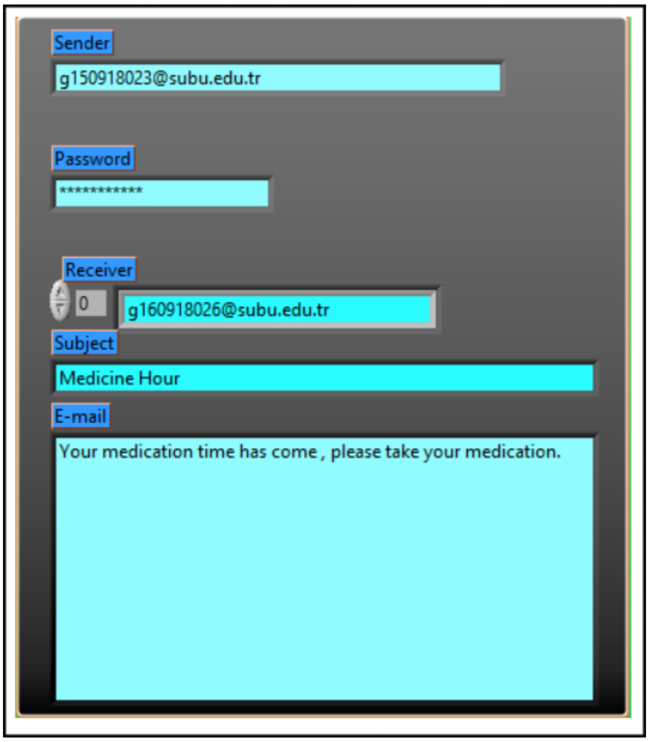

Sender
g150918023@subu.edu.tr

Password
****

Receiver
0
g160918026@subu.edu.tr

Subject
Medicine Hour

E-mail
Your medication time has come , please take your medication.

Figure 3. The front panel of LabVIEW for medication reminder.

2.2. Pulse Control Sensor

The pulse rate sensor that was used for this study can be connected to Arduino. This sensor, measures the pulse by fixing it to fingertip. Thanks to the noise canceling circuit on it, a stable measurement can be taken. Supply voltage of this sensor was 3-5 Volts. When the user puts his/her finger on the pulse rate sensor, the values detected from the sensor can be recorded with analog data reading method through arduino via LabVIEW.

In this application, the object was that pulse rate of an individual was taken instantaneously so health problems of a patient could easily be diagnosed and solved under doctor control. In order to diagnose and solve these problems, the application saved instant pulse rates on a .txt file and made an emergency call to units if pulse rate of a patient was at critical level. A sample txt. file is displayed in the figure below.

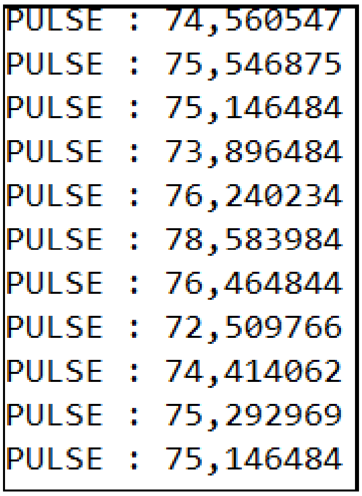

```
PULSE : 74,560547
PULSE : 75,546875
PULSE : 75,146484
PULSE : 73,896484
PULSE : 76,240234
PULSE : 78,583984
PULSE : 76,464844
PULSE : 72,509766
PULSE : 74,414062
PULSE : 75,292969
PULSE : 75,146484
```

Figure 4. A sample txt. file for recording pulse rates.

The application was written on LabVIEW and was imported as analog data from Arduino Pulse heart - Rhythm sensor. Communication was provided through Wi-Fi via an e-mail.

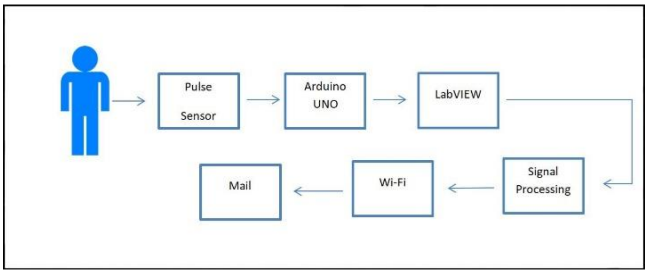

Figure 5. The block diagram of the pulse sensor usage

The block diagram of the heart rate calculation in LabVIEW is presented in Figure 6.

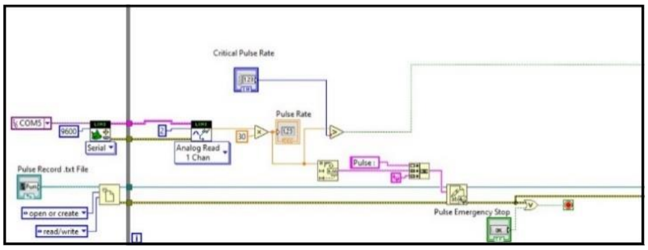

Figure 6. Block diagram of heart rate calculation.

The program was designed as user friendly. A critical pulse rate was added to the panel. Therefore, the value can be adjusted according to user's age or medical condition. Figure 7 represents the front panel of heart rate calculation program.

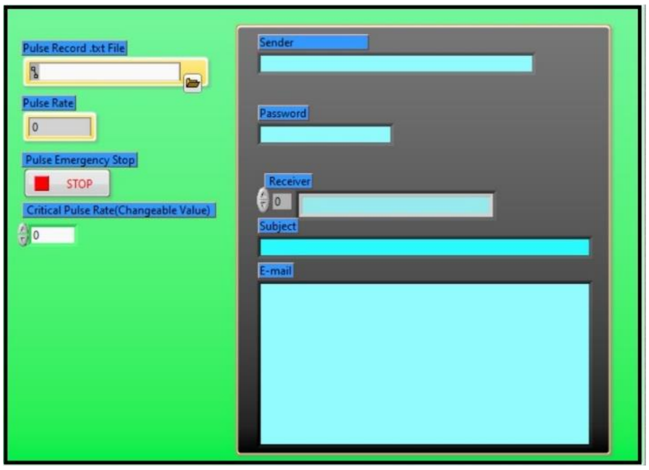

Pulse Record .txt File

Pulse Rate
0

Pulse Emergency Stop
STOP

Critical Pulse Rate(Changeable Value)
0

Sender

Password

Receiver
0

Subject

E-mail

Figure 7. Front panel of heart rate calculation program on LabVIEW.

2.3. Temperature Sensor and Fire Alarm

This application was designed in order to control temperature of a home and provide life safety. Working principal of the application was that necessary parts of automation turns on according to temperature rates which was taken from thermocouple through analog. For instance, when temperature is below 25°C, it is stated that environment is cold, when temperature is 26°C – 33°C, it is also stated that temperature of environment is normal. Between 33°C and 40°C Temperature value range it is stated that environment is hot and fan turns on by means of digital data reading. When temperature is above 40°C, the fire alarm starts and gives emergency call to require units via Wi-Fi and fire extinguish system turns on by means of digital data reading. In order to adjust the limit temperature degree, a critical value option was added to the panel.

The block diagram of working principle of the temperature sensor is displayed in Figure 8.

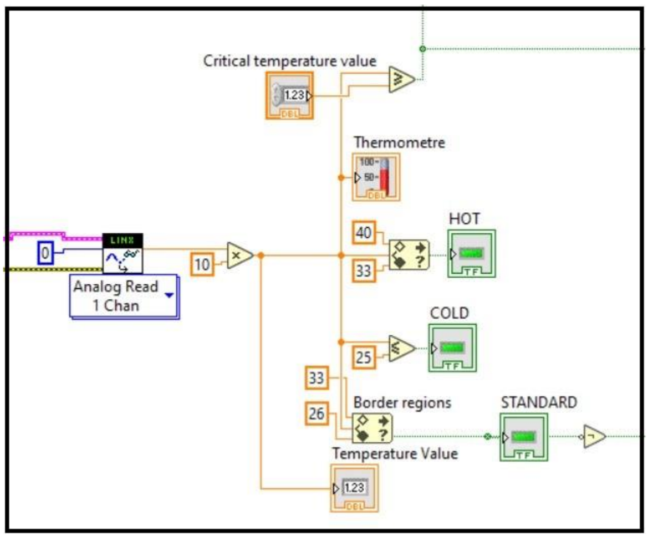

Figure 8. The block diagram of working principle of temperature sensor.

LM335 Temperature Sensor Integration can measure the temperature of the environment thanks to the temperature sensor circuit in it. This Temperature Sensor gives output between 2.95V - 3.01V. Reverse current is 15mA forward current is 10mA. It can measure between -40 °C and 100 °C temperatures. The front panel of temperature sensor is shown in Figure 9.

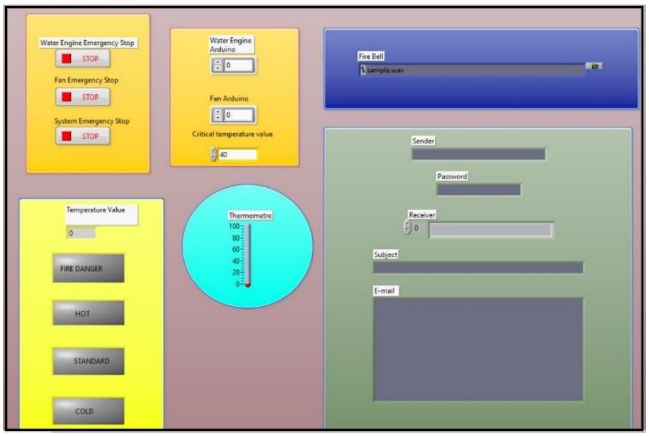

Figure 9. The front panel of the temperature sensor

According to this program, when the temperature value shows over 33 °C, communication from Arduino is provided, the inverted relay is activated and operates the fan to cool the house. The block diagram of fan control is displayed in Figure 10.

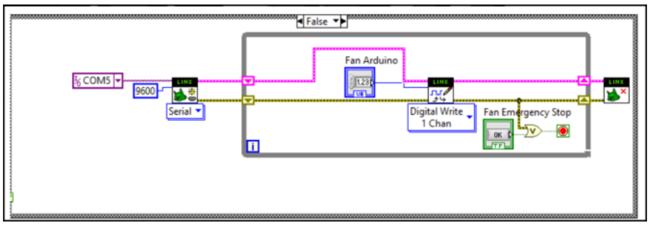

Figure 10. The block diagram of the fan control.

2.4. Door Window Warning System

This application was designed in order to provide safety cautions of a person and the application sends e-mail via Wi-Fi in order that the person close the door and the windows. The algorithm behind this function has the same working principle with the medication reminder function.

2.5. Burglar Alarm

This application was designed in order to take precaution towards the hazards which comes from outside. Working principal is shown on LabVIEW by being imported 1 / 0 data from motion sensor via data reading. Burglar alarm turns on and gives an emergency call to required units when it perceive an activity. The block diagram of the burglar alarm system is displayed in Figure 11.

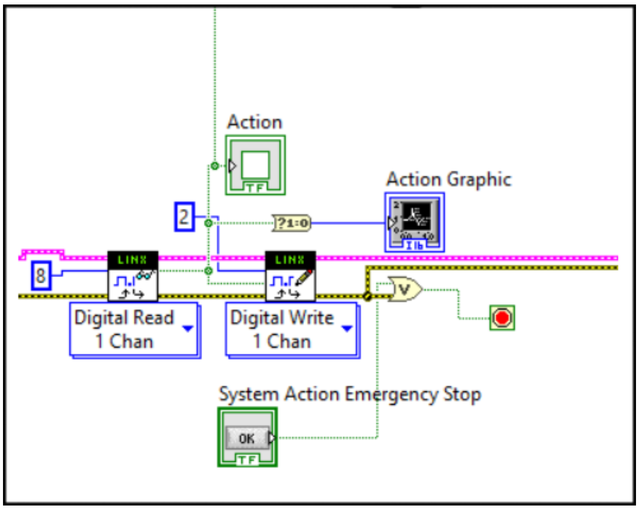

Figure 11. Burglar alarm block diagram

According to the burglar alarm algorithm, when the motion sensor detects a motion, it can be seen on the front panel of the program with the help of the green light. When the signal is received, the alarm sound starts with the help of LabVIEW. The front panel of burglar alarm algorithm is shown in Figure 12.

The algorithm behind burglar alarm function has the same working principle with the temperature control function.

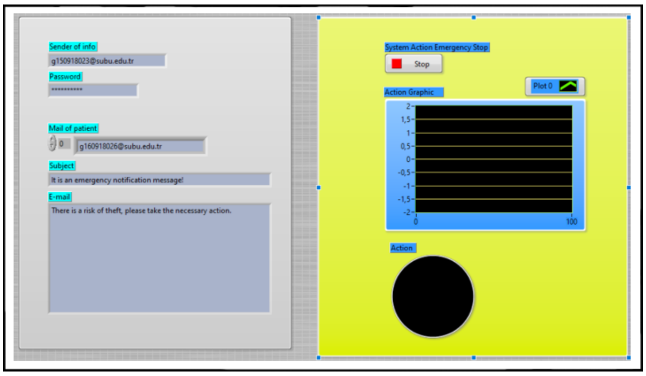

Sender of info
g150918023@subu.edu.tr
Password
****
Mail of patient
0 g160918026@subu.edu.tr
Subject
It is an emergency notification message!
E-mail
There is a risk of theft, please take the necessary action.

Figure 12. Burglar alarm front panel

2.6. Lighting System

3 led light were set up in order to enlighten the smart house. It was connected through Arduino and 1 and 0 control was made over LabVIEW. The logic behind lighting system is simply displayed in figure 13.

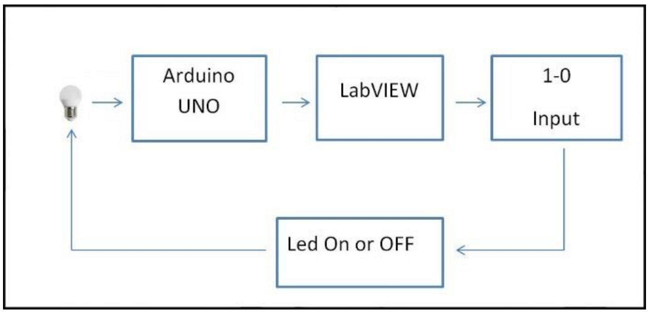

Figure 13. Block diagram of lighting system

Figure 14 and 15 represents the algorithm and user interface of the lighting system.

In this designed smart house, more comfortable life was tried to be provided to elderly especially who has age-related memory loss or Alzheimer's. Besides, the system keeps the security forefront.

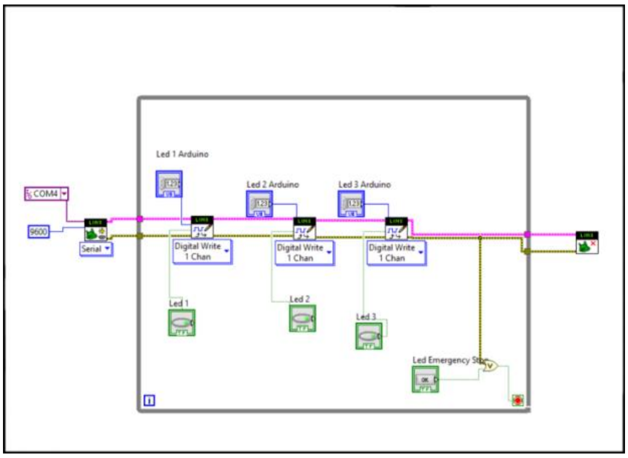

Figure 14. LabVIEW Block diagram of lighting rear panel

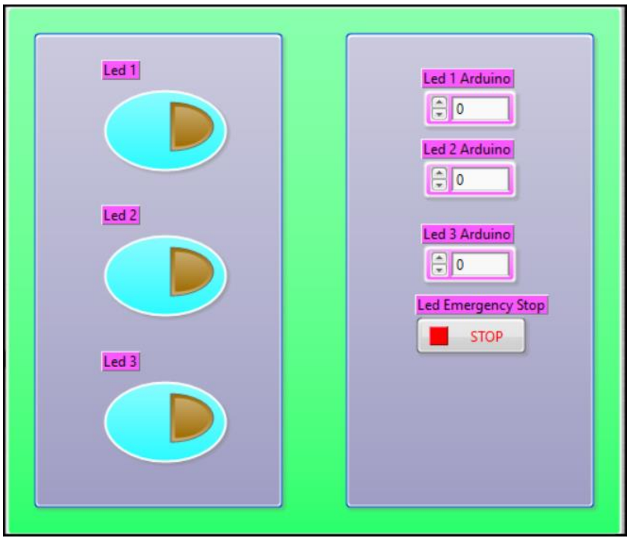

Figure 15. The front panel of lighting system.

3. RESULTS AND DISCUSSION

In this study, smart house automation design in LabVIEW platform was carried out in order to increase life standards of elderly or healthcare needed people and facilitate lives of people who needs assistance. For that purpose, six different functions were applied to the automation system. As it was detailed in the materials and methods sections, all functions were compiled successfully on LabVIEW.

The performance criteria and limitations of this study are taken as reference according to the values of a healthy and young person. However, these values can be easily changed by user from the block diagram of the LabVIEW program. For example, ideal temperature level can be optimized by a user. Therefore, the results of the simulations were determined according to user preferences.

A sample e-mail result that is set for reminding medication hour is displayed in Figure 16.

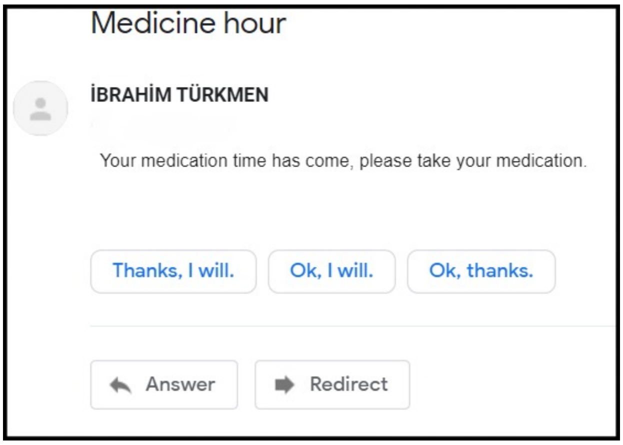

Medicine hour

İBRAHİM TÜRKMEN

Your medication time has come, please take your medication.

Figure 16. A sample e-mail for medication reminder.

A sample e-mail result that is set for pulse-rate alarm is displayed in Figure 17.


It is an emergency message!

İBRAHİM TÜRKMEN <g150918023@subu.edu.tr>

The patient's pulse condition is critical, please take the necessary action.

Figure 17. A sample pulse-rate alarm e-mail.

A sample e-mail result that is set for fire alarm is presented in Figure 18.


It is an emergency message!

İBRAHİM TÜRKMEN <g150918023@subu.edu.tr>

There is a fire, please take the necessary action.

Figure 18. A sample Fire alarm e-mail.

A sample e-mail result that is set for burglar alarm is presented in Figure 19.

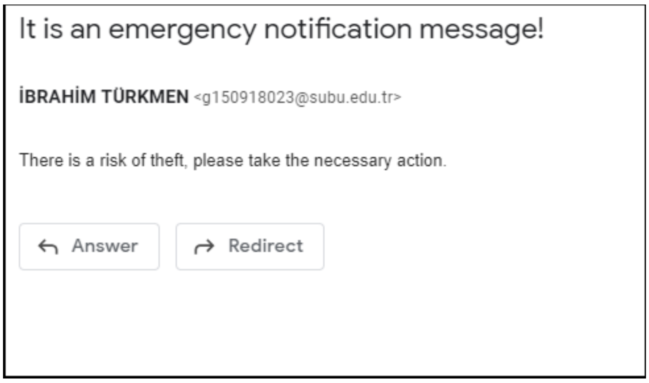
It is an emergency notification message!

İBRAHİM TÜRKMEN <g150918023@subu.edu.tr>

There is a risk of theft, please take the necessary action.

Figure 19. A sample burglar alarm e-mail.

As known, smart houses generally designed to lower the social isolation or loneliness among elder people. Besides, some studies showed that these smart houses reduced fear or anxiety (Lauriks et al., 2007).

In fact, these smart automation systems help people who tend to forget daily tasks such as taking medicines (Cahill et al. 2007).

In this present design, the automation was designed as a companion for Alzheimer patients and those who needs assistance. As well, it became a first aid system which can request first aid with emergency call and compensate security weaknesses. Besides, unlike the commercial smart house automation, this low-cost design can be affordable by more people (Fernandes et al. 2014).

In recent years Internet of Things (IoT) has considered as new technology that aims to help people in their lives. This technology is generally used SCADA based home automation studies (Niranjan et al. 2017). Due to the pandemic situation, these IoT devices become more preferable especially for Alzheimer's (Oskouei et al. 2020). Since this present study confirm and extend the previous studies, we believe this LabVIEW based study will provide new functionalities in smart automation systems especially for elderly.

As known, the quality of life can depend on not only to health but also various factors such as social companionship and entertainment (Pal & Triyason, 2017). Even though our study was focused on limited requirements of people, this low-cost design can be improved with many different functions so that it can be preferable for many people.

4. CONCLUSION

In this present work, firstly, literature research was carried out for house automation system and an application was designed on LabVIEW. Therefore, the conceptual designing stages were performed. Consequently, hardware defines of the project carried out completely, required materials were analyzed, those which were suitable were chosen and the automation software was written on LabVIEW.

While the materials of the project were being determined, Alzheimer patients was prioritized and taken into consideration.

After automation carried out, most suitable materials which can establish communication was reviewed. In addition, materials which will be required if the project is actualized was determined accurately, systems in the design was completed definitely. Moreover, a program that users can make personal adjustments was set up.

In this study, it was served the purpose of facilitating of Alzheimer patients' lives. Arduino, fire extinguish system, motion sensor, pulse sensor and temperature sensor was used in the application. Communication of Arduino and sensors was successfully carried out. In the project, which was done in order that residents feel happy and safe him/herself, it was avoided to make resident lazy and tried to remove negative sides of the project.

Author contributions

Ayşe Nur Ay: Conceptualization, Investigation, Writing-Reviewing and Editing **Barış Çokacar:** Methodology, Writing-Original draft preparation, application **İbrahim Türkmen:** Methodology, Writing-Original draft preparation, simulation.

Conflicts of interest

The authors declare no conflicts of interest.

REFERENCES

Aldrich F K (2003). Smart homes: past, present and future. *Inside the smart home*, Springer, London, 17-39.

Ay A N, Yildiz M Z & Boru B (2017). Real-time feature extraction of ECG signals using NI LabVIEW. *Sakarya University Journal of Science*, *21*(4), 576-583.

Bhardwaj P, Manchanda P, Chahal P, Chaudhary P & Singh R (2017). A review paper on smart home automation. *International Journal of Scientific Research and Management Studies (IJSRMS), 3*, 279-283.

Cahill S, Macijauskiene J, Nygård A M, Faulkner J P & Hagen I (2007). Technology in dementia care. *Technology and Disability*, *19*(2-3), 55-60.

Coskun I & Ardam H (1998). A remote controller for home and office appliances by telephone. *IEEE Transactions on Consumer Electronics*, *44*(4), 1291-1297.

Douligeris C (1993). Intelligent home systems. *IEEE Communications Magazine*, *31*(10), 52-61.

Fernández J L, Losada D P & Domonte E P (2014). An integrated and low-cost home automation system with flexible task scheduling. In *XV Workshop of physical agents*.

González A B, Selmes M & Selmes J (2017). Can smart homes extend people with Alzheimer’s disease stay at home? *Journal of Enabling Technologies*, *11*(1).

Ienca M, Fabrice J, Elger B, Caon M, Scoccia Pappagallo, A, Kressig R W & Wangmo T (2017). Intelligent assistive technology for Alzheimer’s disease and other dementias: a systematic review. *Journal of Alzheimer's Disease*, *56*(4), 1301-1340.

Koyuncu B (1995). PC remote control of appliances by using telephone lines. *IEEE Transactions on Consumer Electronics*, *41*(1), 201-209.

Lauriks S, Reinersmann A, Van der Roest H G, Meiland F J M, Davies R J, Moelaert F, ... & Dröes R M (2007). Review of ICT-based services for identified unmet needs in people with dementia. *Ageing research reviews*, *6*(3), 223-246.

Maresova P, Tomsone S, Lameski P, Madureira J, Mendes A, Zdravevski E & Rodile K (2018). Technological solutions for older people with Alzheimer's disease. *Current Alzheimer Research*, *15*(10), 975-983.

Mennicken S, Vermeulen J & Huang E M (2014). From today's augmented houses to tomorrow's smart homes: new directions for home automation research. In *Proceedings of the 2014 ACM International Joint Conference on Pervasive and Ubiquitous Computing*, 105-115.

Muurling M, de Boer C, Kozak R, Religa D, Koychev I, Verheij H & Visser P J (2021). Remote monitoring technologies in Alzheimer’s disease: design of the RADAR-AD study. *Alzheimer's research & therapy*, *13*(1), 1-13.

Niranjan L, Nethravathi V, Bhavya Shree G, Nethravathi G, Rithu S (2017). Home Automation using SCADA & IOT. *International Journal of Engineering Research in Electronics and Communication Engineering, 4* (6).

Oskouei R J, Mousavi Lou Z, Bakhtiari Z & Jalbani K B (2020). IoT-Based Healthcare Support System for Alzheimer’s Patients. *Wireless Communications and Mobile Computing*.

Pal D, Triyason T & Funikul S (2017). Smart homes and quality of life for the elderly: a systematic review. In *2017 IEEE International Symposium on Multimedia (ISM)*, 413-419.

Soliman M S, Alahmadi A A, Maash A A & Elhabib M O (2017). Design and implementation of a real-time smart home automation system based on arduino microcontroller kit and labview platform. *International Journal of Applied Engineering Research*, *12*(18), 7259-7264.

Zaro F, Tamimi A & Barakat A (2021). Smart home automation system. *International Journal of Engineering and Innovative Research,* 3(1).

Turkish Journal of Engineering – 2022; 6(3); 245-250

Turkish Journal of Engineering
https://dergipark.org.tr/en/pub/tuje
e-ISSN 2587-1366

Performance evaluation of model predictive control method for neutral point clamped inverter

Ozan Gülbudak*[1], Mustafa Gökdağ [1]

[1]*Karabuk University, College of Engineering, Electrical-Electronics Engineering, Karabük, Turkey*

Keywords
Model predictive control
NPC inverter
Optimal control
Optimization
Power converters

ABSTRACT

The neutral-point clamped (NPC) inverter is a popular three-level converter topology used in motor drive applications and other dc/ac converter systems. In this paper, the performance evaluation of the model predictive control is performed to investigate its applicability in controlling NPC inverters. The model predictive control (MPC) is a promising closed-loop control strategy in applications where multiple control goals are considered. The ease of adding the objectives to the control law improves the reputation of the MPC. The numerous control goals can be regulated in single feedback. Thus, the adequate bandwidth is noticeably higher compared to the traditional linear controllers. However, controlling the multiple objectives require the use of weighting factors to tune the system performance. Regarding the system performance, multiple reference tracking performance is investigated in this study. Our case study considers three control goals: output load current, switching frequency control, and capacitor voltage balancing. The predictive control is designed to regulate these dynamics, and comprehensive performance analyses are performed. The designed controller is tested using a simulation tool. The simulation results prove that predictive control offers an excellent multi-objective control performance provided that the weighting factors and other design parameters are finely adjusted. The poor selection of the design parameters affects the closed-loop performance, and the conducted analyses show the effects of the controller parameters.

1. INTRODUCTION

The neutral-point clamped (NPC) inverters are broadly preferred in ac drive applications and power electronics systems. It is a three-level three-phase inverter that can utilize three different voltage levels ($0.5V_{dc}$, 0, $-0.5V_{dc}$) at the inverter output. This offers a substantial benefit regarding reducing the voltage stress on the active switches. Furthermore, the power level can be doubled due to the half voltage across switching devices. The other important aspect of NPC inverter is that the first few harmonics are centered around the two times higher of the operating frequency (switching frequency) (Klabunde et al. 1994; Nabae, et al. 1981; Rojas et al. 1995). This simplifies the procedure of selecting the filter parameter; thus, more efficient filtering capability is attained. A superior harmonics attenuation is achieved, improving the quality of the controlled variables, such as the output voltage or current. Besides the topological advantages of NPC inverters, a higher number of active switches is required to utilize the NPC inverter. In a traditional two-level voltage source inverter, only 6 active switches are used.

However, the NPC inverter employs the 12 active switches, and more active switches increase the switching losses. The other critical point is that the control complexity is higher compared to the two-level topologies. In particular, the capacitor voltage balancing must be considered in the controller design process. In the literature, the voltage balancing problem has been reported in several research papers (Jarutus and Kumsuwan, 2017). Different types of strategies have been investigated to overcome the capacitor voltage imbalance problem.

In the literature, different control and modulation strategies have been reported for NPC inverter systems. The optimal switching frequency technique was introduced in (Steinke, 1992). An analytical method to

---

* **Corresponding Author**

*(ozangulbudak@karabuk.edu.tr) ORCID ID 0000 – 0001 – 9517 – 3630
(mgokdag@karabuk.edu.tr) ORCID ID 0000 – 0001 – 5589 – 2278

Cite this article

Gülbudak O & Gökdag M (2022). Performance evaluation of model predictive control method for neutral point clamped inverter. Turkish Journal of Engineering, 6(3), 245-250

Research Article / DOI: 10.31127/tuje.962857

Received: 05/07/2021; Accepted: 11/10/2021

analyze NPC inverter dynamics and the performance of the capacitor voltage balancing are extensively examined (Ogasawara and Akagi, 1993). A comprehensive stability analysis of neutral-point control (Newton and Sumner, 1997) has been performed, a model that explains the system dynamics has been proposed. Moreover, a predictive control scheme has been introduced in (Vargas et al. 2007), multi-objective optimization problem has been formulated to control NPC inverter. The self-balancing effect has been investigated in (Jie et al. 2011), the effects of the self-balancing on the switching frequency have been reported. Another interesting work (Choi et al. 2015) shows that the voltage oscillations can be reduced by introducing an offset in time to the switch turn-on procedure. Other control mechanisms are also available in the literature. To gain a depth understanding of the NPC system, a good survey paper (Rodriguez et al. 2010) can be referred to.

In this study, the model predictive control method is investigated to analyze the dynamic characteristic of MPC. The control goals are considered the multi-objective optimization problem and the output load current, capacitor voltage balancing, and average switching frequency. The effects of the design parameters are examined, the feasibility of the MPC strategy in controlling NPC inverter is explored. The simulation works verify the system model and the formulated MPC controller. The simulations work demonstrates the potency of the MPC method; however, the design parameters have considerable influences on the steady-state and transient performance.

2. SYSTEM MODEL

In this section, the system mode of the NPC inverter is given. The NPC inverter topology schematic is illustrated in Fig. 1. Each NPC inverter leg has four active switches and two diodes; a high number of switching combinations are possible in this configuration. However, there are some switching restrictions to ensure stable operation. Thus, some of these switching states are not permissible. By considering the switching limitations, the NPC inverter yields 27 allowable switching states. To have a significant sub-set (solution set) allows flexibility in designing the objective function. In NPC inverter, the switching state $S_{j\alpha}$ refers to switching status of phase j, with j∊ {a,b,c} and α ∊{1,2,3,4}. At the output of the inverter stage, three discrete voltage levels can be generated. The switching state for each phase is summarized in Table 1. The parameter P refers to positive dc voltage, and N refers to negative dc voltage. 0 denotes the zero dc voltage at the output of the inverter stage.

Table 1. The switching states for each phase

S_j	S_{j1}	S_{j1}	S_{j1}	S_{j1}	v_{j0}
P	1	1	0	0	$v_{dc}/2$
0	0	1	1	0	0
N	0	0	1	1	$-v_{dc}/2$

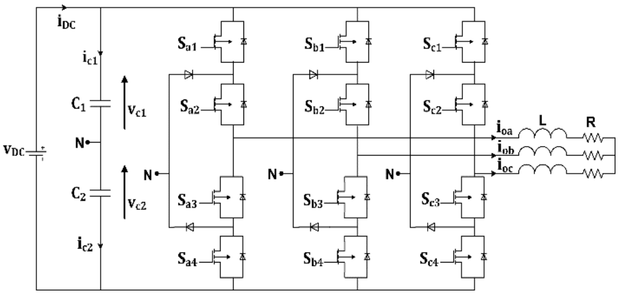

Figure 1. The neutral-point clamped inverter circuit diagram.

Some voltage vectors that the NPC inverter can produce are redundant. Thus, these voltage vectors can be eliminated in the controller design process. The space vector form of the output voltage and current are expressed as

$$\boldsymbol{v_o} = \frac{3}{2}(v_{oa} + \boldsymbol{r}v_{ob} + \boldsymbol{r}^2 v_{oc}) \tag{1}$$

$$\boldsymbol{i_o} = \frac{3}{2}(i_{oa} + \boldsymbol{r}i_{ob} + \boldsymbol{r}^2 i_{oc}) \tag{2}$$

where $\boldsymbol{r} = e^{j(2\pi/3)}$. The continuous-time model of the load current is defined as

$$\boldsymbol{v_o} = L\frac{d\boldsymbol{i_o}}{dt} + R\boldsymbol{i_o} \tag{3}$$

The capacitor voltage dynamic models can be derived as

$$C\frac{dv_{c1}}{dt} = i_{c1} \tag{4}$$

$$C\frac{dv_{c2}}{dt} = i_{c2} \tag{5}$$

To acquire the discrete-time model of the control variable, a numerical method can be applied. In this study, the Forward Euler method is used to convert the continuous data to sampled data. The Forward Euler approximation is as follows:

$$\frac{df(t)}{dt} \approx \frac{f(k+1) - f(k)}{T_s} \tag{6}$$

k denotes the sampling instant. T_s implies the sampling period. By using (6), the discrete-time model of (3) results

$$\boldsymbol{i_o}(k+1) = \left(1 - \frac{RT_s}{L}\right)\boldsymbol{i_o}(k) + \frac{T_s}{L}\boldsymbol{v_o}(k) \tag{7}$$

In (7), $\boldsymbol{i_o}(k+1)$ is the prediction of the load current, $\boldsymbol{i_o}(k)$ refers to the instantaneous load current measurement, and $\boldsymbol{v_o}(k)$ denotes the output load voltage. By applying the same procedure, the capacitor voltage prediction models are defined as

$$v_{c1}(k+1) = v_{c1}(k) + \frac{1}{C_1}i_{c1}(k)T_s \tag{8}$$

$$v_{c2}(k+1) = v_{c2}(k) + \frac{1}{C_2}i_{c2}(k)T_s \tag{9}$$

In (8)-(9), $i_{c1}(k)$ and $i_{c2}(k)$ are the capacitor current measurements. C_1 and C_2 are the capacitance at the inverter input. However, the measurement of these quantities is not a straightforward task (in most cases, the capacitor current measurement is meaningless due to the fast dynamic), $i_{c1}(k)$ and $i_{c2}(k)$ can be estimated by using the dynamic model of the capacitor and NPC inverter. The estimation can be performed based on (10) and (11).

$$i_{c1} = i_{dc}(k) - G_{1a}i_{oa}(k) - G_{1b}i_{ob}(k) - G_{1c}i_{oc}(k) \qquad (10)$$

$$i_{c2} = i_{dc}(k) - G_{2a}i_{oa}(k) - G_{2b}i_{ob}(k) - G_{2c}i_{oc}(k) \qquad (11)$$

where

$$G_{1j} = \begin{cases} 1, & S_j = P \\ 0, & S_j = N \text{ } or \text{ } 0 \end{cases} \qquad (12)$$

$$G_{2j} = \begin{cases} 1, & S_j = N \\ 0, & S_j = P \text{ } or \text{ } 0 \end{cases} \qquad (13)$$

with j ϵ {a,b,c}. $i_{c1}(k)$ and $i_{c2}(k)$ relies on the switch positions. Thus, they can be estimated using the instantaneous switch positions. As a final comment, the prediction model of the system is derived, and the MPC uses (7)-(11) to predict the control goals.

3. PREDICTIVE CONTROL SCHEME

The predictive controller uses the prediction model of the system to predict the output load currents and the capacitor voltage for each allowable control inputs (27 switching states). The measurements in the MPC control scheme are the output load current, capacitor voltage, dc-bus voltage, and dc-bust current. These four measurements are necessary to apply the predictive control routine. Once the prediction of the control variables process is over, the cost function is evaluated for every legitimate state. The designed objective function is defined as

$$g_{NPC} = g_1 + g_2 + g_3 \qquad (14)$$

where

$$\begin{aligned} g_1 = {} & |i^*_{oa}(k+1) - i_{oa}(k+)|^2 \\ & + |i^*_{ob}(k+1) - i_{ob}(k+)|^2 \\ & + |i^*_{oc}(k+1) - i_{oc}(k+)|^2 \end{aligned} \qquad (15)$$

$$g_2 = \Gamma_{vc}|v_{c1}(k+1) - v_{c2}(k+1)| \qquad (16)$$

$$\begin{aligned} g_3 = \Gamma_{swc}(&\left|S_{j1}(k+1) - S_{j1}(k)\right| + \cdots \\ & + \left|S_{j4}(k+1) - S_{j4}(k)\right|) \end{aligned} \qquad (17)$$

In (14), the term g_1 is responsible for tracking the output load current trajectory. The load current error terms are introduced in g_1 to effectively control the output load current. The term g_2 controls the capacitor voltages; thus, the voltage imbalance problem is solved by the inclusion of g_2 term. Moreover, g_3 is responsible for controlling the switching frequency. In power electronics, the switching loss increases with the switching frequency. Thus, controlling the switching frequency is highly desirable to achieve an acceptable conversion efficiency. The predictive control scheme is depicted in Fig. 2. Following Fig. 2, the control variables are controlled by assessing the objective function. The switching state that offers a minimum cost of g_{NPC} is picked and applied to the NPC inverter. This feedback algorithm is repeated at every sampling instant k. Therefore, the MPC implementation can be considered as an iterative operation.

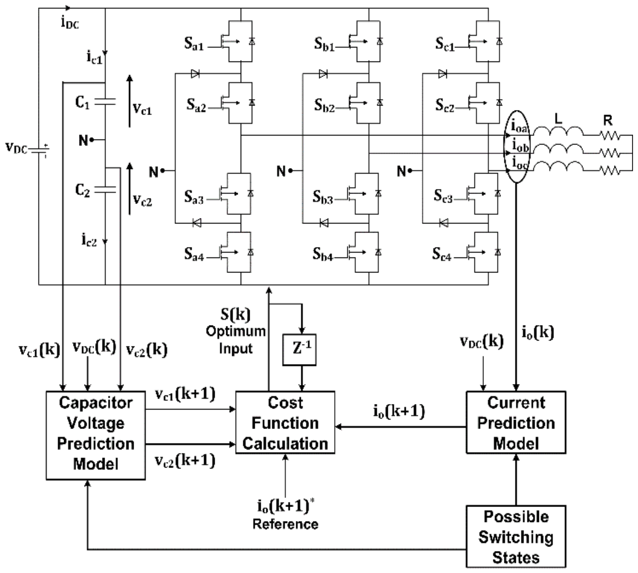

Figure 2. The model predictive control scheme

When $v_{c1}(k+1)$ and $v_{c2}(k+1)$ are equal each other, g_2 results zero. In this case, perfect voltage balancing is achieved. The term g_3 implies that transition from one state to another is penalized. Thus, g_3 has a big influence on the switching frequency reduction. The switching state transition rate is inherently limited due to the penalization term of g_3. The other important design parameters are the weighting factors Γ_{vc} and Γ_{swc}. Γ_{vc} implies the importance of the voltage balancing term. The control of the capacitor voltage equalization becomes more critical as Γ_{vc} increases. Thus, the weighting factors are quite important tuning parameters. The weight Γ_{swc} is the tuning parameter of the switching frequency control term g_3. A large value of Γ_{swc} offers a better switching frequency regulation. In an optimization problem formed by more than one control goal, the weighting factors are required to handle the relationship between control terms. The critical comment on the nomination of these weighting factors is that a good approach to determine the weighting factors has not been proposed yet. In most cases, simulation-based tuning methods are used to determine these tuning parameters.

4. SIMULATION RESULTS AND PERFORMANCE EVALUATION

To perform the performance analyses, the system is simulated using Matlab/Simulink. The simulation parameters are given in Table 2. To assess the steady-state performance, the control variables are monitored. Fig. 3 presents the steady-state waveforms. In this test scenario, the load current reference is 10 A peak with 50

Hz fundamental frequency. According to the steady-state results, the output load current looks good, see Fig. 3(a). The capacitor balancing performance is acceptable, see Fig. 3(b), no big deviation between v_{c1} and v_{c2} is observed.

Table 2. Simulation parameters

Parameters	Description	Values
v_{dc}	dc-bus voltage	380 V
C_1	C_1 capacitance	750 µF
C_2	C_2 capacitance	750 µF
R	Load resistance	5 Ω
L	Load inductance	10 mH
T_s	Sampling period	20 µs
Γ_{vc}	Weighting factor	0.6
Γ_{swc}	Weighting factor	0.05
Solver	Simulink solver	Ode-45

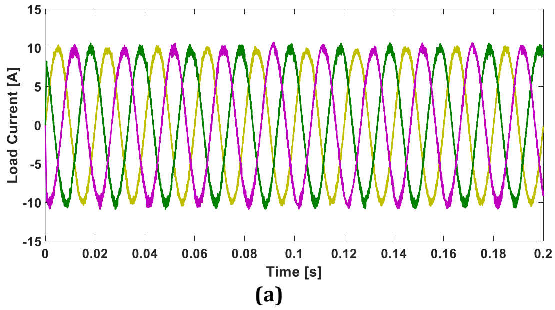

(a)

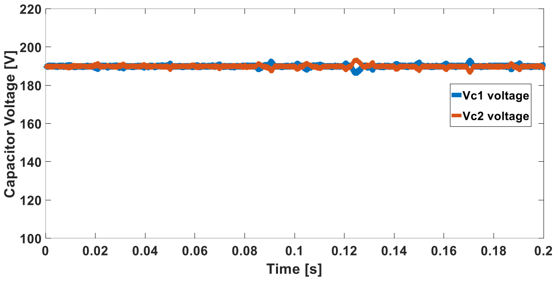

(b)

Figure 3. The steady-state waveform of the predictive controller. (a) The output load current waveform (b) Capacitor voltage waveform.

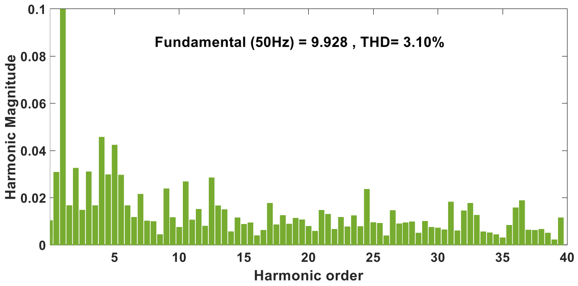

Figure 4. FFT analysis of the load current up to 40th harmonics.

To examine the load current quality, Fast Fourier Transform (FFT) analysis is conducted. The spectral contents are calculated up to 40th harmonics. The frequency spectrum waveform of the output load current is reported in Fig. 4 under steady-state conditions. The load current total harmonic distortions are roughly 3.10%. The calculated THD level is quite acceptable, and the quality of the load current satisfies the design specifications.

The magnitude of the fundamental frequency (50 Hz) is 9.928 A, close to the reference value of 10 A. To investigate the transient performance of the predictive controller, the load current step is applied to the NPC inverter system. The transient response of the system is reported in Fig. 5. The load current step is applied to 5 A peak to 10 A. The predictive controller gives a quick response to the load variations and compensates for the error. The capacitor voltage control is attained, no unwanted discrepancy is observed. Both capacitor voltage is approximately 190 V which corresponds to half of the dc-bus voltage v_{DC}.

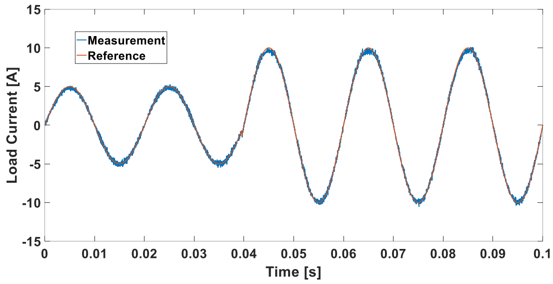

(a)

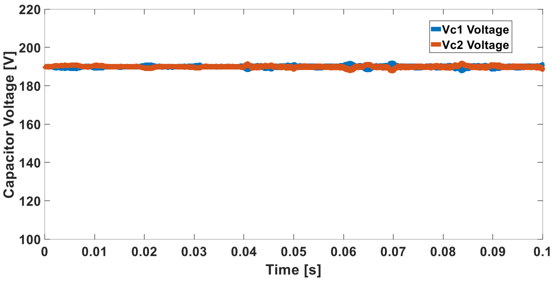

(b)

Figure 5. The transient waveform of the predictive controller. (a) The load current waveform (measurement and reference) (b) Capacitor voltage waveform

To explore the weighting factor Γ_{vc} effects on the capacitor voltage balancing performance, Γ_{vc} set as 0. Then, Γ_{vc} has switched to its nominal value of 0.6. When Γ_{vc}=0, the capacitor voltage balancing is ignored by the predictive controller. It means that the capacitor voltage imbalance is not penalized; thus, the capacitor voltages may not be equal. The effect of Γ_{vc} is presented in Fig. 6, and the fine choice of Γ_{vc} remarkably reduces the voltage imbalance. These simulation results prove that the predictive controller performance highly relies on the selected weighting factors.

For Γ_{vc}=0, v_{c2} is approximately 200 V while v_{c1} is 180 V at the same time. This causes voltage imbalance. For Γ_{vc}=0.6, both capacitor voltages approximately equal 190 V.

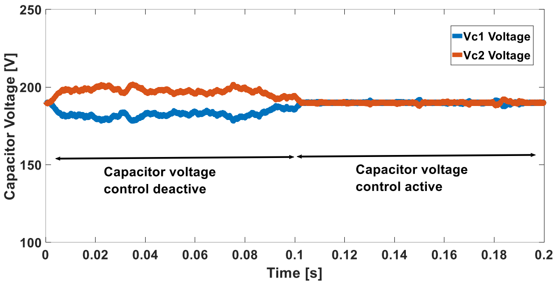

Figure 6. The impacts of the parameter Γ_{vc} on the term $|v_{c1}-v_{c2}|$.

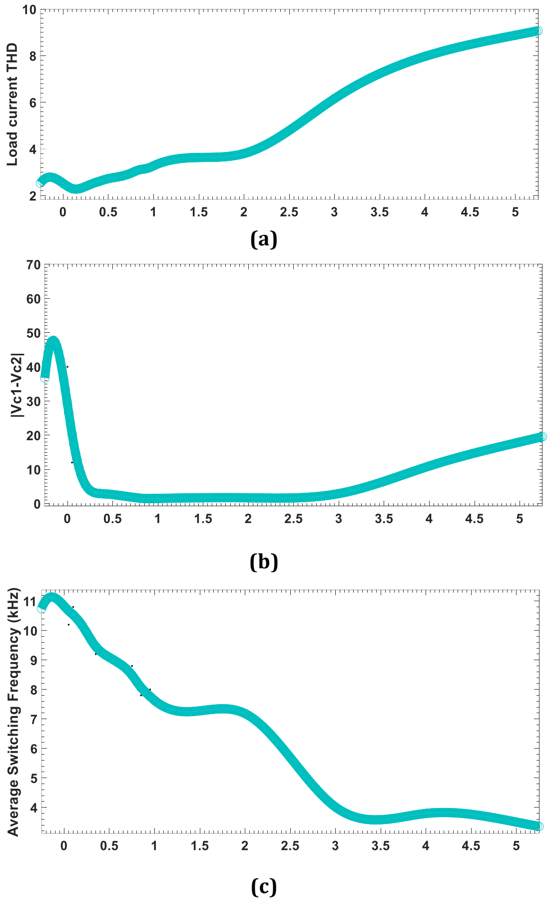

Figure 7. The impacts of the parameter Γ_{vc} on the control variables. (a) The waveform Γ_{vc} vs load current THD. (b) The waveform Γ_{vc} vs. $|v_{c1}-v_{c2}|$. (c) The waveform Γ_{vc} vs. operating frequency.

The effects of the parameter Γ_{vc} on the controller, variables are shown in Fig. 7. The load current has a high THD tendency as Γ_{vc} increases. For the lower choice of Γ_{vc} such as $0.05<\Gamma_{vc}<0.8$, the load current THD varies between 2.43%< THD<3.1%. This THD level is quite acceptable, and it complies with the international standard. However, further, increase in Γ_{vc} degrade the load current quality, see Fig. 7(a). The choice of $\Gamma_{vc}>2$ has a negative influence on the load current THD. The THD level is drastically increased; thus, the selection of Γ_{vc} is quite critical. The capacitor voltage imbalance is reduced with a higher value of Γ_{vc}. The choice of $0.05<\Gamma_{vc}<3$ improves the capacitor voltage control, the parameter $|v_{c1}-v_{c2}|$ varies between 6V and 2.9 V. However, the further increase in Γ_{vc} does not help to improve the control of $|v_{c1}-v_{c2}|$. The voltage imbalance equals 18 V when Γ_{vc} is selected as 5. The main reason for the practical limit on the capacitor voltage control performance is that a higher value of Γ_{vc} causes the increase in the load current THD. Therefore, the control of the capacitor voltage becomes challenging due to the high distortions. For that reason, Γ_{vc} should be selected such that all control variables remain in the acceptable range. The switching frequency decreases with the increase in Γ_{vc}. Fig. 7 (c) show the mean value of the operating frequency versus the Γ_{vc}. The computed average operating frequency range is within 3.5kHz<f_{sw}<11 kHz. By taking into all analyses results presented in Fig.7, the range within $0.05<\Gamma_{vc}<1$ is the sweet spot for Γ_{vc}. The selection of Γ_{vc} within this range offers a good control performance of all control goals. The last evaluation work is performed to analyze the effects of switching frequency control term Γ_{swc}. In this performance assessment process, two control variables are under consideration: the load current THD and the average switching frequency. The effect of Γ_{swc} on the load current, THD, and the mean value of the operating frequency is shown in Fig. 8. The load current THD increases as the value of Γ_{swc} increases. In particular, the selection of $\Gamma_{swc}>4$ degrades the output load current control performance. The key reason for this harmful effect is that the switching frequency is noticeably reduced with the increase in Γ_{swc}, see Fig. 8 (b). The switching transitions are further penalized by increasing Γ_{swc}. Thus, the NPC inverter does fewer switching transitions resulting in a lower switching frequency. However, the output load current control is negatively influenced. Based on the collected simulation results, the selection of $0.5<\Gamma_{swc}<2.5$ is recommended to attain good steady-state performance.

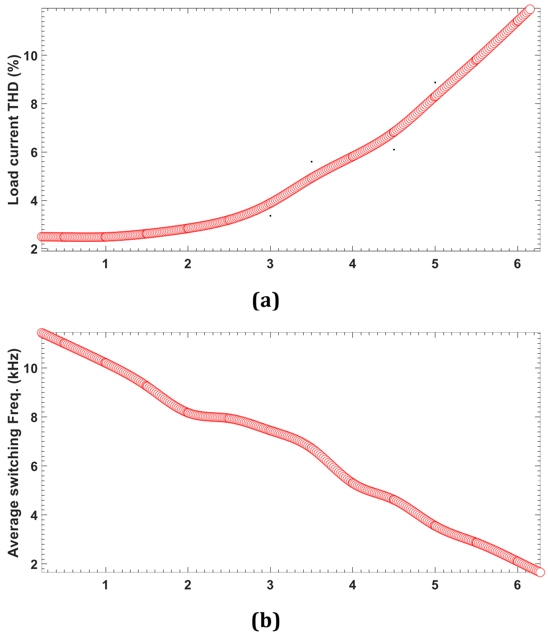

Figure 8. The impact of the tuning parameter Γ_{swc} on the control variables. (a) The waveform Γ_{swc} vs. load current THD. (b) The waveform Γ_{swc} vs. switching frequency.

Finally, the proposed control method is compared with the conventional control technique which is based on the proportional-integral (PI) combined with the linear modulator. Table 3 summarizes the comparison results. According to Table 3, the proposed method offers faster dynamic response than the conventional method to load perturbations. The transient time is noticeably lower for the proposed strategy. On the other hand, the traditional method provides a lower THD under steady-state performance.

Table 3. Comparison results

Metric	PI+Modulator	MPC
Transient time	210 µs	155 µs
Load current THD	3.05 %	3.10 %
Modulator	Required	No
Inclusion of constraints	No	Yes
Inclusion of nonlinearity	No	Yes
Switching frequency	Fixed	Variable
Design complexity	High	Low
Voltage balancing	Yes	Yes

The PI+modulator requires the linear modulator to generate the gate signals. Thus, the switching frequency is fixed. However, the inclusion of the modulator increases the complexity of the design stage. On the contrary, the MPC strategy does not require a modulator; therefore, the switching frequency varies during the operation. Both control methods offer voltage balancing capability. The other important aspect is that the conventional method does not provide the flexibility to include the nonlinearities or control constraints. On the other hand, the inclusion of the system constraints is relatively easy in the MPC method. Regarding the simplicity of the feedback design, the MPC method has several advantages over the traditional control method.

5. CONCLUSION

This paper has presented the performance evaluation of the predictive control method for the NPC inverter. The performance analyses have been conducted to scrutinize the steady-state performance and transient performance of the MPC. The impacts of the design parameters on the trajectory tracking performance have been substantially analyzed. Several simulation works have been conducted to prove the effectiveness of the MPC in handling the multi-control objectives. The simulation results demonstrate that multiple-control goals are effectively regulated, and the NPC inverter provides a robust system operation. The choice of the weighting factor highly influences the error compensation performance. Thus, weighting factors should be finely selected to achieve a reliable energy conversion operation.

Author contributions

Ozan Gulbudak: Design and analyses, Methodology **Mustafa Gokdag:** Simulation, Writing-Original draft preparation.

Conflict of interest

The authors declare no conflicts of interest

REFERENCES

Choi U-M, Blaabjerg F & Lee K-B (2015). Method to Minimize the Low-Frequency Neutral-Point Voltage Oscillations With Time-Offset Injection for Neutral-Point-Clamped Inverters. *IEEE Transactions on Industry Applications*, *51*(2), 1678–1691. https://doi.org/10.1109/TIA.2014.2350079

Jarutus N & Kumsuwan Y (2017). A Carrier-Based Phase-Shift Space Vector Modulation Strategy for a Nine-Switch Inverter. *IEEE Transactions on Power Electronics*, *32*(5), 3425–3441. https://doi.org/10.1109/TPEL.2016.2587811

Jie S, Schröder S, Rösner R & El-Barbari S (2011). A Comprehensive Study of Neutral-Point Self-Balancing Effect in Neutral-Point-Clamped Three-Level Inverters. *IEEE Transactions on Power Electronics*, *26*(11), 3084–3095. https://doi.org/10.1109/TPEL.2011.2138161

Klabunde M C, Yifan Z, & Lipo T A (1994). Current control of a 3-level rectifier/inverter drive system. *Proceedings of 1994 IEEE Industry Applications Society Annual Meeting*, 859–866. https://doi.org/10.1109/IAS.1994.377519

Nabae A, Takahashi I & Akagi H (1981). A New Neutral-Point-Clamped PWM Inverter. *IEEE Transactions on Industry Applications*, *IA-17*(5), 518–523. https://doi.org/10.1109/TIA.1981.4503992

Newton C & Sumner M (1997). Neutral point control for multi-level inverters: theory, design and operational limitations. *IAS '97. Conference Record of the 1997 IEEE Industry Applications Conference Thirty-Second IAS Annual Meeting*, *2*, 1336–1343. https://doi.org/10.1109/IAS.1997.629031

Ogasawara S & Akagi H (1993). Analysis of variation of neutral point potential in neutral-point-clamped voltage source PWM inverters. *Conference Record of the 1993 IEEE Industry Applications Conference Twenty-Eighth IAS Annual Meeting*, 965–970. https://doi.org/10.1109/IAS.1993.299015

Rodriguez J, Bernet S, Steimer P K & Lizama I E (2010). A Survey on Neutral-Point-Clamped Inverters. *IEEE Transactions on Industrial Electronics*, *57*(7), 2219–2230. https://doi.org/10.1109/TIE.2009.2032430

Rojas R, Ohnishi T & Suzuki T (1995). An improved voltage vector control method for neutral-point-clamped inverters. *IEEE Transactions on Power Electronics*, *10*(6), 666–672. https://doi.org/10.1109/63.471286

Steinke J K (1992). Switching frequency optimal PWM control of a three-level inverter. *IEEE Transactions on Power Electronics*, *7*(3), 487–496. https://doi.org/10.1109/63.145136

Vargas R, Cortes P, Ammann U, Rodriguez J & Pontt J (2007). Predictive Control of a Three-Phase Neutral-Point-Clamped Inverter. *IEEE Transactions on Industrial Electronics*, *54*(5), 2697–2705. https://doi.org/10.1109/TIE.2007.899854

Turkish Journal of Engineering
https://dergipark.org.tr/en/pub/tuje
e-ISSN 2587-1366

Short-term wind power prediction with harmony search algorithm: Belen region

Esra Saraç Eşsiz[*1]

[1]*Adana Alparslan Türkeş Science and Technology University, Engineering Faculty, Computer Engineering Department, Adana, Turkey*

Keywords
Renewable Energy
Wind power
Artificial neural networks
Feature Selection
Short-term forecast

ABSTRACT

Wind power is the fastest-growing technology among alternative energy production sources. Reliable forecasting of short-term wind power plays a critical role in the acquisition of most of the generated energy. In this study, short-term wind power forecast is performed using radial-based artificial neural networks, forecast error and cost to be minimized with the harmony search algorithm. Experimented results show that, we can predict wind power with fewer features and less error by using harmony search algorithm. A %7 percent improvement in RMSE rate has been achieved with the proposed method for short-term wind power prediction.

1. INTRODUCTION

The required energy of the world raises nearly 4-5% every year meanwhile the fossil fuel reserve that accommodated the world's need is decreasing day by day. It is predicted that the oil, coal and natural gas reserves, which are among the basic energy resources, will be depleted in the next 30-40 years at best. The increase in the use of fossil fuels has also increased the world average temperature. Increasing temperature caused material and moral damages and loss of life by triggering various natural events such as floods and storms. Evacuations have begun with the melting of glaciers and the rise of the water level on many islands located at sea level. Without action, life in cities at sea level will not be possible. Clean energy sources have now become an obligation, not an alternative. It is essential to turn to clean resources without waiting for the depletion of energy reserves. Using renewable energy sources is advantageous in many ways. The most important of these advantages are reducing foreign dependency, providing cheap energy, no fuel expense, and being environmentally friendly. Due to these advantages, its use is increasing day by day. Wind power, one of the popular renewable energy alternatives, is of great importance in terms of the wind potential in our country. Among the European countries, Germany is the country that benefits from wind power the best. Spain follows Germany in second place. According to the German Wind power Institute DEWI, Spain's wind potential and Turkey's wind potential are equivalent. According to the wind map of our country, electricity can be produced from wind power in four seasons a year. In order to produce energy without the need for any other energy support, a storage area of 6 times the hourly production is required. Despite this high potential, wind power is the least utilized resource in energy generation.

Turkey's Wind Power Potential Atlas (REPA), prepared by the Ministry of Energy and Natural Resources and prepared by the Electrical Works Survey Administration (EIE), determines Turkey's wind power potential and guides investors. According to REPA, wind power of our country is 67 MW. Again, according to the same report, our country has a wind power potential of 50000 MW. The installation of wind power plants is also ongoing in Turkey.

There are some operational challenges for both electrical systems and electricity markets when the

---

[*] **Corresponding Author**

[*](esarac@atu.edu.tr) ORCID ID 0000-0002-2503-0084

Cite this article

Eşsiz E S (2022). Short-term wind power prediction with harmony search algorithm: Belen region. Turkish Journal of Engineering, 6(3), 251-255

Research Article / DOI: 10.31127/tuje.970959

Received: 13/07/2021; Accepted: 15/08/2021

large-scale integration of wind power (Exizidis et al., 2017). Wind power prediction takes an important role in the reliable and economical process of power systems with wind leakage (Cui et al., 2017). Long-term predictions of wind energy are necessary for capacity planning and maintenance planning (Kanna and Singh, 2016). Medium term forecasts are used for maintenance planning (Alberdi et al., 2017; Bae et al., 2017), fuel planning (Guangyu et al., 2017) and hydro pool management (Meng et al., 2015). Short-term load prediction is a fundamental and vital factor for daily operations, unit commitment and timing functions, assessment of net change and system security analysis (Zhou et al., 2016a; Zhou et al., 2016b). Very short-term predictions are used for optimizing the process of wind energy reserves (Wang et al.; 2017). When the literature is reviewed, there are many studies on wind prediction in recent years (Zhuo and Savkin, 2017). Long-term wind prediction has been performed using the adaptive wavelet neural network method (Kanna and Singh, 2016). In the literature, support vector machine regression model (Ahmed et al., 2017), nonlinear autoregressive network model with extroverted inputs (Baby et al., 2017), double-tier hierarchical genetic algorithm trained artificial neural network model (Li et al.; 2017), deep learning network architecture model with stacked automatic encoders (Khodayar et al., 2017), particle swarm optimization-based adaptive neuron fuzzy inference model (Eseye et al., 2017), particle swarm optimization model integrated with mutation operator (Quan et al., 2013), K-clustering-based artificial sine network model (Xu et al., 2015) and advanced Markov model (Yang et al., 2015) are used for short-term wind prediction. Very short-term wind estimation has been performed using the spatial-temporal method (Dowell and Pinson, 2015), neural fuzzy networks method (Paixao et al., 2017), and autoregressive model and Hilbert-Huang transform method (Shi et al., 2016).

The aim of this study is to show the effects of feature selection on the performance of short-term wind power prediction. In the literature, there is no such study to our knowledge, and the results presented here will be helpful to researchers.

The rest of the paper is organized as follows: in the second section, a detailed overview of the dataset and methods are presented. Experimental results are discussed in the third section.

2. METHOD and DATASET

In this study, the wind power dataset produced by the Belen region wind power plant is used to predict short-term wind power using the radial-based artificial neural networks and the harmony search feature selection algorithm. Details about the dataset and methods used are given in the next subsections.

2.1. Dataset

The yearly data which is obtained from wind turbines in Belen region and recorded on a daily was used in this study. Wind turbine model is seen in Figure 1.

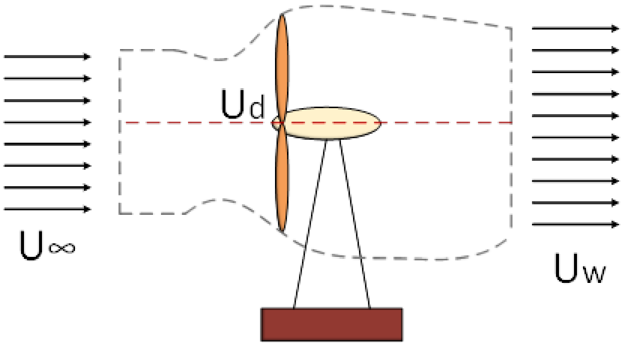

Figure 1. Wind Turbine Model

The dataset contains 365 different sample data with 10 numeric features; *day*, *ud*, *m*, *a, uw*, *U∞*, *cp*, *ct*, *trust*, *kn* and finally the *class* value representing the amount of electricity generated, which represents the output value of the modeled network.

2.2. Radial Based Artificial Neural Networks

Radial-based regressor was used to train the regression model in proposed study. Radial-based neural network model is shown in figure 2. While modeling the radial-based regressor, which is a supervised learning method, unlike traditional radial-based neural networks, the BFGS (Broyden-Fletcher-Goldfarb-Shanno algorithm) method, which is suitable for the optimization of nonlinear problems, has been used to minimize the quadratic error (Buhman, 2003). All attributes in the dataset used were normalized in the range of [0,1]. The model learned by the designed artificial neural network is given by equation 1.

$$f(x_1, x_2, \dots, x_m) = g(w_0 + \sum_{i=1}^{b} w_i \exp\left(-\sum_{j=1}^{m} \frac{a_j^2(x_j - c_{i,j})^2}{2\sigma_{i,j}^2}\right)) \qquad (1)$$

Such that; $x_1, x_2, \dots, x_m$ denote the attributes used, *g(.)* denoting the activation function, *b* denoting the number of basic functions, $w_i$is the weight value of each function, a_j^2 represents the weight of the j^{th} attribute, c_i and σ_i^2 are the central and variance values of the basic functions, respectively. Attribute weights were not used during the modeling. All a_j^2 values are taken as 1 as a constant. The value of *b*, which is the basic function number, was chosen as 5 empirically. The Least Squared Simulated Errors function used is given in equation 2.

$$LSSE = \frac{1}{2}\sum_{i=1}^{n}(y_i - f(\underset{x_i}{\to}))^2 + (\lambda \sum_{i=1}^{b} w_i^2) \qquad (2)$$

If the y_i value in the given function is the predicted valuex_i, it is the real value. *n* is the total number of training samples. λ is the penalty coefficient used to prevent over fitting and was taken as 0.01.

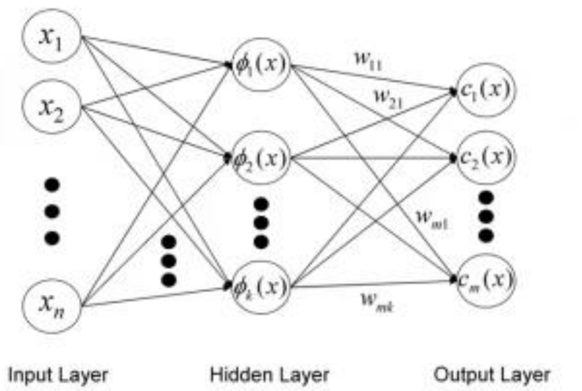

Figure 2. Radial-based Neural Network Model

2.3. Harmony Search Algorithm

Harmony search (Woo et al., 2001) is inspired by the music orchestra. It is one of the popular population-based algorithms. Like a music orchestra, which tends to create the most harmonious melody, this algorithm mimics the behavior of a music orchestra. In an orchestra, musicians repeatedly improve the melody; the HS algorithm, like the process in real orchestras, iteratively improves the fitness value of the candidate solutions. The candidate solutions are kept in the Harmony Memory. A new harmony vector is produced by applying optimization parameters to Harmony Memory.

First of all, HS start with the initialization of the HM, and then a new harmony is generated. If there is an improvement with newly generated harmony, this new harmony is included in the HM. Algorithm continues to generate the new harmony until a termination criterion is satisfied.

HS uses two different probabilistic operators to control the new harmony generation procedure, which are Harmony Memory Considering Rate (HMCR), and Pitch Adjusting Rate (PAR).

HMCR ∈[0,1], HMCR ∈[0,1], is used to define the probability of drawing a new note uniformly from the values of this same note. Without this probability value, algorithm can choose note values randomly.

PAR ∈[0,1], is similar to mutation operation in genetic algorithms, and it is used for to avoid local optima in the HS algorithm.

Pseudo code of Harmony Search Algorithm is given in Figure 3.

Nature inspired based Harmony search algorithm is used to select optimum features over wind power dataset to predict wind power with low error rates in the proposed study.

```
begin
Define fitness function f(a), $a = (a_1, a_2, \dots, a_N)^T$
Define (HMCR),(PAR),(HMS),(EOR)
Define Maximum number of iterations (NI).
$HM \leftarrow GenerateInitialPoplution()$
min = minimum visible value.
max = maximum visible value.
while ($iter \leq NI$) do
  while ($a_i \leq number\ \ of\ \ variables$) do
    if ($rand \in (0,1) \leq HMCR$) then
      choose a value from HM for i
      if ($rand \in (0,1) \leq PAR$) then
        adjust the value of i by:
        $a_{i_new} = a_{i_old} + rand \in (0,1) \times bw$
      end if
    else
      choose a random variable:
      $a_i = min + rand \in (0,1) \times (max - min)$
    end if
  end while
  if ($FitFun(new\ \ harmony\ \ solution) \leq worst(FitFun(HM))$) then
    accept the new harmony and replace the worst in HM with it.
  end if
end while
best=find the current best solution
end
```

Figure 3. Pseudo Code of Harmony Search Algorithm

3. RESULTS

In this study, the yearly data which is obtained from wind turbines in Belen region and recorded on a daily was used. So, the dataset contains 365 different sample data with 10 numeric features. The amount of electricity produced has been tried to be estimated so that other values in the data will be inputs. Radial based regressor method is used to perform the regression between the input set and the output set. Harmony search algorithm is used as feature selector. In Figure 3, Belen region and the power plant where data is taken are shown. Figure 4 shows the Turkey wind speed map.

Figure 4. Belen Wind Power Plant from Real Data

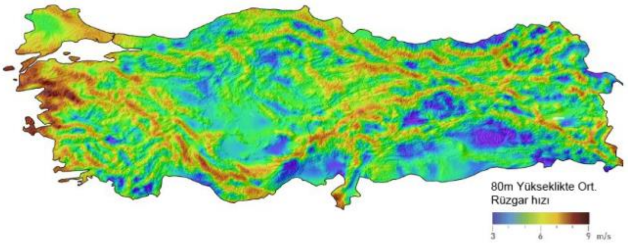

Figure 5. Turkey wind speed map

The dataset containing 365 samples was randomly separated as 70% training, 10% validation, and 20% testing. After the training process with radial based regressor is completed, the model is verified and tested on test data. The results obtained from the test data were evaluated according to the Root Mean Square Error (RMSE, Equation 3), Mean Absolute Error (MAE, Equation 4), and Correlation Coefficient (R, Equation 5) error measurement criteria.

$$\text{RMSE} = \frac{1}{n}\left[\sum_{i=1}^{n}(O_i - P_i)^2\right] \tag{3}$$

$$MAE = \frac{1}{n}\left[\sum_{i=1}^{n}|O_i - P_i|\right] \tag{4}$$

$$R = \sqrt{1 - \frac{\sum_{i=1}^{n}(O_i - P_i)^2}{\sum_{i=1}^{n}(O_i - O_m)^2}} \tag{5}$$

For the given equations;
n: number of data in test data,
P_i: predicted value
O_i: observed value
O_m: is the average of the observed values.

With the error equation, the squares of the errors are taken. In this way, the effect of higher error values in the predicted values on the average is higher, and the effect of these higher error values on the entire prediction can be determined. MAE considers the absolute error between actual values and model predictions. The model can be predicted more accurately if the RMSE and MAE values are close to zero. R value is used to define the relationship between the true value and the predicted value. The R values can be in the range of [+1, -1]. If the value of R is equal to +1, which is the biggest value it can take; there is a positive and fully linear relationship between variables.

According to HS algorithm, these 7 features were chosen; *day*, *ud*, *m*, *uw*, *U∞*, *cp* and *trust*. Comparison of selected features on wind power prediction with all 10 features is given in Table 2.

Table 2. Performance comparison of the proposed system with all features

	MAE	RMSE	R
All features	12.92	17.92	0.9997
HS Feature Selection	4.95	10.80	0.9998

Experimented results show that, wind power can be predicted with fewer features and less error by using harmony search algorithm. A %7 percent improvement in RMSE rate has been achieved with the proposed method for short-term wind power prediction.

Prediction of wind power with HS selected features is given in Figure 6.

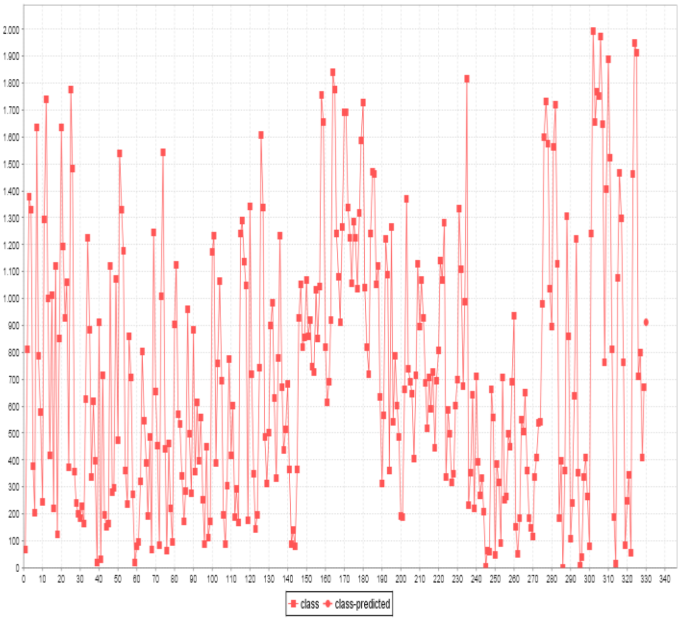

Figure 6. Prediction Result with Selected Features

With this study, daily wind power production was estimated and the most accurate information was tried to be given in order to adjust the storage capacities. The lower the error of the estimates, the more efficient use of the energy produced will be.

REFERENCES

Ahmed S, Khalid M & Akram U (2017). A method for short-term wind speed time series forecasting using Support Vector Machine Regression Model. In 2017 6th International Conference on Clean Electrical Power (ICCEP) (pp. 190-195). IEEE.

Alberdi R, Fernandez E, Albizu I, Mazón A J, Bedialauneta M T & Sagastabeitia K J (2017). Wind speed forecasting in overhead lines for system operation. In 2017 IEEE Manchester PowerTech (pp. 1-5). IEEE.

Baby C M, Verma K & Kumar R (2017). Short term wind speed forecasting and wind power estimation: A case study of Rajasthan. In 2017 International Conference on Computer, Communications and Electronics (Comptelix) (pp. 275-280). IEEE.

Bae H R, Tsuji T, Oyama T & Uchida K (2017). Frequency control in power system based on balancing market considering wind power forecasting error. In 2017 6th International Conference on Clean Electrical Power (ICCEP) (pp. 376-383). IEEE.

Buhmann M D (2003). Radial basis functions: theory and implementations (Vol. 12). Cambridge university press.

Cui M, Zhang J, Wang Q, Krishnan V & Hodge B M (2017). A data-driven methodology for probabilistic wind power ramp forecasting. IEEE Transactions on Smart Grid, 10(2), 1326-1338.

Dowell J & Pinson P (2015). Very-short-term probabilistic wind power forecasts by sparse vector autoregression. IEEE Transactions on Smart Grid, 7(2), 763-770.

Eseye A T, Zhang J, Zheng D, Ma H & Jingfu G (2017). Short-term wind power forecasting using a double-stage hierarchical hybrid GA-ANN approach. In 2017 IEEE 2nd International Conference on Big Data Analysis (ICBDA) (pp. 552-556). IEEE.

Exizidis L, Kazempour J, Pinson P, De Grève Z & Vallée F (2017). Impact of public aggregate wind forecasts on electricity market outcomes. IEEE Transactions on Sustainable Energy, 8(4), 1394-1405.

Guangyu X, Shaoping S & Jietao S (2017). Wind speed forecast for the stratospheric airship by incremental extreme learning machine. In 2017 36th Chinese Control Conference (CCC) (pp. 4088-4092). IEEE.

Kanna B & Singh S N (2016). Long term wind power forecast using adaptive wavelet neural network. In 2016 IEEE Uttar Pradesh Section International Conference on Electrical, Computer and Electronics Engineering (UPCON) (pp. 671-676). IEEE.

Khodayar M, Kaynak O & Khodayar M E (2017). Rough deep neural architecture for short-term wind speed forecasting. IEEE Transactions on Industrial Informatics, 13(6), 2770-2779.

Li H, Eseye A T, Zhang J & Zheng D (2017). A double-stage hierarchical hybrid PSO-ANFIS model for short-term wind power forecasting. In 2017 Ninth Annual IEEE Green Technologies Conference (GreenTech) (pp. 342-349). IEEE.

Meng K, Yang H, Dong Z Y, Guo W, Wen F & Xu Z (2015). Flexible operational planning framework considering multiple wind energy forecasting service providers. IEEE Transactions on Sustainable Energy, 7(2), 708-717.

Paixão J L, Rigodanzo J, Sausen J P, Hammarstron J R, Abaide A R, Canha L N & Santos M M (2017). Wind generation forecasting of short and very short duration using Neuro-Fuzzy Networks: A case study. In 2017 International Conference on Modern Power Systems (MPS) (pp. 1-6). IEEE.

Quan H, Srinivasan D & Khosravi A (2013). Short-term load and wind power forecasting using neural network-based prediction intervals. IEEE transactions on neural networks and learning systems, 25(2), 303-315.

Shi J, Gong Y, Liu X & Zhu X (2016). Model optimization for very-short-term wind power forecasting using Hilbert-Huang Transform. In 2016 International Conference on Smart Grid and Clean Energy Technologies (ICSGCE) (pp. 239-243). IEEE.

Wang Z, Wang W, Liu C, Wang Z & Hou Y (2017). Probabilistic forecast for multiple wind farms based on regular vine copulas. IEEE Transactions on Power Systems, 33(1), 578-589.

Xu Q, He D, Zhang N, Kang C, Xia Q, Bai J & Huang J (2015). A short-term wind power forecasting approach with adjustment of numerical weather prediction input by data mining. IEEE Transactions on sustainable energy, 6(4), 1283-1291.

Yang L, He M, Zhang J & Vittal V (2015). Support-vector-machine-enhanced markov model for short-term wind power forecast. IEEE Transactions on Sustainable Energy, 6(3), 791-799.

Zhou L, Li F & Tong X (2016a). Active network management considering wind and load forecasting error. IEEE Transactions on Smart Grid, 8(6), 2694-2701.

Zhou Y, Yan Z & Li N (2016b). A novel state of charge feedback strategy in wind power smoothing based on short-term forecast and scenario analysis. IEEE Transactions on Sustainable Energy, 8(2), 870-879.

Zhuo W & Savkin A V (2017). Wind power dispatch based on wind forecasting, electricity price and battery lifetime estimation. In 2017 36th Chinese Control Conference (CCC) (pp. 2915-2920). IEEE.

Woo Z, Hoon J, Loganathan G V (2001). A New Heuristic Optimization Algorithm: Harmony Search. *SIMULATION*. 2001;76(2):60-68. doi:10.1177/003754970107600201

Turkish Journal of Engineering – 2022; 6(3); 256-261

Turkish Journal of Engineering

https://dergipark.org.tr/en/pub/tuje

e-ISSN 2587-1366

Word-based game development on Android with an efficient graphical data structure

Mustafa Batar[*1]

[1]*Burdur Mehmet Akif Ersoy University, Faculty of Engineering and Architecture, Department of Computer Engineering, Burdur, Turkey*

Keywords
Word-Based games
Mobile games
Android
Graphs
DAWG

ABSTRACT

Today, new games are released every day, and the virtual reality market is developing in a similar way to the rapidly growing smartphone ecosystem about 10 years ago. In addition to this, mobile games that take place with smartphones in people's daily lives can be downloaded to their phones for free, without paying any money, only with an internet connection. In this sense, a mobile game on android has been designed and developed about word games for this study. These word games need to have fast feedback and fast research time to the users and the players. In this context, Directed Acyclic Word Graph (DAWG) has been used and applied for giving fast feedback in the developed game "Kelimetris" in the study. The game "Kelimetris" has been explained in detail step by step with showing its captures, screenshots, UML diagrams and code blocks. In addition, this study has showed – the graphical data structure – DAWG's efficiency and usability in word-based games on mobile phones on Android. As a result, this study will have had a positive effect on the relationship between data structures and mobile games with the contribution of the developed game "Kelimetris" and the finite state machine DAWG.

1. INTRODUCTION

Cultural historian and philosopher Johan Huizinga has one of the most enduring evaluations of the game. Huizinga game; "A voluntary action or activity that is freely consented, but carried out within the limits of certain time and place in accordance with fully mandated rules, has a purpose in itself, accompanied by a sense of tension and joy and a consciousness of 'being different' from 'ordinary life'." (Huizinga, 1995). It is possible to adapt the definition of game that Johan Huizinga has stated in this paragraph to games (adventure, simulation, action, platform games, and etc.) (Yılmaz, & Çağıltay, 2015).

The game is directed by the players, within the framework of their own wishes, the rules of the game and depending on the rules. In a game, no matter what kind of game the player plays, s/he has to comply with the rules drawn by the game scenario or the group principles developed by the virtual groups established in the game for her/his "success in the game" (Bates, 2004). It depends on the game scenario; the character cannot go out of it in order to reach his goal. Within the framework of these rules, the place where the player is located is the virtual digital game world. In addition, it is the place where the player can interact with other players in the game where the character's struggle continues. Dialogue during game streaming, especially with other players in the virtual world can establish. At the same time, the player can develop their characters in the games and provide a financial income on top of that (Aarseth, 2001).

According to Huizinga; at the same time, s/he stated that after playing once, the game can be conveyed as having a spiritual value in the memories and can be repeated at any time (Aarseth, 2003). Although some rules are games, they are not independent of everyday life. As a result, the addiction of the game increased. The game and game stages have gained new identities and images with technologies that have reached virtual reality, and have continued to take place in different positions in human life with new functions and different gameplay diversity (Su & Zhao, 2011).

Nowadays, there are thousands of different types of games in the market (Rouse, 2005). Generally, these games are related to war, strategy, race, gambling, etc. When it is looked at the games, it is realized that some users play them to take pleasure, some of them play to spend their times. However, in this study, a word-based

---

[*] **Corresponding Author**

*(mbatar@mehmetakif.edu.tr) ORCID ID 0000-0002-8231-6628

Cite this article

Batar M (2022). Word-based game development on Android with an efficient graphical data structure. Turkish Journal of Engineering, 6(3), 256-261

Research Article / DOI: 10.31127/tuje.987141

Received: 25/08/2021; Accepted: 07/09/2021

game has been chosen in order to design, develop and implement.

Word games and puzzles are spoken or board games often designed to test ability with language or to explore its properties. It has to be thought that it is to benefit individuals in several ways (Mitchell, 2001). These games enrich vocabulary of users while enjoying, they improve user's memory and exercise their mind muscles for long-term learning and retention. Thus, they have slight contribution to the users not to catch Alzheimer's disease. Furthermore, children can learn and understand new and complex words in an easy and enjoyable way. Moreover, these games require the person to read and write. After a time, they improve a person's reading and writing speed. Also, text-based games can help people (especially people in hospital, whether admitted there or waiting to hear news about a loved one) to relieve a stressful day in a way that other games cannot (Ahl, 1983).

In this study, a word game which is named "Kelimetris" has been designed and developed on Android. In "Kelimetris", stones are falling rapidly from top to bottom. One has to click on the stones to select the letters. What is needed to do is to derive meaningful words by selecting the right stones. There is no need to create words related to the each other. For each correct word, user gets points based on the points of letters. When the screen is filled with stones, the game is over.

2. The Game "Kelimetris"

General Game Functionality has described main game menu. This menu has included four main sections: "How to Play", "About the Game", "Best Players" and "Start Game". Figure 1 has showed the use cases in general game functionality in the developed game "Kelimetris".

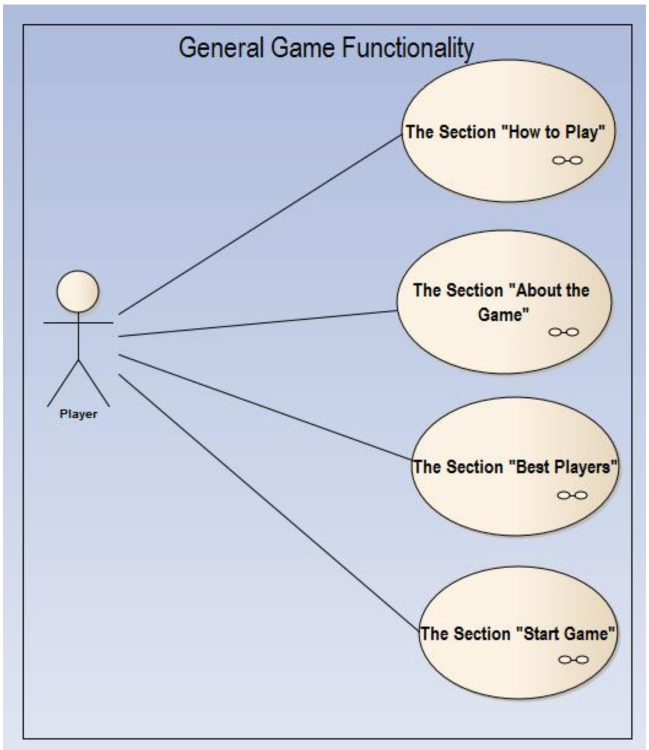

Figure 1. Use cases of the general game functionality

Figure 2. Screenshot of main game menu

In order to start the game (the main menu of the game has been given in Figure 2), if the player doesn't have a profile, the player has to create a new profile or if it exists, existing profile has to be selected. After the game is started, the player has to try to construct words by selecting as many letters as possible. The player increases his/her own score for each valid word after submission. Otherwise, s/he needs to construct new ones. In addition to this, the activity diagram of the player in order to play the game "Kelimetris" has demonstrated in Figure 3.

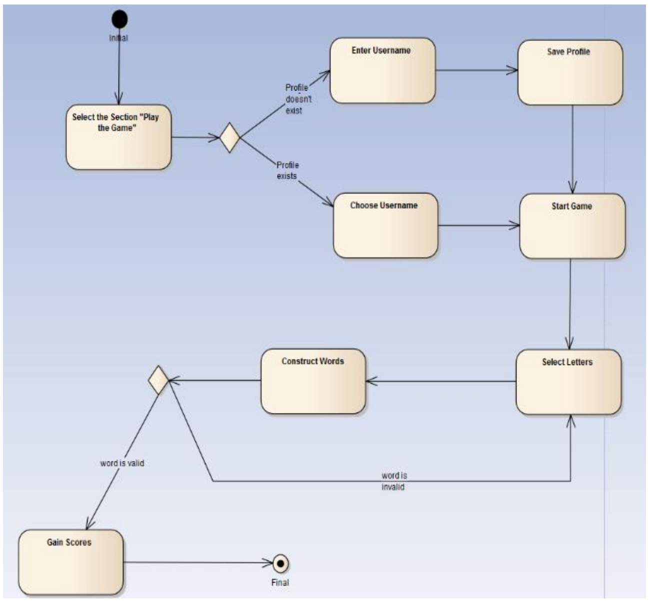

Figure 3. Activity diagram of the section "play game"

In "Kelimetris" game scenario, once the player starts the game in the main menu, then the stones that embedded a character drop consecutively in an order. The stones land on the top of each of one after another through a pattern and the stone locations are different to prevent that one stone overlaps the other. A location of a stone is not given as a location of another one before the stone leaves the window. Everything about the arrangement of the locations to the stones is done in Port super class. Also, it is needed to define some classes extending Port: these are Port1, Port2, Port3, Port4 and Port5 which are specialized to settle the stones in different columns. These ports have been captured in Figure 4 in the following.

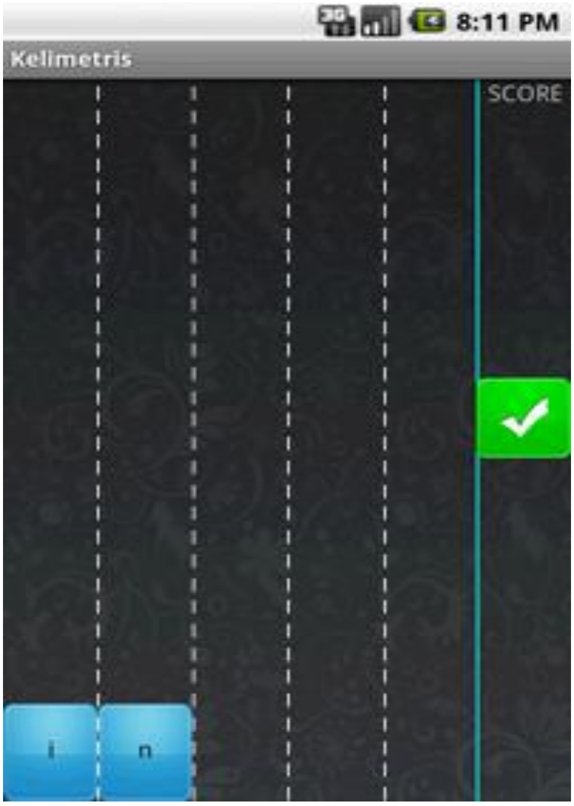

Figure 4. Capture of ports in the game

Each stone location is an integer variable and they are kept in an array named as Locations[] in port class. When any one of the classes called Port1, Port2, Port3, Port4, Port5 which extend Port is initiated, base elements of Locations[] array are initialized to -1 value by the initializeLocations() method. That means all the locations in that port are available at the beginning to settle a stone.

```
int [] Locations=new int[7];
int btnId=0;

Port(){
        initializeLocations();
}
public void initializeLocations(){
        int i;
        for(i=0;i<=6;i++){
                Locations[i]=-1;
        }
}
```

When a stone is created, its location needs to be assigned to it, therefore getButtonLocation() method gives an available location by traversing in Locations[] array and comparing if an element of it is -1. If it is, then it means this location is available and the method returns the index with the element of -1.

```
public int getButtonLocation(){
        int x=0,i;
        for(i=0;i<=6;i++){
                if(Locations[i]==-1){
                        x=i;
                }
        }
        return x*100;
}
```

After returning the index that represents an available location, the element at that index is assigned to the button ID value by insertButton() method. That means the location is not available for the coming other stones.

```
public void insertButton(){
        int i,current=0;
        for(i=0;i<=6;i++){
                if(Locations[i]==-1){
                        current=i;
                }
        }
        Locations[current]=btnId;
}
```

There is an updateLocations() method which is invoked if the created word is confirmed. The method updateLocations() actually gets IDs of the buttons that were used to make meaningful word, as the word has a meaning, the letters of that word must be removed from the game window. Their locations also have to be available in the Locations[] array, updateLocations() replace the ID values regarding the past word by -1. As the array is used to keep locations, there is no dynamically changing size of the collection after the stone is hidden (as shown in Figure 5), just the value of its location index in Location[] array in Port class is assigned to -1. Assigning -1 means that location is made available to land another stone. New dropping stones – as given in Figure 6 – come to these empty locations.

```
void updateLocations(Vector<Integer> Clickeds){
        int i;
        for(i=0;i<=6;i++){
                if(Clickeds.contains(Locations[i])){
                        Locations[i]=-1;
                }
        }
}
```

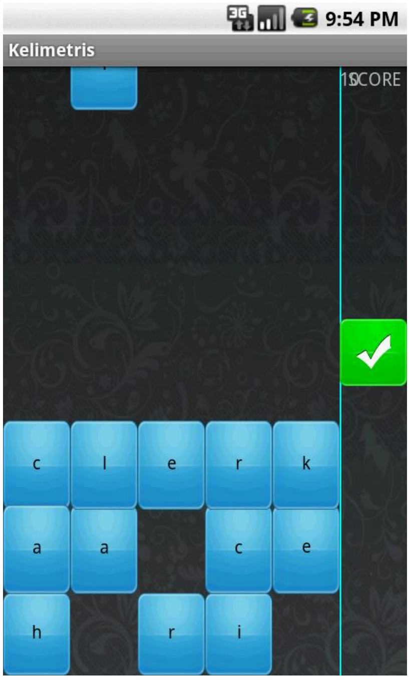

Figure 5. Capture of hidden stones in the game

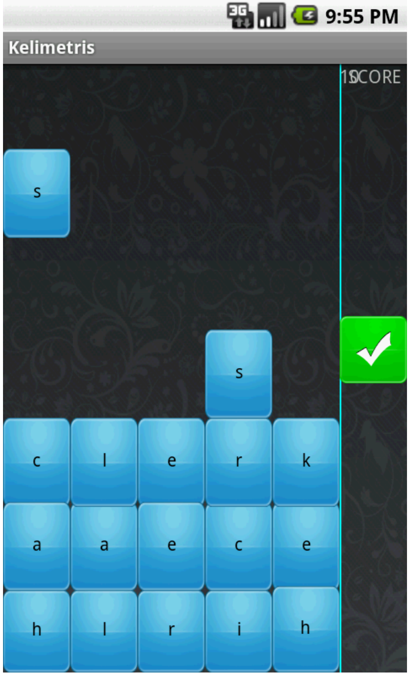

Figure 6. Replacement of new stones in the empty areas

Also, there is isLocationAvailable() method which returns true if a Location[] array includes at least one -1 value meaning available location exists. It is used to make the game over, if the game window is filled, then game has to be stopped. In this context, the location adjustment has been shown in Figure 7 in the following.

```
boolean isLocationAvailable(){
    int i;
    for(i=0;i<=6;i++){
        if(Locations[i]==-1){
            return true;
        }
    }
    return false;
}
```

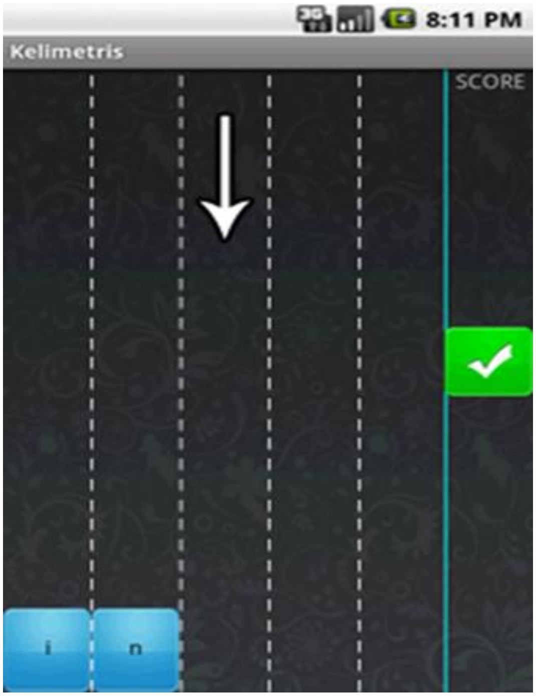

Figure 7. Drop of the stones in the game

A mechanism is needed to provide an immediate movement to each stone after it is created. It is seen that the movement of the stone (as given Figure 7 above) can be succeeded by assigning a layout parameter to this, by changing some values of this parameter periodically, and Mytask class, which extends TimerTask class, provides the mechanism. In addition, extending TimerTask class gives us an advantage to provide a continual movement by invoking a method in a specific time period.

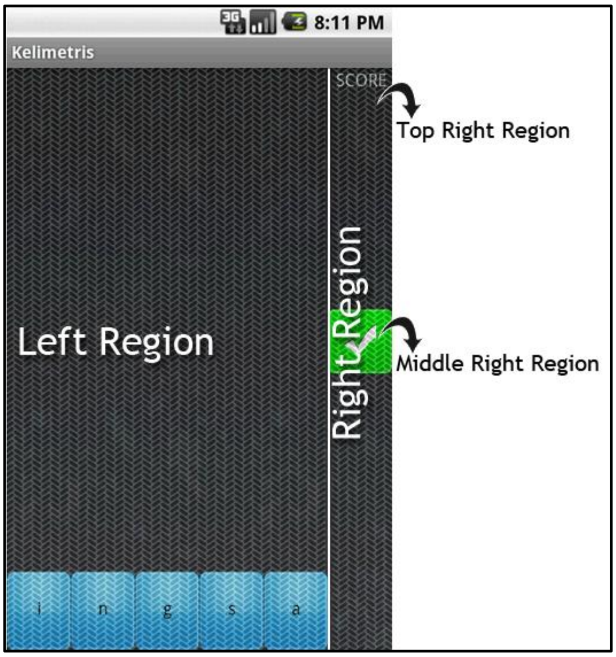

Figure 8. The regions of the window in the game

The game window has been divided into some parts as shown in Figure 8 above: the score is displayed on the right side of the layout and the buttons drop on the left side of the layout. There is a stable button stands for submission, when it is clicked; the word generated by the player is sent for looking up to a function of LetterFactory instance. If the word is confirmed, the Flag variable is assigned to be true and the update locations methods regarding each port are invoked, update locations methods result in removal of the buttons which were used for obtaining last confirmed word. A variable called portcounter type of integer is assigned, it keeps track of at which port a button will drop.

When a stone is generated, a letter is assigned to it. We have lines of words of a text file which the words are randomly taken from, and shuffled. Each character of these shuffled words is set one by one to each released stone. Words are used when their all letters are assigned to the stones, and then the new words are brought from the file. This process goes on as long as the game is being played. All things that regarding the above are done by LetterFactory class. The method addFromFile() opens a text file and fetches corresponding to valid words at the random lines in the file. Then fetched words are pushed into a vector named words. wordsIndexes are random integers corresponding to random lines in the text file so as to get the words randomly from the file.

In addition to this, in computer science, a directed acyclic word graph (DAWG) (Appel & Jacobson, 1988) is a data structure that represents a set of strings, and allows for a query operation that tests whether a given string belongs to the set-in time proportional to its length. In these respects, a DAWG (Crochemore & Vérin, 1997) is very similar to a tree, but it is much more space efficient. The entry point into the graph represents the starting letter in the search. Each node represents a letter, and you can travel from the node to two other nodes, depending on whether you the letter matches the one you are searching for. It is a directed graph (Aoe, Morimoto, Shishibori & Park, 1996) because one can only move in a specific direction between two nodes. In other words, one can move from A to B, but one can't move from B to A. It is Acyclic (Perrin, 1990) because there are no cycles. One cannot have a path from A to B to C and then back to A. The link back to A would create a cycle, and probably an endless loop in your search program. The structure of DAWG (Jansen & Boekee, 1990) has been given in Figure 9.

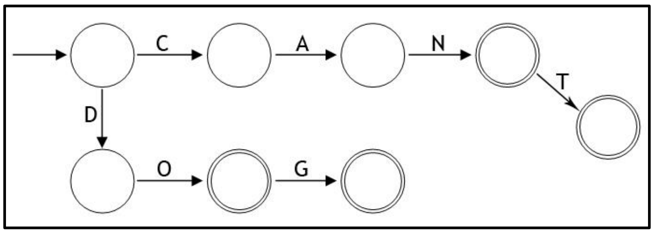

Figure 9. DAWG working structure

Based on DAWG in Figure 9, the words "can", "can't", "do" and "dog" could be gained and created easily.

Moreover, each letter has its own point. The points have been determined based on their usage rate. That means if a letter places in many words, its point will be less than the others that place rarely. Table 1 in the following has showed the standard points of each letter in the game "Kelimetris" for scoring.

Table 1. Letter points in the game

Letter	Value	Letter	Value	Letter	Value
A	1	I	2	R	1
B	3	İ	1	S	2
C	4	J	10	Ş	4
Ç	4	K	1	T	1
D	3	L	1	U	2
E	1	M	2	Ü	3
F	7	N	1	V	7
G	5	O	2	Y	3
Ğ	8	Ö	7	Z	4
H	5	P	5		

3. Results of the Game "Kelimetris"

As the consequences of the performance test in which trying to search in a text file for a particular word, it results that it takes 0,8 seconds for a file that consists of 3.000 lines of words. However, when it comes to handle a file that consists of 60.000 lines of words, approximately it takes over 10 seconds. There is need a dictionary which includes at least 80.000 words to be played in the game. Therefore, DAWG Algorithm implementation has been applied and developed for this game "Kelimetris". The results of searching a word in "Kelimetris" have been given in Table 2 in the following.

Table 2. Word search time in the game "Kelimetris"

The Technique	The Number of The Words	The Search Time
Read from the File	1000	~0,6 seconds
Read from the File	48000	~10 seconds
DAWG	1000	~0,001 seconds
DAWG	48000	~0,5 seconds
Read from Database	1000	~1 seconds
Read from Database	48000	~5 seconds

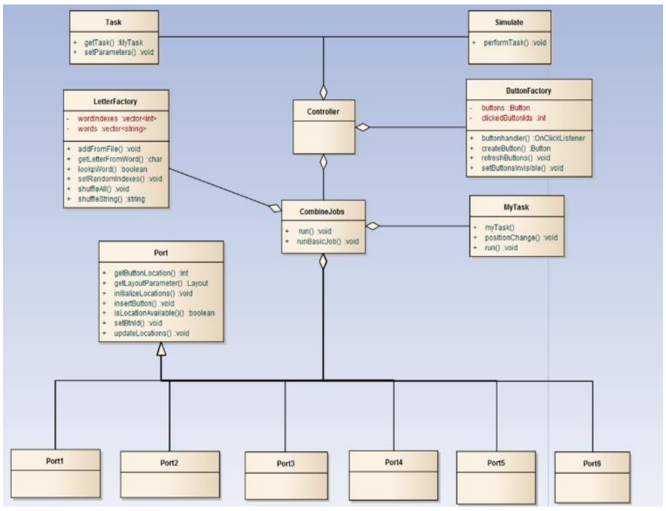

Figure 10. The class diagram of the game

According to data in Table 2, it has been easily seen that DAWG is very efficient and useful data structure in searching a word in a mobile game with its fast feedback.

Finally, the game "Kelimetris" has been designed, developed and accomplished to complete based on the class diagram shown in Figure 10.

4. CONCLUSION

As a result of the development of technologies, the game industry has become a large economic market in a short time. From the first electronic game in 1947, to Tennis for Two in 1958, from Pong to Pac-Man, from Commodore 64 to Gameboy and Playstation, from Snake on a Nokia mobile phone to social media games, from Angry Birds on smartphones Until the first Pokemon Go game, which was developed using virtual reality, the game industry has always made progress, except for short pauses. By making large investments in the mobile game market, companies have entered into the competition of game making. The increase in internet connection speed, tablets, smartphones and social media have made the gaming industry a constantly evolving industry.

Based on this evolving gaming industry, there is need to give fast responses to the players and the users in the games. In this context, the developed game "Kelimetris" on Android in the study has given a graphical data structure DAWG (directed acyclic word graph) to improve fast feedbacks and to shorten waiting period in the game. Thus, the study has brought an innovation into the mobile game development, and the literature as well.

ACKNOWLEDGEMENT

Ethics committee approval document is not required for this study, and the author declares that there is no conflict of interest.

Conflicts of interest

The authors declare no conflicts of interest.

REFERENCES

Aarseth E (2001). Computer Game Studies, Year One, Game Studies: International Journal of Computer Game Research, 1(1).

Aarseth E (2003). Playing Research: Methodological Approaches to Game Analysis. Computer Game Theory Compendium.

Ahl D H (1983). Creative Computing Video & Arcade Games.

Aoe J, Morimoto K, Shishibori M & Park K-H (1996). A Trie Compaction Algorithm for a Large Set of Keys, IEEE Transactions on Knowledge and Data Engineering, 8(3), 476-491.

Appel A W & Jacobson G J (1988). The World's Fastest Scrabble Program. Communications of the ACM, 31(5), 572-578.

Bates B (2004). Game Design: The Art and Business of Creating Games. Boston, MA: Thomson Course Technology.

Crochemore M & Vérin R (1997). Direct Construction of Compact Directed Acyclic Word Graphs, 8th Annual Symposium, CPM 97, Aarhus, Denmark, 116-129.

Huizinga J (1995). Homo Ludens, (Çev. MA. Kılıçbay), İstanbul: Ayrıntı Yayınları.

Jansen J A & Boekee D E (1990). On the significance of the directed acyclic word graph in cryptology, Advances in Cryptology — AUSCRYPT '90, Lecture Notes in Computer Science, 453, Springer-Verlag, pp. 318–326, doi:10.1007/BFb0030372, ISBN 3-540-53000-2.

Mitchell B L (2001). Game Design Essentials, Indianapolis: John Wiley & Sons, Inc.

Perrin D (1990). Finite Automata, in: J. van Leeuwen, ed., Handbook of Theoretical Computer Science, Elsevier, Amsterdam, Vol. A, 3-57.

Rouse R (2005). Game Design, Theory and Practice (Wordware Game Developer's Library). USA: Worldware Publishing.

Su H, Zhao V (2011). Alive Character Design: For Games, Animation and Film, Beijing: CYPI Press.

Yılmaz E & Çağıltay K (2015). History of Digital Games in Turkey, Digra Uluslar Arası Konferansı.